UNIVERSITÀ
DEGLI STUDI
FIRENZE

INTERNATIONAL DOCTORATE
IN ATOMIC AND MOLECULAR PHOTONICS

CYCLE XXXIII

COORDINATOR Prof. Francesco Saverio Cataliotti

Photonic crystals based on smart polymers

A new route for tunable devices

Academic Discipline (SSD) FIS/03

Doctoral Candidate
De Bellis Isabella
_____
(signature)

Supervisor
Prof. Wiersma Diederik Sybolt
_____
(signature)

Co-Supervisor
Dr. Nocentini Sara
_____
(signature)

Coordinator
Prof. Cataliotti Francesco Saverio
_____
(signature)

Years 2017/2020

Summary

Abbreviations **4**

Introduction **5**

1 Techniques and Materials for 3D Printing **7**

1.1 Lithographic techniques for 3D printing **7**

1.2 Lithographic techniques for polymeric micro- and nano-patterning **9**

1.2.1 Photolithography and soft lithography 9

1.2.2 Electron beam lithography 11

1.2.3 Direct laser writing 12

1.3 Materials for polymeric micropatterning **15**

1.3.1 Positive and negative photoresists 15

1.3.2 Polymerization process and two-photon absorption 16

1.3.3 Advantages of polymers 17

1.3.4 Ip-Dip™, a commercial polymer for DLW 18

1.3.5 Resolution, swelling and rigidity in custom resists 19

1.3.6 Hydrogels 20

1.3.7 "Smart materials" : Liquid Crystalline Networks for optics and photonics 20

1.3.8 LCNs: phases and molecular alignments 22

1.3.9 The employed Liquid Crystalline Network mixture 23

1.3.10 Cell configurations for LCN alignment 25

2 Tunable Optics and Photonics **33**

2.1 3D printing for optics and photonics **33**

2.2 3D printing for responsive structures **34**

2.3 Static photonic devices fabricated by DLW **36**

2.4 Different stimuli to control photonic micro-devices made via DLW **37**

2.5 Liquid crystalline elastomeric devices fabricated via DLW for tunable photonics **40**

3 Modulation of optical properties in Liquid Crystalline Networks across different length scales **49**

3.1 Methods to measure material birefringence **49**

3.2 Wedge-cell refractometer method **50**

3.2.1 Experimental set up 51

3.3 Macro- and microscopic LCN samples **54**

3.4 Optical characterization 57
3.4.1 Macroscopic wedge cell 57
3.4.2 Microscopic wedge cell 61

4 Temperature role in two-photon polymerization in birefringent materials ... 68
4.1 Stimuli responsive soft polymers: resolution increase at the microscale 68
4.2 Strategies and studies to improve resolution 69
4.2.1 Temperature role on resolution 70
4.3 Materials characterization 71
4.3.1 Polymerization threshold 72
4.3.2 Voxel dimension 74
4.3.3 Swelling 76
4.3.4 Anisotropic resolution in LCN mixture 78

5 Tunable elastomeric photonic crystals 85
5.1 Photonic crystals 85
5.1.1 Three-dimensional photonic crystals 86
5.2 Woodpile photonic crystal 88
5.3 3D woodpile PC made of Liquid Crystalline Networks 89
5.3.1 Fabrication of a LCN woodpile by DLW at room temperature 89
5.3.2 Optical characterization 92
5.3.3 LCN woodpile fabricated via DLW at 10 °C 95
5.3.4 UV post curing of LCN woodpile photonic crystals 96
5.3.5 Tuning of the stop band at telecom range by temperature variation .. 98
5.3.6 Towards the tuning of the woodpile stop band by light 99

6 Color modulation in *Morpho* butterfly wings using Liquid Crystalline Elastomers 102
6.1 Natural photonic crystal as template for tunable structural colors 102
6.2 *Morpho* butterfly wing integrated with liquid crystal elastomers 104
6.2.1 LCE artificial muscles 104
6.2.2 Two coupling integration strategies 105
6.3 *Morpho Menelaus* blue butterfly 106
6.3.1 Morphology 106
6.3.2 Reflectance characterization 110
6.4 Artificial muscle of liquid crystal elastomer 113
6.4.1 Fabrication procedure of the LCE film 114
6.5 Biotic-abiotic hybrid system made by *Morpho Menelaus* butterfly and LCE artificial muscle 116
6.5.1 LCE film integration in *Morpho Menelaus* wing 116

6.5.2 LCE layer infiltrated in *Morpho Menelaus* blue butterfly wing 121
6.6 Towards butterfly wing replicated in PDMS and LCE 128
6.6.1 Negative PDMS mold of butterfly wing 128
6.6.2 Positive LCE replica of butterfly wing 130
6.6.3 Effects of interference in LCE butterfly wing replica 131
A Optics of Liquid Crystalline Elastomers 136
A.1 Optics of uniaxial anisotropic media 136
A.2 Interference of polarized light 137
Conclusions 140
List of publications 144

Abbreviations

The following abbreviations are used in this manuscript:

PCs	Photonic Crystals
LCNs	Liquid Crystalline Networks
DLW	Direct Laser Writing
UV	Ultraviolet
3D	Three-dimensional
HOT-DIW	High Operating Temperature Direct Ink Writing
LCEs	Liquid Crystalline Elastomers
T_{NI}	Nematic-Isotropic Temperature
PDMS	Polydimethylsiloxane
EBL	Electron Beam Lithography
SEM	Scanning Electron Microscopy
AOM	Acousto-Optic Modulator
POM	Polarized Optical Microscope
TPA	Two-Photon Absorption
VIS	Visible
NIR	Near Infrared
PEG	Poly(ethylene glycol)
LCPs	Liquid Crystal Polymers
PI	Polyimide
PVA	Polyvinyl Alcohol
PLA	Polylactide
PEG-DA	Poly(ethylene glycol) diacrylate
FDTD	Finite-Difference Time-Domain
WGMR	Whispering Gallery Mode Resonator
PMMA	Polymethyl Methaclyrate
LED	Light Emitting Diode
TPP	Two Photon Polymerization
STED	Stimulated-Emission Depletion
PGMEA	Propylene Glycol Methyl Ether Acetate
AOTF	Acousto-Optic Tunable Filter
PBG	Photonic Band-Gap
CW	Continuous Wave
RO	Radial Outward

Introduction

Photonic technology aims to control light propagation within miniaturized devices that can possibly integrate different functionalities. Among them, tuning the optical properties of photonic structures in a reversible and non-invasive way has attracted attention of scientists aiming to make dynamically reconfigurable structures. To this aim, photonic crystals (PCs) represent a versatile platform: their permittivity modulation at a length scale comparable with the working wavelength prevents light propagation in a frequency range, the so called band gap. In such a way, the light propagation can be locally and efficiently controlled introducing linear or punctual defect in 2D or 3D structures to create waveguides with minimal losses and high quality factor cavities.

The aim of this thesis is the study, fabrication and optical characterization of tunable PCs having different functionalities in optics and photonics and the modulation of their optical properties (e.g. refractive indices, optical anisotropy, reflectance, etc...). In order to realize dynamically reconfigurable structures, photo-responsive polymers, which allow a remote and non-invasive control of their optical properties, have been employed. Liquid Crystalline Networks (LCNs), which combine the orientational order of liquid crystals with the elasticity of a cross-linked polymeric rubber have been chosen. Their striking properties of photo- and thermo-responsivity and shape changing behavior result particularly suitable to fabricate reconfigurable photonic crystals. We selected light stimuli as activation signal because, due to its remote and non-invasive nature, is highly compatible with photonic applications. Moreover, temperature effects were investigated as well in order to broaden the range of applications. Periodic structures have been studied following different research approaches, both for a more deep understanding of the optical properties of such customized material and for different applications, from tunable telecom filters to tunable structural colors.

In the first part of this thesis, after the description of the most important 3D lithographic techniques and materials employed for polymeric micro-patterning, some applications of polymer technology for tunable optics and photonics are presented, focusing the attention on recent LCN-based applications.

In this work, liquid crystalline network have been deeply studied by investigating their anisotropic optical properties through refractive indices

measurements, fundamental quantity for the design of LCN photonic structures. Ordinary and extraordinary refractive indices have been measured as a function of temperature and light by using a wedged cell based refractometer method. Different mixtures were studied with different dyes and cross-linker percentages. The material characterization has been performed comparing the optical properties of macroscopic samples that have been polymerized by an ultraviolet (UV) lamp and microscopic samples polymerized by Direct Laser Writing (DLW). This allowed to highlight as different polymerization processes affect the optical properties at different length scales.

In order to pattern the first elastic tunable photonic crystals with nanometric resolution, the lithographic technique of DLW has been employed. To combine the customized LCN material and the DLW lithographic technique, tailored calibrations, characterizations and relative improvements have been performed. Among the different writing parameter, temperature was investigated to improve resolution and the quality of the polymerized structures. Such calibration underlined an unexpected temperature dependence of the LCN polymerization process, and allowed to achieve very competitive resolutions, comparable with the other commercial resists, never reached for liquid crystalline networks, so far.

The third part of this work concerns the manufacturing and optical characterization of the first example of a tunable LCN woodpile PC filter, having a stop band at telecom wavelength, which has been tuned in a reversible way by temperature.

In the last part, the first proof of a smart visualizable sensor, developed during a six-month period in collaboration with Prof. Li and Prof. Keller group in Paris, at Chimie ParisTech, is presented. We explored the integration of efficient thermo-responsive Liquid Crystalline Elastomers, whose properties have been customized at the Chimie ParisTech laboratories, together with the *Morpho* butterfly wing, owing an optimized structural coloration due to its natural photonic crystal structure and superhydrophobic properties. A new biotic-abiotic platform capable of color tuning in response to temperature changes has been projected, described and optically characterized.

Chapter 1

1 Techniques and Materials for 3D Printing

Chapter 1 introduces the conventional lithographic techniques for 3D macro- and nano-printing in polymeric materials. The potentialities and limitations of these lithographic techniques are discussed with a particular attention on Direct Laser Writing technique. The chemical and physical material properties of shape changing polymers are introduced, describing in detail Liquid Crystalline Network properties. These materials characterized by a reversible deformation in response of a given stimulus, such as light, temperature, pH, electric or magnetic field, have been widely explored in this work in combination with both macro and micro fabrication techniques. Their choice was dictated by their millisecond responsiveness, their optical transparency and birefringence, their controllable deformation and processability with Direct Laser Writing technique. These peculiar properties allowed the demonstration of tunable photonic devices.

1.1 Lithographic techniques for 3D printing

Three-dimensional (3D) printing is a new challenge in the customized manufacturing of components. Several printing techniques allow to fabricate macroscopic 3D objects with a resolution reaching tens of micrometers. Among them, one of the most well-known technique is stereolithography [1], which is based on laser-induced polymerization of a liquid resist contained into a tank. Only the exposed portion of the resin at the polymer/liquid interface hardens creating layer by layer a 3D solidified component. Another type of 3D macro-printing is based on fused deposition modeling, a common type of 3D printing based on the material extrusion: thermoplastic materials are melted and pulled out through a nozzle forming successive object layers along precise directions. Instead, in selective laser sintering [2], performed to create metal or ceramic 3D structures, metal powders and ceramic powders are commonly employed and the powder is piled up layer-by-layer. In direct ink writing [3, 4] the liquid-phase "ink" is dispensed out of small

nozzles under controlled flow rates and deposited along digitally defined paths to fabricate layer-by-layer 3D structures.

However, all these techniques enable to print object of several centimeters in size with microscopic geometrical feature of tens of microns [5]. As an example, Zarek et al. [6] demonstrated that by using a commercial stereolithography 3D printer, complex shape memory structures with high resolution can be fabricated based on polycaprolactone. The achieved resolution along the X- and Y-axis is 39 μm, whereas for Z-axis, the resolution can be as low as 1 μm. As shown in Figure 1.1.a, complex shape memory miniaturized Eiffel Tower can be obtained and this approach can be extended to biomedical devices or flexible electronics. Kotikian et al. employed high operating temperature direct ink writing (HOT-DIW) to print 3D Liquid Crystalline Elastomers (LCEs) with mesogen domains aligned along the direction of the printing path [7]. As shown in Figure 1.1.b, when the temperature is higher than the nematic-isotropic temperature (T_{NI}), defined as the temperature at which the nematic to isotropic phase transition occurs, the 3D printed LCE (about 1 mm thick) contracts and it is capable of lifting an object of 20 g. Moreover, the 3D printed shape-morphing LCEs with specific architectures can undergo remarkable planar-to-3D reversible transformations upon thermal stimulus [7].

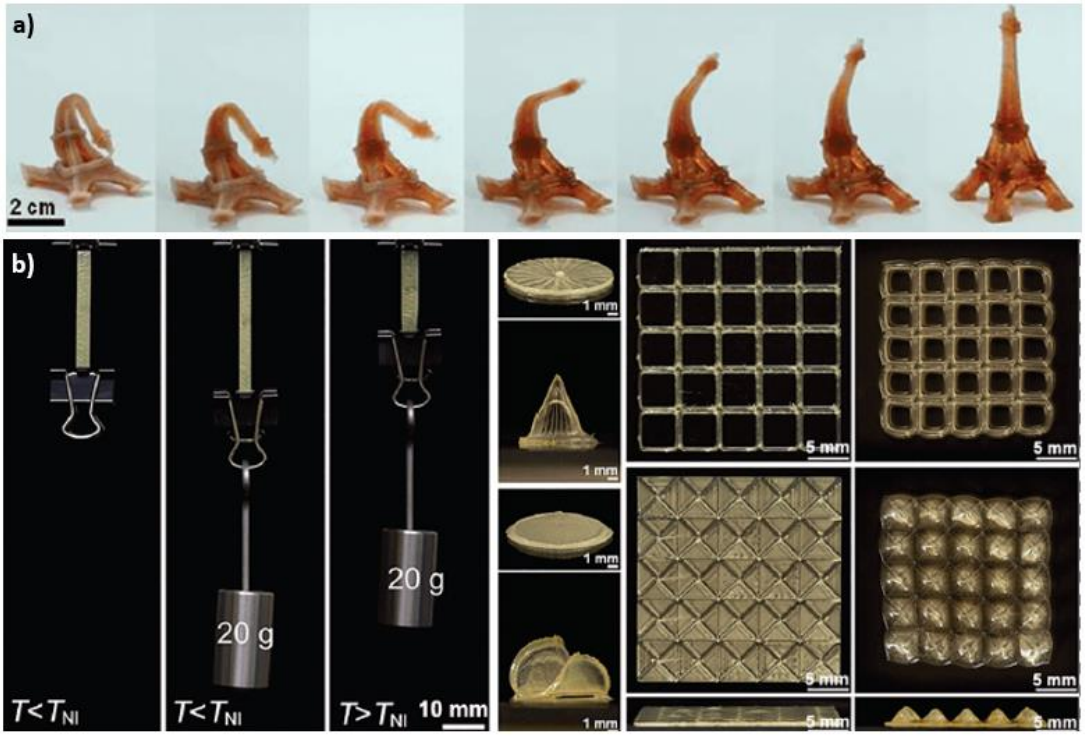

Figure 1.1. a) Stereolithography 3D printed shape memory scaled Eiffel Tower reverting to its original shape at 70 °C. Adapted from reference [6]. b) LCE

structures realized via HOT-DIW: weight lifting (20 g) of the printed LCE at $T>T_{NI}$; programmable shape morphing of LCEs into cone, saddle shape, and conical array upon heating above T_{NI}, respectively. Adapted from reference [7].

Since we are interested to design and fabricate tunable photo-elastic devices with micro- and nanoscopic features, other lithography techniques, such as photolithography, electron-beam lithography and direct laser writing (DLW) should be considered in order to decrease the lithographic resolution to the nanometer scale.

1.2 Lithographic techniques for polymeric micro- and nano-patterning

1.2.1 Photolithography and soft lithography

Aiming at a nanostructuration, photolithography and soft lithography are two common techniques suitable for large scale production of geometries with planar designs [8].

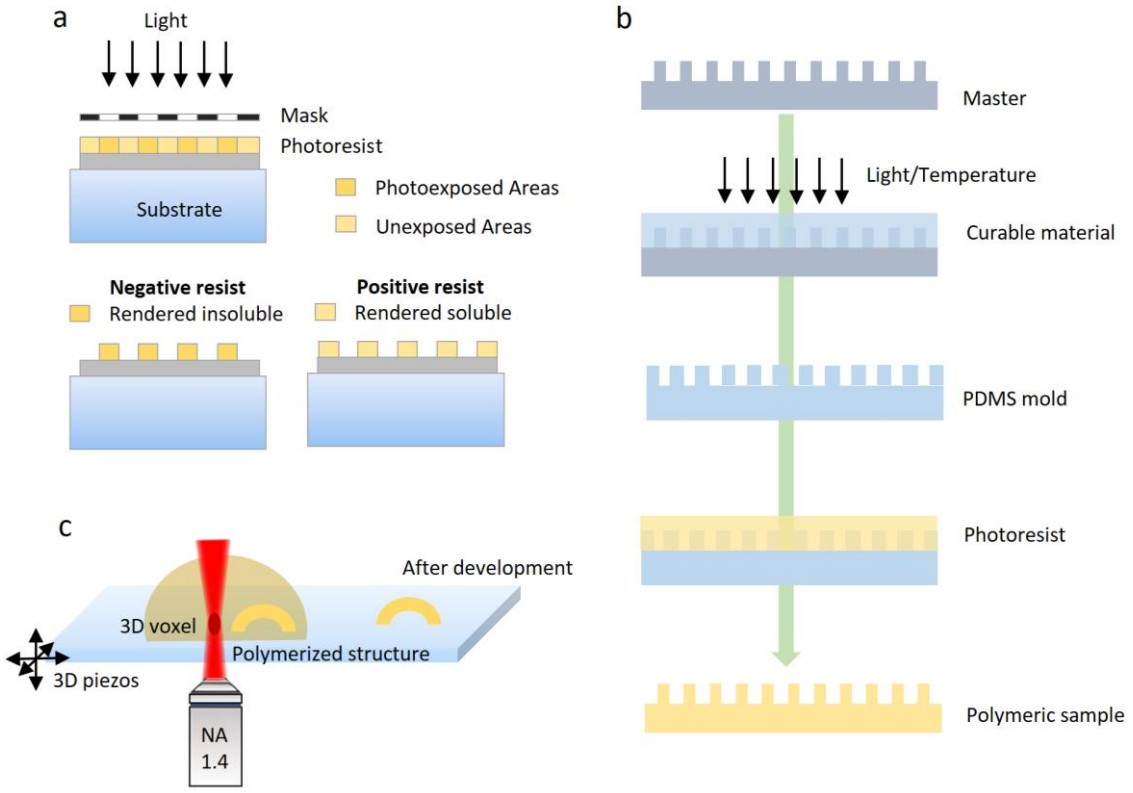

Figure 1.2. Scheme of the main lithographic techniques for polymeric micropatterning: a) photolithography, b) soft lithography, c) direct laser writing.

In photolithography, [9] glass or metal substrates are covered by a thin homogeneous film of a photoresist, generally prepared by spin coating. After irradiation using collimated UV light, which passes through a mask, the final pattern is obtained following a development procedure that allows to eliminate the undesired material (Figure 1.2.a).

In contrast to photolithography, soft lithography allows the fabrication on different substrates, from planar to curved and flexible ones combining high versatility, low cost and simple material manipulation. Replica molding is often realized with negative tone resists [10]. UV light exposure causes the polymerization of the chemical structure in these photoresists. In this manner, instead of becoming more soluble, negative photoresists become hard and extremely difficult to dissolve, while the photoresist developer solution removes the unexposed liquid volumes [11]. Typically, soft lithography, as a first step, requires the preparation of a flexible polydimethylsiloxane (PDMS) mold created by replicating the silicon stamp master: the PDMS mixture after covering the master is cured at high temperature. The PDMS is then removed from the master reproducing its negative features. Then the PDMS mold is used to give the desired geometries by pulling it onto the liquid resist. After UV curing, the PDMS mold is peeled off, obtaining thereby a positive copy of the master made of the chosen polymeric material (Figure 1.2.b) [12]. The printing process, allows for the realization of a large number of micropatterned structures in a fast and easy way but the fabrication of the stamp master requires other more complex lithographic techniques, as photolithography or electron beam lithography. Soft lithography has been widely used to pattern shape change materials that well reproduce the micron sized features of the PDMS stamp/mold. Keller *et al.* utilized soft lithography to prepare micron sized pillar array made by thermo-responsive liquid crystalline elastomers [13]. The pillars underwent a reversible contraction and expansion of the order of 30-40% when heating and cooling (Figure 1.3).

Figure 1.3. An isolated pillar exhibits a contraction with the order of 35%. Adapted from reference [13].

1.2.2 Electron beam lithography

Electron beam lithography (EBL) is a high-resolution and direct-write exposure method [15, 16]. EBL consists in scanning a beam of electrons across a surface covered with an electron sensitive resist film, thus depositing energy in the desired pattern. A tightly focused electron beam scans the surface of the sample covered by the resist. Therefore, the exposed pattern can be changed at every lithographic realization/step without using masks. EBL enables to fabricate extremely fine patterns (up to $\backsim$ 5 nm [17]).

Figure 1.4 illustrates the fundamental parts of an EBL machine. Electrons are generated by a source kept under vacuum (p $\backsim 2 \cdot 10^{-9}$ mbar), named electron gun. They are guided towards the sample through an electron optical system: a beam aligner, condenser lenses, a stigmator, a pair of deflectors and an objective lens direct, shape and focus the electron beam on the sample. In addition, there is a beam blanker to quickly deflect the beam, in order to avoid undesired exposure of the sample. Inside another chamber under vacuum (p $\backsim 2 \cdot 10^{-5}$ mbar), a mechanical stage holds the sample and positions it with respect to the electron beam. A vibration isolation system is necessary to maintain the alignment between the beam and stage constant during the exposure, while the whole EBL equipment is controlled through a computer.

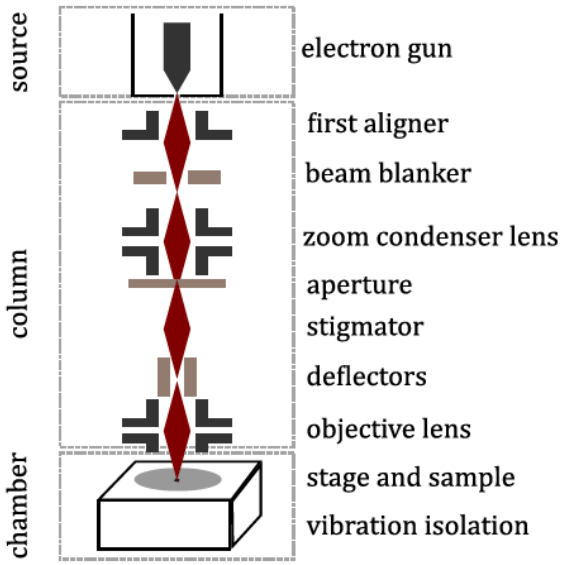

Figure 1.4. Scheme of a typical EBL system.

Scanning Electron Microscopy (SEM), widely used during this research work to characterize the morphology of the samples, works according to the same principle.

The electrons interact with the sample producing various signals (e.g. secondary electrons, backscattered electrons, and characteristic X-rays) that are collected by one or more detectors to obtain information about the surface topography and composition. SEM high-resolution feature derives from the small wavelength associated to electrons. According to de Broglie expression ($\lambda = h/\sqrt{2mK}$), with $K =$ eV which is the kinetic energy and it is proportional to the applied electrical potential V), an electron's wavelength in an electrical potential difference of V = 10 kV, is only 0.12 Å, several order of magnitude smaller than a photon's wavelength (typically 100 nm to 400 nm).

1.2.3 Direct laser writing

The realization of arbitrary and complex 3D shapes can be obtained by Direct Laser Writing (DLW), which allows for lithographic resolutions better than 150 nm, representing therefore the technique of choice for 3D polymer photonics in a single fabrication step [14]. In fact, without the use of masks or complex and expensive machines and materials, 3D structures can be realized in a single writing process in polymeric matrices. DLW is based on a nonlinear absorption process and allows to create, point-by-point, a 3D polymeric object replicating a computer designed structure (Figure 1.2.c). In DLW technique, pulsed femtosecond lasers with high peak energy (as Ti:sapphire femtosecond oscillators or second harmonic fiber lasers) are tightly focused to a diffraction-limited spot within the photoresist [18, 19]. They have two main advantages: very short pulses, of the order of tens of femtoseconds, which do not cause thermal damage, while the standard emission wavelength of around 800 nm allows in-volume focusing with minimal scattering in transparent material. The laser intensity is chosen such that only in the focal volume it is sufficiently high to induce polymerization via two-photon absorption creating a "voxel" (a 3D pixel). The shape of the voxel is an ellipsoid with typically the major axis about twice as long as the minor axis. The laser focal spot is then scanned in 3D by moving the sample using a piezoelectric translation stage, thus writing point by point the computer designed 3D structure [19, 20]. Second generation DLW systems have the sample fixed. Moreover, by using galvanometric mirror the laser beam is deflected to address the different point of the structure to be polymerized, improving the writing speed and fabrication times. At the end of the writing process, the unpolymerized mixture is washed away by means of an

organic solvent, leaving the fabricated microstructures on the substrate. By means of DLW, a subdiffraction limited lateral resolution of around 120 nm is easily achieved [21a]. On the other hand, DLW presents disadvantages as long fabrication times, which can limit the scaling up of the process and mass production.

In our lab, a commercial DLW system (Photonic Professional Nanoscribe GmbH) has been employed for the photopolymerization at the microscale, using a 780 nm erbium doped femtosecond fiber laser by focusing the beam, circularly polarized, by a 10x or 100x-oil-immersion objective.

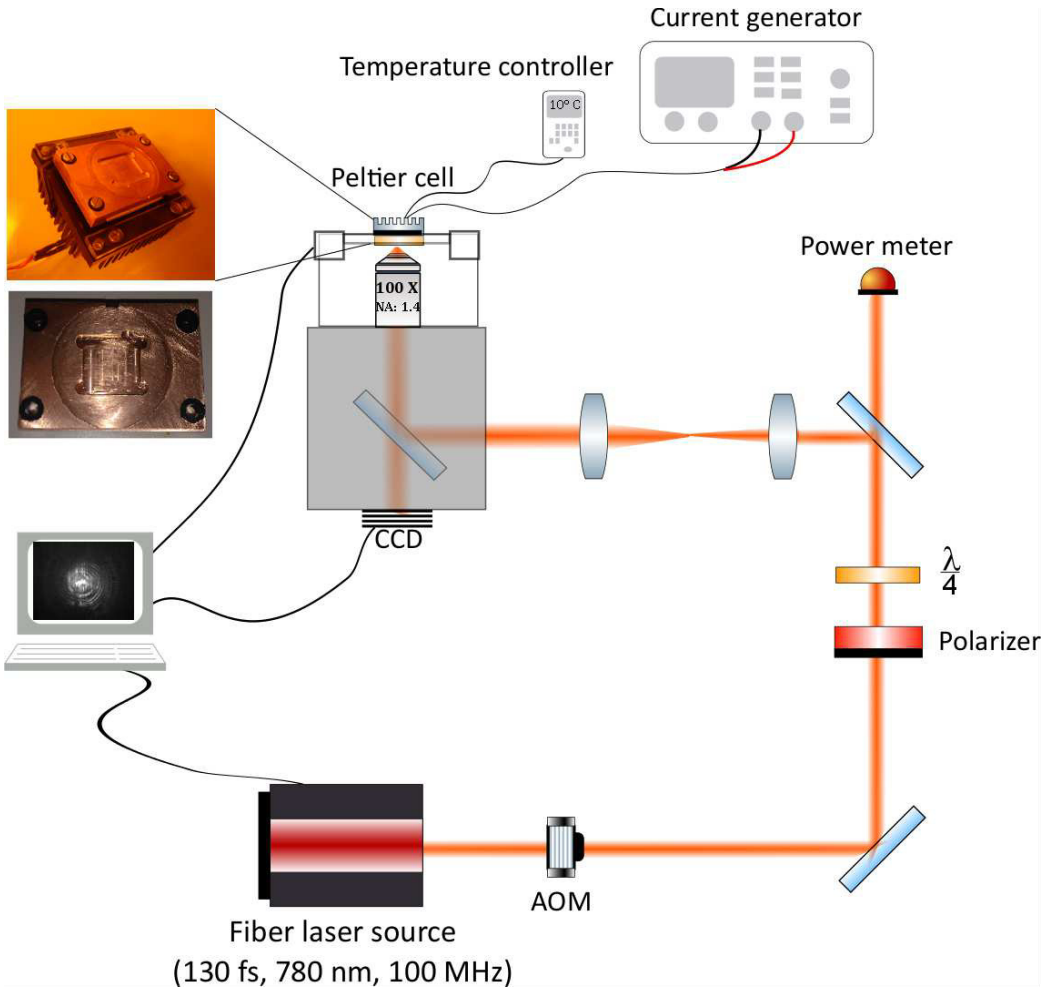

Figure 1.5. Nanoscribe GmbH set up with the home-made Peltier cell.

The laser pulses are 130 fs long with a 100 MHz repetition rate. An acousto-optic modulator (AOM) is used to control the writing average power (Figure 1.5). Through the AOM, only the first diffracted order is selected and its intensity is set by proper parameters in the writing codes. A first polarizer linearly polarizes the beam, and a quarter waveplate ($\lambda/4$) circularly polarizes the beam in order to

eliminate voxel asymmetry in the focal plane caused by large numerical apertures of the objective. The beam is then splitted by a beam sampler: one beam is collected by a detector in order to monitor the power; the other one passes through a beam expander in order to fill the back aperture of the focusing objective and through a system of mirrors, it is sent to an inverted microscope. The laser beam is then focused into a cell where the photoresist is dropped, spin-coated or infiltrated depending on the sample preparative. By using a 3D axis piezo-activated stage is possible to fabricate 3D arbitrary geometries.

In commercial DLW system, the temperature control of the sample and therefore the polymerization temperature control has not been implemented. On the other hand, this is a fundamental parameter responsible for lithographic features as resolution and structure rigidity in polymeric materials with temperature dependent properties. Moreover, several phenomena (e.g. swelling, polymerization shrinkage, monomer diffusion), having a temperature dependence, contribute to determine the voxel dimension.

In several fabrication protocols of this work, described in Chapters 4 and 5, a home-made system constituted by a Peltier cell (current driven), a heatsink and a thermometer have been designed and introduced to control the local radical polymerization temperature.

In general, a material suitable for structuring with DLW includes at least two components: a monomer, or a mixture of monomers/oligomers, which will provide the final polymer and a photoinitiator, which will absorb the laser light and provide the active species that will cause the radical polymerization. Negative photoresists (see 1.3.1), such as hydrogels, acrylate materials as IP-Dip™ [5, 21b] and the epoxy-based photoresist SU-8™ [21c], are typically employed. In the last years, a renewed interest about custom materials highlights as many different chemical/physical properties of the microstructures can be achieved patterning them by DLW [21d, 21e]. Recently, DLW has enabled to reach sub-microscopic resolution in a particular class of polymers, named “smart materials” - and described in detail in the paragraph 1.3.7 - such as Liquid Crystalline Networks. For example, Zeng et al. [22] used DLW to print 3D LCN structures and maintaining desirable molecular orientations as shown in Figure 1.6.a. Zeng et al. [23] also fabricated an azo-dye based LCN walker via the DLW printing system, shown in Figure 1.6.b. When the walker was stimulated by a modulated laser beam, it showed fast response to light and exhibited reversible contraction of around 20% along the nematic phase

direction. More recently, Wiersma and co-workers reported a microhand composed of four LCN "fingers" (100 µm in length) with different alignments (Figure 1.6.c) that are capable to bend towards the same point under light optical illumination [24] in order to grab and hold very small objects, such as polymeric microcubes (40 µm × 40 µm × 20 µm in size) (Figure 1.6.d).

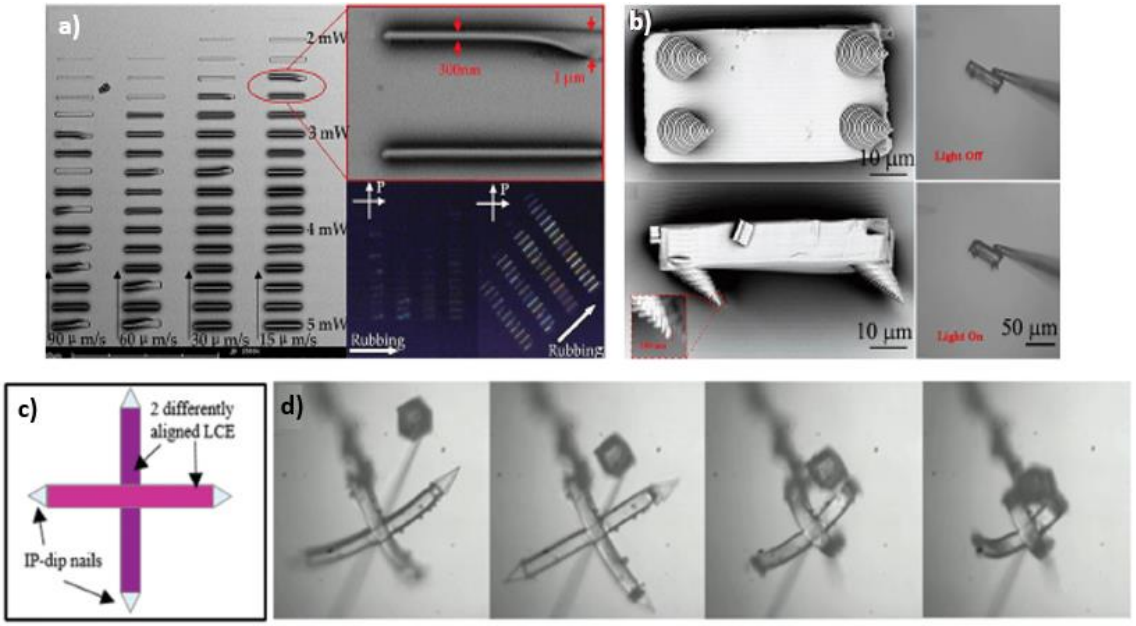

Figure 1.6. a) SEM and polarized optical microscope (POM) images of LCN linear structures fabricated by DLW. Adapted from reference [22]. b) SEM images and the actuation of a DLW printed micro-walker under a 532 nm laser beam. Adapted from reference [23]. c) Schematic microhand design. d) Sequence of the microhand catching a micro-object. Adapted from reference [24].

1.3 Materials for polymeric micropatterning

1.3.1 Positive and negative photoresists

After this first brief introduction about fabrication techniques, the next paragraphs describe some of the different employed materials, starting from the distinction of positive and negative photoresists.

In case of positive photoresists [25], the light or electron beam hits the material in the areas that the user intends to remove. After exposure the photoresist undergoes a depolymerization reaction becoming more soluble in the photoresist developer. The exposed areas are then washed away with a developer solvent,

leaving the remaining structure. The photoresist regions that are not exposed are left insoluble to the photoresist developer.

In case of negative resists (e.g. SU-8™, commercial photoresists as Ip-L™, Ip-Dip™, or "smart" materials as liquid crystal polymers, networks, elastomers and hydrogels) [10a], the exposure induces/promotes the cross-linking of the chemical structure of the photoresist. In this manner, instead of becoming more soluble, negative photoresists become hard and extremely difficult to dissolve, and the photoresist developer solution removes the unexposed liquid volumes.

1.3.2 Polymerization process and two-photon absorption

Polymer micropatterning, induced by the fabrication techniques previously described, is based on a photopolymerization process. It mainly refers to a polymerization reaction, which is initiated by light absorption, transforming single molecules, named monomers in their liquid state, into a polymeric, solid and insoluble material [10b]. In order to promote radicals formation, small molecules, called photo-initiators, are added. They play the role of polymerization starters. In the next step, known as the propagation, the initiator fragment reacts with a monomer molecule to form the first active adduct that is capable of being polymerized. Monomers continue to add in the same manner resulting in the formation of radical chains. After the polymeric chain termination, once two radical chains neutralize each other, the polymer backbone network is realized and the material acquires a solid phase. Cross-linking molecules have been also added. Therefore, during the polymerization process, cross-linking processes also take place in which different polymer chains are connected to each other, under illumination, affording more rigid structures. By choosing the nature and structure of the different cross-linkers, it is possible to control the physical, chemical and mechanical properties of the solidified polymeric structure.

In case of 3D lithography, it is achieved through a nonlinear process: two-photon or (2-photon) absorption (TPA) [10c]. In TPA, an electron simultaneously absorbs two photons to transcend the energy gap in one excitation event. When the sum of the two absorbed photons is resonant with the transition, photo-initiators are excited to triplet states and decay into radicals that trigger the radical polymerization. The TPA cross section of this process depends on the squared intensity [10c], which is the underlying mechanism to improve the spatial resolution in two-photon fabrication. On the other side, the small TPA cross sections need for

sufficiently high intensities, providing sub-diffraction resolution by the polymerization of a small volume, named voxel (3D pixel), where the intensity of the laser exceeds the threshold.

In between cationic and radical polymerization [10b], we focused on acrylate based free radical polymerization, which is one of the more studied and widely employed polymerization reaction. Cationic polymerization is a type of chain growth polymerization in which a cationic initiator transfers charge to a monomer which then becomes reactive. This reactive monomer goes on to react similarly with other monomers to form a polymer. In free radical polymerization, when exposed to light, photoresists generate free radicals that trigger the polymerization. Radicals then react with monomers in a cascade process, forming a monomer radical chain which is neutralized by another radical to form a polymeric chain. The reactions that produce radicals have to compete with monomer quenching, oxygen quenching and other pathways of deactivation of the excited states like phosphorescence emission.

1.3.3 Advantages of polymers

Polymers with respect to other semiconductor materials offer advantages and drawbacks. The choice of the structure constituents is mainly determined by the final application of the device. Besides being very cheap materials, polymers can be integrated on different substrates [26], and combined together with the previously described fabrication techniques as UV lithography, soft lithography [13], 3D printing and direct laser writing [27]. The great potential of polymers resides in the possibility to tailor their physical, electronic and optical properties by adjusting the polymerization process and chemical structure. Moreover, in case of responsive materials, a dynamic control of their properties can be achieved by external stimuli, opening to tunable structures for optics and photonics, such as integrated optical circuits and photonic crystals [28], for optical signal modulation and switching [29]. In this scenario, polymer photonics, exploiting the versatility and multi-functionality of polymers, can represent an alternative to silicon technology. Even if photonic components based on glassy and soft polymers cannot approach, at least at present, the levels of performance and mass production obtained with silicon technology [27, 30a], polymer photonics offers a complementary approach based on arbitrary and customized geometries made by properly designed materials. In addition, thanks to the possibility to pattern polymeric micro- and nano-structures

with a very high resolution, DLW has been demonstrated a good tool for our challenge: to exploit responsive polymers in optics and photonics. In this work both rigid and soft responsive polymers have been employed. The first ones are commercial polymers as Ip-Dip™, the second one are stimuli responsive materials as Hydrogels and Liquid Crystalline Networks and Elastomers.

1.3.4 Ip-Dip™, a commercial polymer for DLW

In our experiments, we employed Ip-Dip™, a commercial (Nanoscribe GmbH), acrylate-based, negative and liquid photoresist. Its molecular structure is reported in Figure 1.7 [30b].

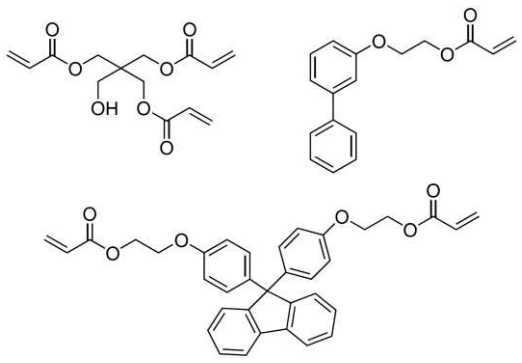

Figure 1.7. Chemical structure of IP-Dip™ commercial resist

Its refractive index is n = 1.52 at 780 nm, before the light exposure, and it increases of 2% after the polymerization process. The lithographic features of IP-Dip™ microstructures are a high stability and rigidity, low proximity effect and shrinkage and a lateral resolution of 150 nm. Commercial acrylate-based polymers are widely used to create static photonic structures as waveguides, whispering gallery mode resonators and photonic crystals. These materials are already optimized in terms of resolution, rigidity and swelling. Moreover, acrylate based photopolymers have several properties which make them attractive for multi-photon polymerization applications: a wide variety of the full composites or their monomers are commercially available; they are transparent at visible (VIS) and near infrared (NIR) wavelengths, and can be therefore processed by NIR and VIS ultra-fast lasers; it is possible to develop them in common, non-aggressive solvents such as isopropanol and can be polymerized rapidly and with low shrinkage. Moreover, after polymerization, they are mechanically and chemically stable. IP-Dip™ has been developed as a resist in which the immersion objective can be dipped working both as immersion oil and photoresist. It is widely used for upside down fabrication placing a drop in the glass center, between the glass and objective.

This fabrication geometry allows for printing micro structures with a high aspect ratio (height (up to 300 um)/lateral dimension) preventing laser beam scattering in the already polymerized resist. At the same time, the microstructure height is not limited by the objective focal distance.

1.3.5 Resolution, swelling and rigidity in custom resists

When customized resists are employed for new applications, two fundamental aspects have to be considered: it is necessary both to preserve the high resolution and to guarantee the same structural mechanical stability, typical of commercial photoresists. In order to reduce the minimal voxel dimension many techniques can be adopted (e.g. the use of a radical quencher) [31, 32], while the increase of the structure stability is more challenging especially in soft polymers. After polymerization, the structures can undergo swelling (of unpolymerized monomers) or other shrinkage processes (during solvent development and drying), which cause distortions or, in the worst cases, the structure collapse. In particular, these undesired effects become critical problems in case of suspended or not bulky structures (e.g. for photonic crystals) having a typical structure periodicity of hundreds of nanometers. An efficient strategy to avoid deformations and reduce the stickiness with a consequent increase of the structure rigidity, as demonstrated for IP-Dip™ structures [33], is an UV post curing. Since DLW does not generate a full conversion of the acrylate moieties, the mechanical properties of the written structures can be improved by immersion of the polymerized micro structure into a photo-initiator solution and irradiation with an UV lamp. In this way, the conversion of the polymerizable groups can be completed and the final material is more resistant to the development and drying process, as shown in Figure 1.8 for IP-Dip™ micro-structures. This successfully procedure has been investigated and applied to our soft polymers to reduce the stickiness of the structures and improve their optical properties.

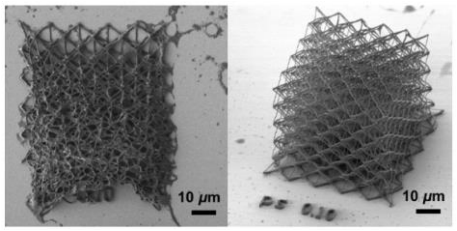

Figure 1.8. Post-print UV curing method: SEM images show the same final structure developed directly after writing (on the left) or subjected to UV curing (on the right). Adapted from reference [33].

In order to create tunable devices, materials with an intrinsic response to external stimuli have been selected [34]. Hydrogels and Liquid Crystalline Networks are the responsive polymeric matrices employed in this research work.

1.3.6 Hydrogels

Hydrogel polymers are hydrophilic polymers that can hold large amounts of water in the interspatial spaces of their 3D network, shrinking their volume under an external stimulus as temperature variation and leading to reversible process of water deswelling [35-37]. The use of hydrogels is mainly limited to biological applications and microfluidics as the material operation requires a liquid environment. Hydrogels can be prepared with natural molecules (e.g. proteins), representing an ideal biocompatible platform for the realization of optical elements or cellular scaffold to be used in vivo [38]. Nevertheless, the achievable lithographic resolution, rarely below 1 µm, limits the possible geometries [39, 40].

We employed in Chapter 4, the hydrophilic polymeric network of PEG (Poly(ethylene glycol)) dyacrylate average Mn 250, whose molecular structure is reported in Figure 1.9, with the 5% mol of initiator reported in Figure 1.11.

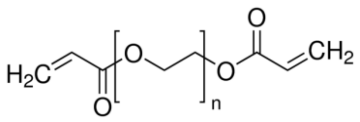

Figure 1.9. Chemical structure of Poly(ethylene glycol) dyacrylate average Mn 250.

1.3.7 "Smart materials": Liquid Crystalline Networks for optics and photonics

The research for "smart materials" that respond to external stimuli (e.g. pH variations, ion concentration, temperature, electric field, etc.) with a shape change has attracted the attention of a lot of scientists. Among smart materials, particular interest has been deserved to nematic liquid crystal elastomers. They were introduced for the first time from de Gennes [41, 42] that proposed them using the definition of "artificial muscles". The idea was to make use of a conformational

change of the polymer backbone at the nematic to isotropic phase transition [43] as the motor for a macroscopic contraction.

According to chemical compositions, crosslinking densities and thermodynamical properties, there is a division of "smart materials" in between Liquid Crystal Polymers (LCPs), Liquid Crystalline Networks (LCNs) and Liquid Crystalline Elastomers (LCEs) [44]. LCPs are rigid linear polymers (without crosslinking molecules in their composition) with liquid crystalline phases and a very high Young modulus above 100 GPa. LCNs have a glass transition temperature in the interval (40-100) ℃ and a Young modulus of around 1 GPa. LCEs are a subclass of the LCNs and are characterized by lower than room temperature glass transition and a low degree of crosslinking that brings the Young modulus down to MPa.

In the palette of responsive polymers, LCNs, the materials widely explored in this thesis, are characterized by the high molecular anisotropy of liquid crystals and elasticity of cross-linked networks, and present many opportunities for tunable photonic devices thanks to their ability to reversibly deform and change their birefringence under an external stimulus such as temperature or light [45-47]. Moreover, they can be manufactured by lithographic fabrication techniques, their properties can be widely chemically tuned, they provide a low-cost fabrication and can be integrated in several diversified materials with different functions. For all these reasons, a great challenge aims to the optimization of LCNs properties in order to introduce them in optics and photonics, for tunable photonic devices.

In particular, the aim of this work is the demonstration of optically/thermally tunable photonic structures by controlling the three-dimensional deformation and birefringence with the light irradiation or temperature variation. Light activation is a highly promising control stimulus because it enables a local control and a wireless activation of the structures. Moreover light is a multi-parameter quantity (e.g. polarization/wavelength/power), that can be modulated in space and time without needing integration of electrodes or needing huge magnetic coils. On the other hand, temperature is a well-established LCN control stimulus that can be employed in absence of polymer dye doping or in case of temperature sensors.

In this thesis, studies about refractive indices and optical anisotropy measurements of LCNs have been described in Chapter 3, while a method to increase the resolution in LCN structures, fabricated by DLW, has been developed and described, in detail, in Chapter 4. LCNs have been patterned by DLW, in order to demonstrate a tunable 3D microscopic woodpile photonic crystal, described in

Chapter 5. Moreover in Chapter 6, LCEs have been polymerized by an UV lamp, taking advantage of soft lithography, in order to make an elastomeric actuator and modulate the optical properties of the natural *Morpho* genus butterfly photonic crystal.

1.3.8 LCNs: phases and molecular alignments

LCNs are characterized by various phases. In nematic phase, the molecules tend to align along a preferred direction called director, resulting in an anisotropic optical medium, characterized by two different refractive indices: the extraordinary refractive index (n_e) along the axis parallel to the LCN director (**n**) and the ordinary one (n_o) in the perpendicular plane. Under an external stimulus such as temperature, light, pH, magnetic field, LCNs do not show a complete transition to the isotropic phase (as in standard low molecular weight liquid crystals in which no molecular order is preserved), reaching instead the so called para-nematic phase where the alignment is only partially destroyed [48]. Therefore, all the different stimuli induce only a partial loss of the molecular anisotropy. During the phase transition, the system changes its shape with a consequent contraction along the nematic director and an expansion in the perpendicular plane in case of homogeneous (molecules parallel to the surface) and homeotropic (molecules perpendicular to the surface) alignments. In this research work, we used these two particular types of alignments whose schematics is reported in Figure 1.10. Once the stimulus is switched off, the material returns spontaneously the original shape [49]. Engineering the mesogen alignment, for example, by using played or twisted configurations, opens to more complex deformations as bending [50], torsion [51], or rotation [52]. Big anisotropic deformations (up to 20% of the structure length) [53] have been reported for LCNs in different environments (from air to solvents) and demonstrated in tunable photonic platforms [54-55]. Instead for LCEs, a typical deformation is of the order of 35% [13] but their softness prevents their use for photonic application in which even small deformation can determine a large shift of the optical properties.

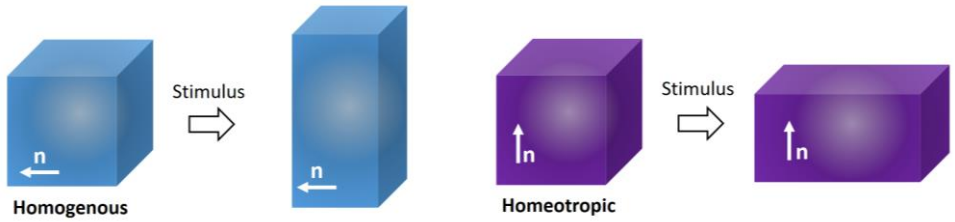

Figure 1.10. Different alignment configurations: in homogeneous configuration, LCN molecules are parallel aligned to the substrate plane, in homeotropic configuration, LCN molecules are perpendicular to the plane. In both cases, under an external stimulus the alignment results in contraction along the director direction and elongation in the perpendicular plane.

1.3.9 The employed Liquid Crystalline Network mixture

In this work, we mainly focused on a LCN mixture synthetized at the European Laboratory for Non-Linear Spectroscopy lab, which has been optimized to be patterned with DLW.

The preparation of our LCN mixture, depicted in Figure 1.11, requires three components: a mesogen, responsible of the material alignment, a cross-linker, which allows the formation of a network with an elastic mechanic response and a photo-initiator (Irgacure 369™), to achieve the spatial control of the radical polymerization reaction. The first two components need to be functionalized with one or two photo-polymerizable groups, such as the acrylate group for an acrylate based photopolymerization. To optically activate the material deformation, an azobenzene dye has been added to these three components [53]. In particular, the mixture contains: 68% mol of monomer, 30% mol of cross-linker, 1% mol of azo-dye and 1% mol of initiator (Irgacure 369™). The phase transition temperature from nematic to isotropic is at about 60 °C for this specific mixture as shown in Figure 1.12.

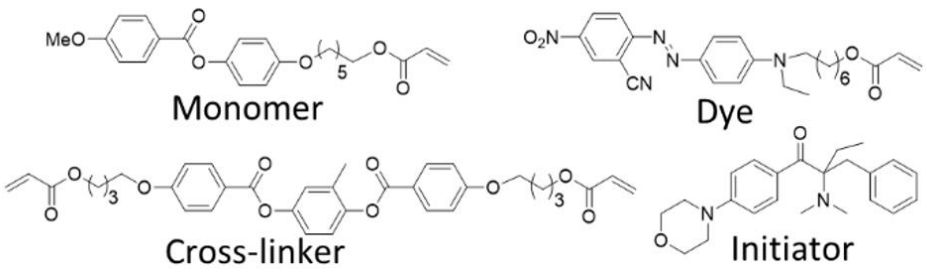

Figure 1.11. Chemical structures of the molecules employed for the LCN mixture.

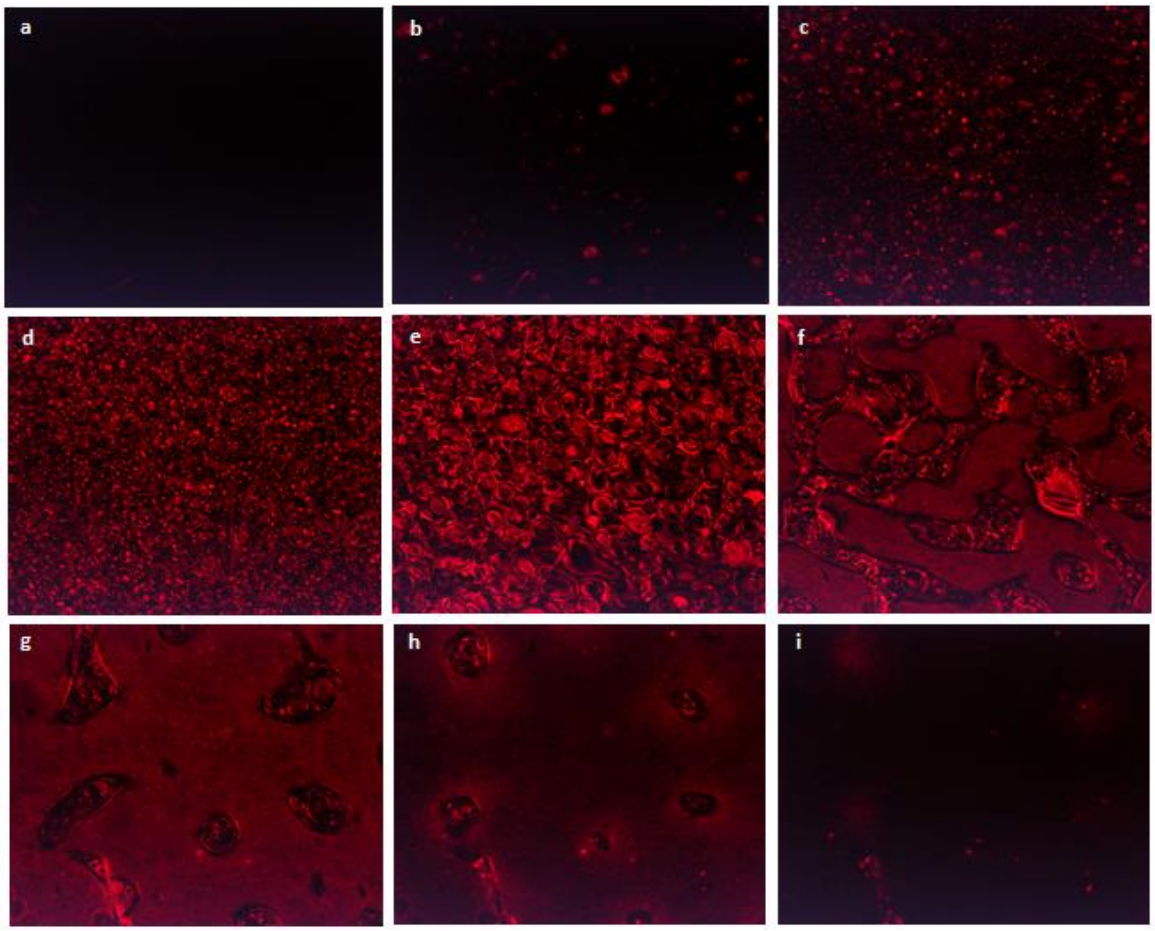

Figure 1.12. Polarized optical microscope images, during the temperature decrease, showing the transition phase from isotropic to nematic of the LCN mixture: a) isotropic phase at 70 °C; b) formation of nematic phase at a temperature of about 64 °C; c-h) formation and growth of liquid crystal domains; i) monodomain formed at about 61 °C.

Monomer and cross-linker were purchased from Synthon Chemical (SYNTHON Chemicals GmbH & Co. KG, Wolfen, Germany), initiator Irgacure 369™ was purchased from Sigma Aldrich (Sigma Aldrich SRL, Milano, Italy). The choice of the mesogens, responsible for the properties of the photoresist, has been done to have a nematic phase at room temperature for several hours, making easy the structuration with the standard lithographic platform [57]. On the other hand, in order to obtain a photoresponsive material, a dye (an azobenzene molecule) was properly prepared to match the technical requirement of the operational wavelength of the lithographic technique. Commercial azo-dyes typically have an absorption band in the UV spectral range and are not suitable for direct laser writing fabrication, as this overlaps with the photoinitiator two-photon absorption

peak used in the system. To circumvent this, the azo-dye absorption has been tuned by changing the substituents on the aromatic rings, thus opening a gap of minimum absorption around 390 nm and a transparency window above 700 nm [53]. Azobenzenes induce deformations in LCNs by two main mechanisms [58, 59]. The first one is the isothermal transition due to a trans-to-cis isomerization: the rod-like trans azobenzene is converted in its bent cis form, disturbing the LC order by changing of the molecular dipolar moment and by steric effects [60-62]. On the other hand, dyes can work as nanoscale heaters able to convert light in a thermal jump that induces a light induced thermal transition [60]. Thermal imaging of polymers doped with push-pull azodye, which was added to our chemical formulation clearly demonstrated as, in this case, the effect that generates light driven deformation is mainly thermal [63-65]. Moreover, the material rigidity and the DLW resolution can be controlled by adjusting the ratio between monomer and cross-linker, having control of the shape-changing properties [66]. The percentages of the various components have been varied according to the experiment. In fact, the balance in between the molecules impacts strongly the mechanical properties and the sample response. In addition, the patterning of LCNs with DLW showed that tuning the lithographic setting (e.g. power laser or writing speed) and varying the chemical composition of the mixture, a lateral resolution of 160 nm can be achieved, for mixtures with the higher content of the cross-linking agent (40% mol/mol) [52]. In this research work, it has been demonstrated, for the first time in Chapter 4, that also polymerization temperature strongly affects the LCN micro-structures resolution patterned via DLW.

1.3.10 Cell configurations for LCN alignment

The type of deformation of a micro-structure depends on the LCN molecular alignment. It can be controlled with a proper cell prepared using proper sacrificial layers in which the LCN mixture is infiltrated. In particular, homogeneous cells (Figure 1.13.a) were prepared by means of a polyimide (PI5291, Nissan Chemical) coated glass from one side and a polyvinyl alcohol (PVA 1%) coated glass on the other side, separated by 20 µm spacers (ThermoFisher borosilicate glass microspheres reported in the SEM image of Figure 1.13.b) and placed at the edges of the cell. The coatings were chosen in order to align the molecules parallel to the glass surface, by the rubbing of the sacrificial layers using a velvet cylinder. Meanwhile, homeotropically aligned LCN cells (with the director perpendicular to

the glass surface) were made of two glasses both coated with PI1211. The LCN mixture, reported in Figure 1.11, was melted in its isotropic phase on a hot plate at 75 °C and infiltrated for capillarity. Afterwards, the cell was cooled down until room temperature at -1 °C/min, and the liquid crystalline alignment was checked with a polarized optical microscope (Zeiss, Axio Observer A1, Jena, Germany). The cell was glued into a proper holder and fixed on the inverted microscope of the DLW system. The LCN microstructures have been anchored to the bottom glass and have been realized from the bottom to the top using an immersion oil objective. After the writing process, the LCN cell was removed from the holder, opened with a blade, and put in a bath of 2-propanol at 75 °C, the first of 20 minutes and the latter of 10 minutes in order to dissolve the unpolymerized material without any degradation of the polymerized structures. Finally, the glass was dried with clean air. A scanning electron microscope was used to observe the LCN structures after sputtering them with a 10 nm gold layer.

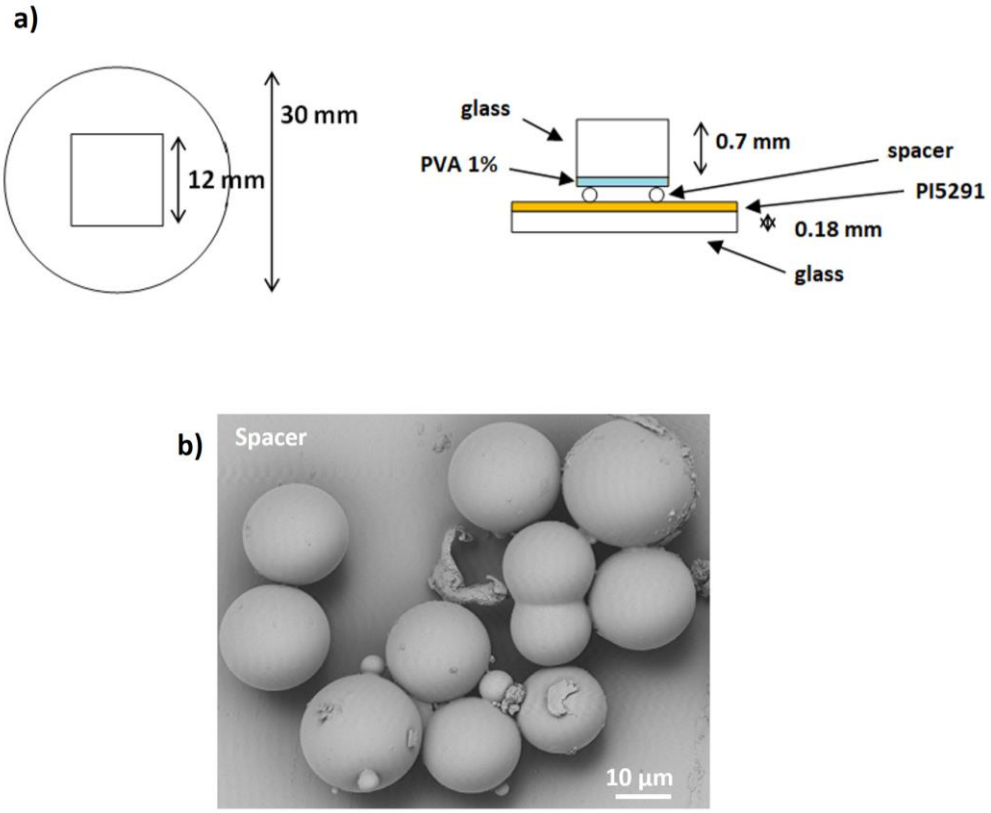

Figure 1.13. a) Top view and side view of the LCN cell homogenously aligned. b) SEM image of spacers having diameters of 20 µm.

In this thesis, side-chain polymer architecture has been chosen: the mesogens are attached with a flexible spacer to the network. After the liquid crystal monomer orientation, the acrylate polymerization has been activated by a photo-polymerization process via UV lamp to create macroscopic film or via two-photon absorption for microscopic structures. The polymerization process in both cases is a free radical polymerization process triggered by the photo-initiator. After the elastic structure fabrication, the shape and refractive index control have been obtained by temperature or light.

References

[1] F. P. Melchels, J. Feijen, D. W. Grijpma, Biomaterials 2010, 31, 6121.

[2] J. P. Kruth, P. Mercelis, J. Van Vaerenbergh, L. Froyen, M. Rombouts, Rapid Prototyping J. 2005, 11, 26.

[3] B. Derby, Annu. Rev. Mater. Res. 2010, 40, 395.

[4] J. A. Lewis, Adv. Funct. Mater. 2006, 16, 2193.

[5] C. N. LaFratta, J. T. Fourkas, T. Baldacchini, R. A. Farrer, Angew. Chem., Int. Ed. 2007, 46, 6238.

[6] M. Zarek, M. Layani, I. Cooperstein, E. Sachyani, D. Cohn, S. Magdassi, Adv. Mater. 2016, 28, 4449-4454.

[7] A. Kotikian, R. L. Truby, J. W. Boley, T. J. White, J. A. Lewis, Adv. Mater. 2018, 30, 1706164.

[8] D. Qin, Y. Xia, G. M Whitesides, Nat. Protoc. 2010, 5, 491.

[9] C. Mack, Fundamental Principles of Optical Lithography: The Science of Microfabrication, Wiley, Hoboken, NJ, USA 2007.

[10a] H. Lorenz, M. Despont, N. Fahrni, N. La Bianca, P. Renaud, P. Vettiger, J. Micromech. Microeng. 1997, 7, 121.

[10b] M. Farsari, M. Vamvakaki, B. N. Chichkov, J. Opt. 2010, 12, 124001.

[10c] X. Zhou, Y. Hou, J. Lin, AIP Adv., 2015, 5, 030701.

[11] Y. Xia, G. M. Whitesides, Angew. Chem., Int. Ed. 1998, 37, 550.

[12] Y. Xia, G. M. Whitesides, Annu. Rev. Mater. Sci. 1998, 28, 153.

[13] A. Buguin, M.-H. Li, P. Silberzan, B. Ladoux and P. Keller, J. Am. Chem. Soc. 2006, 128, 4, 1088-1089.

[14] J. Fischer, M. Wegener, Laser Photonics Rev. 2013, 7, 22.

[15] P. Rai-Choudhury. Handbook of microlithography, micromachining, and microfabrication: microlithography, volume 1. Iet, 1997 (cited on page 68).

[16] D. J. Grant and S. Sivoththaman. Electron-beam lithography: From past to present. University of Waterloo, Canada, 2003. (cited on page 68).

[17] V. R. Manfrinato, L. Zhang, D. Su, H. Duan, R. G. Hobbs, E. A. Stach and K. K. Berggren, Nano Lett. 2013, 13, 4, 1555-1558.

[18] H. B. Sun, S. Kawata, in NMR—3D Analysis—Photopolymerization, Springer, Berlin 2004.

[19] C. Barner-Kowollik, M. Bastmeyer, E. Blasco, G. Delaittre, P. Moller, B. Richter, M. Wegener, Angew. Chem., Int. Ed. 2017, 56, 2.

[20] Y. Guo, H. Shahsavan, and M. Sitti, Adv. Mater. 2020, 32, 2002753.

[21a] S. Kawata, H.-B. Sun, T. Tanaka, K. Takada, Nature 2001, 412, 697.

[21b] M. Farsari, G. Filippidis, K. Sambani, T.S. Drakakis, C. Fotakis, J. Photochem. Photobiol. A 2006, 181, 132-135.

[21c] S. Juodkazis, V. Mizeikis, H. Misawa, J. Appl. Phys. 2009, 106, 051101.

[21d] M. Hippler, E. Blasco, J. Qu, M. Tanaka, C. B. Kowollik, M. Wegener, M. Bastmeyer, Nat. Comm. 2019, 10, 232.

[21e] D. Gräfe, S. Walden, J. Blinco, M. Wegener, E. Blasco, and C. B. Kowollik, Angew. Chem. Int. Ed. 2019.

[22] H. Zeng, D. Martella, P. Wasylczyk, G. Cerretti, J.-C. Gomez Lavocat, C.-H. Ho, C. Parmeggiani, and D. S. Wiersma, Adv. Mater. 2014, 26, 2319-2322.

[23] H. Zeng. P. Wasylczyk, C. Parmeggiani, D. Martella, M. Burresi, D. S. Wiersma, Adv. Mater. 2015, 27, 3883-3887.

[24] D. Martella, S. Nocentini, D. Nuzhdin, C. Parmeggiani, D. S. Wiersma, Adv. Mater. 2017, 29, 1704047.

[25] W. Zhou, S. M. Kuebler, K. L. Braun, T. Yu, J. K. Cammack, C. K. Ober, J. W. Perry, S. R. Marder, Science 2002, 296, 1106.

[26] M. Schumann, T. Bückmann, N. Gruhler, M. Wegener and W. Pernice, Light: Science & Applications 2014, 3.6, e175.

[27] M. Deubel, G. von Freymann, M. Wegener, S. Pereira, K. Busch, C. M. Soukoulis, Nat. Mater. 2004, 3, 444−447.

[28] S. Nocentini, D. Martella, C. Parmeggiani, D. S. Wiersma, Adv. Opt. Mater. 2019, 1900156.

[29] T. A. Ibrahim, W. Cao,Y. Kim, J. Li, J. Goldhar, P.-T. Ho, C. H. Lee, J. Lightwave Technol. 2003, 21, 2997.

[30a] J. Leuthold, C. Koos, W. Freude, Nat. Photonics 2010, 4, 535.

[30b] https://pdf.directindustry.com/pdf/nanoscribe/ip-resist/114589-404467.html

[31] K. Takada, H. B. Sun, S. Kawata, Appl. Phys Lett. 2005, 86, 071122.

[32] A. Ovsianikov, J. Viertl, B. Chichkov, M. Oubaha, B. MacCraith, I. Sakellari, A. Giakoumaki, D. Gray, M. Vamvakaki, M. Farsari, ACS Nano 2008, 2, 2257.

[33] J. S. Oakdale, J. Ye, W. L. Smith, J. Biener, Opt. Express 2016, 24, 27077.

[34] D. D. Han, Y. L. Zhang, J. N. Ma, Y. Q. Liu, B. Han, H. B. Sun, Adv. Mater. 2016, 28, 8328.

[35] K. Y. Lee, D. J. Mooney, Chem. Rev. 2001, 101, 1869.

[36] T. R. Hoare, D. S. Kohane, Polymer 2008, 49, 1993.

[37] L. Ionov, Mater. Today 2014, 17, 494.

[38] R. A. Barry III, R. F. Shepherd, J. N. Hanson, R. G. Nuzzo, P. Wiltzius, J. A. Lewis, Adv. Mater. 2009, 21(23), 2407-2410.

[39] J. L. Connell, E. T. Ritschdorff, J. B. Shear, Anal. Chem. 2016, 88, 12264.

[40] E. Kapyla, T. Sedlacik, D. B. Aydogan, J. Viitanen, F. Rypacek, M. Kellomaki, Mater. Sci. Eng. C. 2014, 43, 280.

[41] P. G. de Gennes, Acad. Sci. Paris 1975, 281b, 101.

[42] P. G. de Gennes, Acad. Sci. Paris IIB 1997, 324, 343.

[43] J. P. Cotton, F. Hardouin, Prog. Polym. Sci. 1997, 22, 795-828.

[44] M. Warner and E. M. Terentjev. Liquid crystal elastomers. Vol. 120. OUP Oxford, 2003.

[45] T. J. White, D. J. Broer, Nat. Mater. 2015, 14, 1087-1098.

[46] D. J. Broer, J. Boven, G. N. Mol, G. Challa, Makromol. Chem. 1989, 190, 2255-2268.

[47] T. Ikeda, J.-i. Mamiya, Y. Yu, Angew. Chem., Int. Ed. 2007, 46, 506-528.

[48] J.Küpfer, H. Finkelmann, Makromol. Chem., Rapid Commun. 1991, 12, 717-726.

[49] T. J. White, D. J. Broer, Nat. Mater. 2015, 14, 1087.

[50] G. N. Mol, K. D. Harris, C. W. Bastiaansen, D. J. Broer, Adv. Funct. Mater. 2005, 15, 1155.

[51] J. J. Wie, K. M. Lee, T. H. Ware, T. J. White, Macromolecules 2015, 48, 1087.

[52] S. Nocentini, D. Martella, D. S. Wiersma, C. Parmeggiani, Soft Matter 2017, 13, 8590.

[53] H. Zeng, D. Martella, P. Wasylczyk, G. Cerretti, J. C. G. Lavocat, C. H. Ho, C. Parmeggiani, D. S. Wiersma, Adv. Mater. 2014, 26, 2319.

[54] A. M. Flatae, M. Burresi, H. Zeng, S. Nocentini, S. Wiegele, C. Parmeggiani, H. Kalt, D. Wiersma, Light: Sci. Appl. 2015, 4, e282.

[55] S. Nocentini, D. Martella, C. Parmeggiani, S. Zanotto, D. S. Wiersma, Adv. Opt. Mater. 2018, 6, 1800167.

[56] S. Nocentini, F. Riboli, M. Burresi, D. Martella, C. Parmeggiani, D. S. Wiersma, ACS Photonics 2018, 5, 3222.

[57] D. Martella, D. Antonioli, S. Nocentini, D. S. Wiersma, G. Galli, M. Laus, C. Parmeggiani, RSC Adv. 2017, 7, 19940.

[58] T. Ikeda, J. I. Mamiya, Y. Yu, Angew. Chem., Int. Ed. 2007, 46, 506.

[59] H. Koerner, T. J. White, N. V. Tabiryan, T. J. Bunning, R. A. Vaia, Mater. Today 2008, 11, 34.

[60] H. Yu, T. Ikeda, Adv. Mater. 2011, 23, 2149.

[61] J. Wei, Y. Yu, Soft Matter 2012, 8, 8050.

[62] L. Dong, Y. Zhao, Mater. Chem. Front. 2018, 2, 1932.

[63] D. Martella, S. Nocentini, D. S. Wiersma, C. Parmeggiani, Soft Matter 2019, 15, 1312.

[64] D. Martella, S. Nocentini, D. Nuzhdin, C. Parmeggiani, D. S. Wiersma, Adv. Mater. 2017, 29, 1704047.

[65] A. H. Gelebart, G. Vantomme, E. W. Meijer, D. J. Broer, Adv. Mater. 2017, 29, 1606712.

[66] S. Nocentini, D. Martella, C. Parmeggiani, D. S. Wiersma, Materials 2016, 9, 525.

Chapter 2

2 Tunable Optics and Photonics

Chapter 2 introduces recent developments in 3D printing with a particular focus on static and tunable optics and photonics. Combining printable smart material and high resolution 3D printing might provide a unique platform for active and reconfigurable structures. This approach can introduce unprecedented opportunities in optics and photonics for future applications in freeform optics, integrated optical and optoelectronic devices, displays, optical sensors, antennas, active and tunable photonic devices, and biomedicine.

Finally, we will focus on the description of the recent advances of Direct Laser Writing in the field of light-tunable photonics, showing as polymers, with a particular attention on Liquid Crystalline Networks, are used not only as passive elements for guiding and manipulating light but also to dynamically control the optical properties of the devices themselves.

2.1 3D printing for optics and photonics

3D printing is a powerful technique for customized, complex optical components and it has been employed for the fabrication of opto-mechanical components [1], photonic crystal fibers and waveguides [2], gratings, and lenses [3, 4]. One of the great advantages of 3D printing is the possibility to be integrated on different substrates or using different materials in a multi-step process without additional assembling procedures. Moreover, various freeform optical components, that cannot be achieved with conventional lithographic techniques (UV lithography, electron beam lithography), usually limited to planar geometries, can be fabricated [5-9] also with complex features along the out-of-plane direction.

3D printing of integrated optical components has been recently developed in a variety of optical fields [10-13]. An interesting example, concerning the daily life, could be the advances in the design of freeform systems for imaging and

illumination applications, such as the head-mounted displays for virtual reality and augmented reality [14, 15].

2.2 3D printing for responsive structures

3D printing of "smart materials" is a valid method for the fabrication of stimuli-responsive structures.

Here we report a couple of examples in which 3D printing has been combined with responsive polymers for optical applications. In Figure 2.1, the working mechanism of a smart polymeric grating controlled via temperature is reported. By employing fused deposition modeling printing, which enables a spatial resolution of micrometers and, therefore, it is suitable for the fabrication of microwave active structures, a shape memory polymeric beam array, made of a thermoplastic material (polylactide (PLA)), has been fabricated. PLA is a well-known material for fused deposition modeling printing and has a clear shape-memory property. This resonant structure after fabrication is characterized by a broad resonance due to the PLA/grating disordered lattice. This inhomogeneity can be removed by heating the structure above the PLA glass-transition temperature at which the lattice becomes ordered. In this way, the spectral response of the microwave grating can be tuned and it exhibits sharp Fano resonance at (38-40) GHz as designed [16]. An important advantage of this system is that this stimuli-responsive action occurs because of temperature dependent material properties, thus does not requiring an electric power supply.

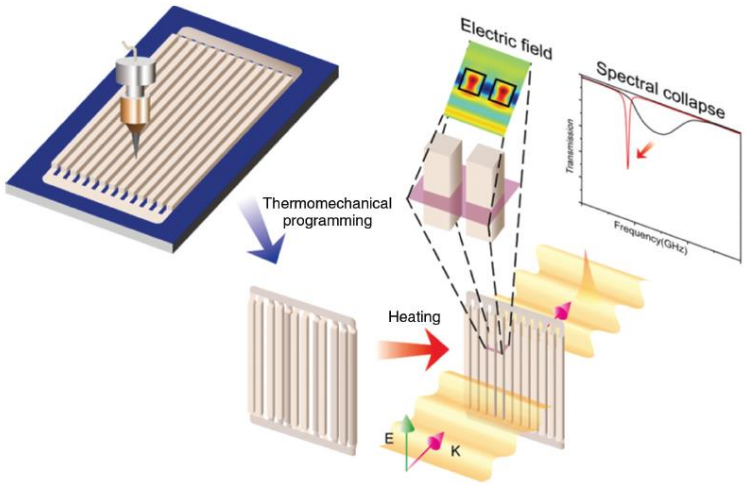

Figure 2.1. Shape memory polymeric photonic structure: the disordered lattice does not exhibit a sharp spectral resonance. When it is heated above the glass

transition temperature, the lattice becomes ordered, exhibiting a sharp Fano resonance. Adapted from reference [16].

With respect to temperature as well as, heat, humidity, pH variations, light has the advantage to remotely activate the material switching, enabling a local control on the structures. This means that light can be locally focused or light patterns can be projected on specific microstructures without illuminating the whole sample. Moreover, properties of light as intensity, polarization, wavelength, can be adjusted to control the material response [17-20]. Among the photo-responsive molecules used to introduce an optical control, azobenzenes are widely employed because of the isomerization process of azobenzene molecules, that under illumination at certain wavelengths (typically in the UV region), consists in a reversible switching among the two molecular state: the *trans* state in which the molecule is stretched along its molecular axis (rest/stable/minimal energy state) and the cis state in which the molecule bends around the isomer in a metastable state [21]. A recent application of photoresponsive polymers with 3D printing allowed the demonstration of smart window (Figure 2.2.a) [22], made of azobenzene compounds mixed with photopolymer liquid resins for stereolithography. Their optical characterization, made with crossed polarizers, showed as without optical pumping, there was no transmission through the window. Introducing a laser light pumping, optical anisotropy was induced, because of the trans-cis transformation of the azobenzene compounds (Figure 2.2.b), leading to the polarization rotation of the incident light with a consequent increase of the transmission through the window. When the pumping light is turned off, the azobenzene compounds reversibly returns into the trans state with a consequent decrease of the transmission. It was possible to modulate the transmitted beam with a frequency of 100 Hz (Figure 2.2.c).

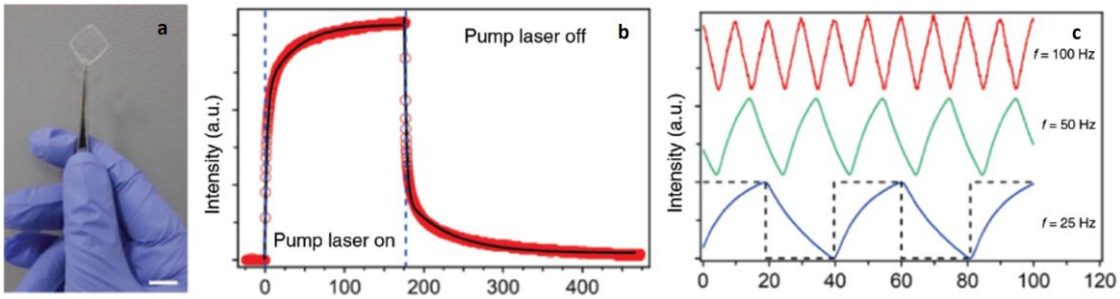

Figure 2.2. a) Photograph of the optical window realized by stereolithography (scale bar: 1 mm). b) Intensity value with the 532 nm pump laser turned on and

off. C) Modulation of the transmitted beam was demonstrated up to 100 Hz. Adapted from reference [22].

Between different 3D printing methods, DLW, based on multi-photon absorption polymerization, enables a high resolution (around 100 nm) if it is compared to the other 3D printing techniques, previously described [23]. In DLW the structure resolution is the minimum size of the voxel minor axis that can be fabricated for each laser power and writing speed. Taking advantage of this aspect, DLW has been widely used in optics and photonics to fabricate various nanophotonic structures and optical metamaterials, such as log-pile photonic crystals [24], spiral photonic crystals, 3D split-ring metamaterials [25] and U-shaped resonators [26].

2.3 Static photonic devices fabricated by DLW

The potentiality of DLW to create three dimensional structures in one step process, reaching nanometric resolution with respect to the lithographic techniques of the past, has enabled the fabrication of 3D microscopic photonic crystals, such as woodpiles (Figure 2.3.a), both for the near infrared and visible spectrum [27-29]. Moreover, the possibility to reproduce computer programmed designs has enabled to realize several complicated morphologies [30, 31], such as chiral structures to control the polarized light propagation [32, 33], quasi-crystals or amorphous photonic crystals [34-36] (Figure 2.3.b-d). However, a limit of polymeric materials for photonic applications is their low refractive index of about 1.5. Therefore, in order to solve this problem, increasing the refractive index contrast with respect to the air, photonic crystals have been fabricated in polymeric matrices, used as a template for single or double inversion into higher refractive index materials as silicon, titania, titanium dioxide or in chalcogenide glasses [37, 38, 39]. In addition, direct laser writing enables both photonic integration between different platforms, as the interconnection of integrated planar circuits [40-43], and exploiting the third space dimension (Figure 2.3.e). Other photonics structures as whispering gallery mode cavities (Figure 2.3.f) [43, 44], plasmonic crystals [45], metamaterials [46], cloaking structures [47], and micro-optical components [48] were fabricated via DLW, which has been demonstrated a very versatile technique and a useful method

that can be combined with "smart materials" to realize stimuli responsive structures.

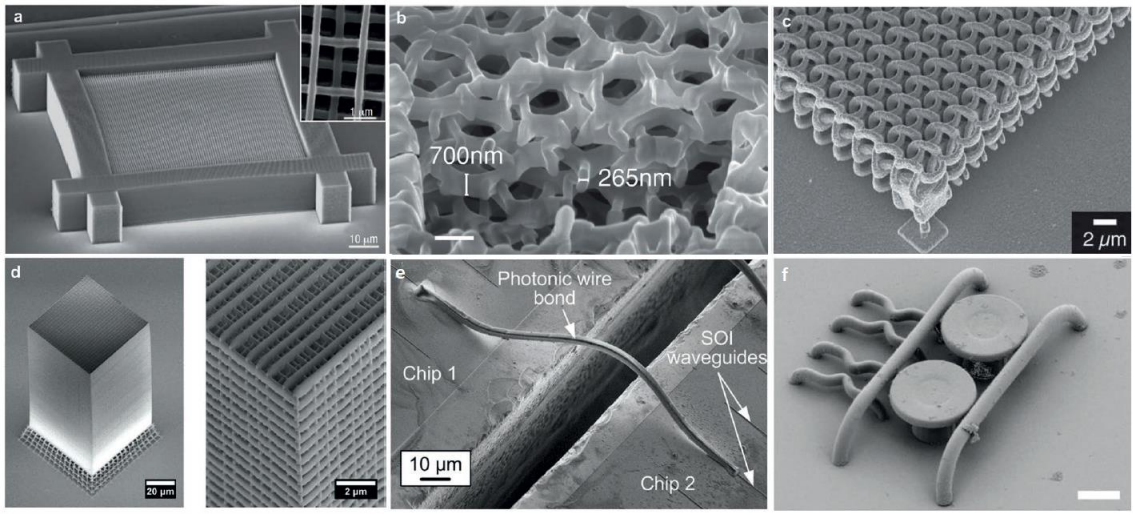

Figure 2.3. SEM images of photonic structures fabricated by DLW. a) A photonic crystal woodpile for telecom wavelengths. Adapted from reference [20]. b) A silicon hyperuniform disordered material. Adapted from reference [29]. c) A bichiral plasmonic crystal with right-handed corners and right-handed helices after electroless silver plating. Adapted from reference [37]. d) A deterministic aperiodic structure made by two-dimensional square Fibonacci tiling. Adapted from reference [24]. e) Photonic wire bonds for chip-to-chip interconnections. Adapted from reference [34]. f) Waveguides, couplers and micro-disc resonators in nanodiamond photoresist. Scale bar: 5 µm. Adapted from reference [35].

2.4 Different stimuli to control photonic micro-devices made via DLW

In photonics, light tunability of the optical properties directly depends on modulation of refractive index of the structure. This can be done by electro-optical effect of the matrix [49-51], by introducing liquid crystals [52, 53], phase changing materials, or many other effects [54-58]. In photonic platforms, tunability has been also successfully obtained by the introduction of photo responsive matter/polymers. In particular, two different strategies have been followed: controlling the matrix refractive index or modulating the spectral property by a geometrical elastic reshaping.

In the field of stimuli responsive optical devices, according to the type of environment, several stimuli are used for controlling shape changing materials. We

report here several examples of polymeric structures fabricated via DLW whose optical properties can be tuned by different stimuli. For example, recently, photonic microstructures have been fabricated by DLW in hydrogel or polydimethylsiloxane (PDMS) and controlled via pH, solvent concentration, and temperature [59-61].

The simpler tunable optical component that has been reported is a micro lens made by the cross-linking of bovine serum albumin, enabling the realization of 3D smooth convex microlenses, whose focal distance was tuned regularly and reversibly by changing the pH value [62]. Photonic devices based on proteins have a good biodegradability and can be fabricated on flexible substrates as PDMS [63]. Moreover, PDMS is also used as a polymeric matrix for micro-optics due to it is optically clear, chemically inert, non-toxic, and biologically compatible. As an example, PDMS micro-lenses have been integrated in microfluidic circuits by DLW without the use of any mask or duplicated templates. The focal length has been tuned by changing the curvature of the lenses exploiting the swelling of PDMS in a solvent [62].

The tuning of the properties can be achieved not only by swelling but also employing the modulation of the refractive index as in case of a tunable 3D photonic woodpile, written starting from an oligo(aniline)-diacrylate monomer [64]. The resulting polyaniline was switched from a dielectric (emeraldine base) to a conducting (emeraldine salt) state by well-known redox process, thus changing its refractive index with a negligible corresponding dimensional change. Despite this interesting optical property control, the tunability of the fabricated 3D woodpile structure was not reported, making this strategy not yet practically applicable to active devices.

Synthetic poly(ethylene glycol) diacrylate (PEG-DA) hydrogel-based photonic microcavities, controlled by changing the environmental humidity, has been also demonstrated [65]. Two rhodamine-B doped PEG-DA hydrogel-based photonic microcavities, prepared using DLW, are able to produce standard whispering-gallery mode emissions with a low threshold (0.50 $\mu J/cm^2$) and a high quality factor (about 2.9×10^3). Moreover, PEG-DA hydrogel-based microcavities can expand or shrink uniformly, in conditions of increasing or decreasing relative humidity. In particular, when the humidity is high the two microcavities close up and couple to each other. As a consequent, the resulting lasing spectrum shows a significant decrease in the number of laser peaks and a red-shift.

Finally, we cite two examples in which the polymeric structure has been fabricated via DLW in a rigid polymer, while the optical properties tuning was obtained thanks to the introduction of liquid crystals inside the structure and using temperature as the external stimulus to tune the liquid crystal phase transition.

The first example is a tunable-focus liquid crystal microlens array, realized by two-photon polymerization based direct-laser writing [66]. Such microlens array is composed by glassy polymer lenses covered with a liquid crystalline mixture which creates inhomogeneous electric field distribution and homogeneous-like liquid-crystal alignment, simultaneously. The phase profile and thus the focal length can be tuned by the applied voltage.

The second example is a 3D woodpile photonic crystal, fabricated by DLW in a negative photoresist, IP-Dip™ (Nanoscribe GmbH) and filled with liquid crystals, which demonstrated the possibility of switching between different patterns of light beams transmitted through the photonic structure (Figure 2.4) by changes of temperature [67].

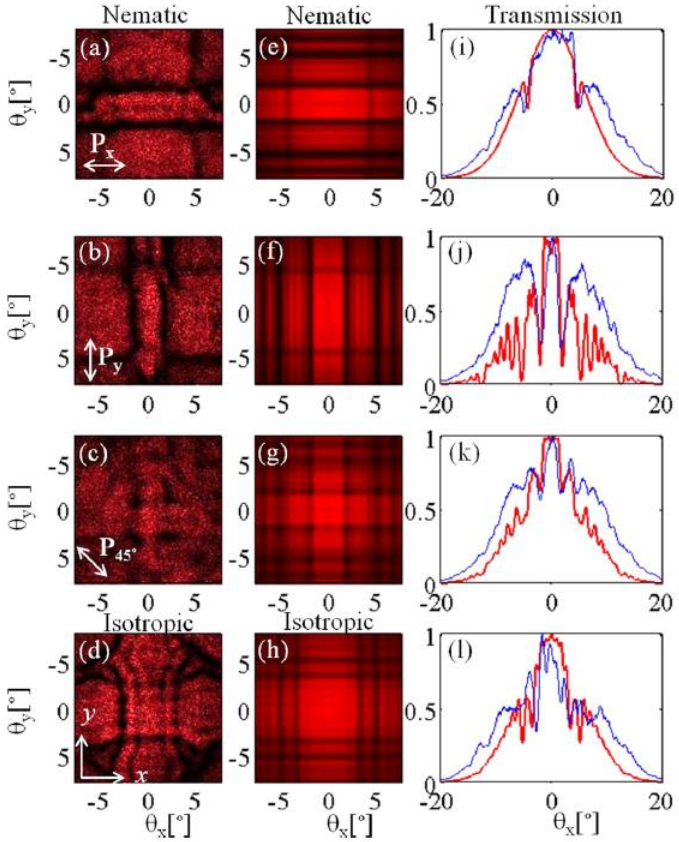

Figure 2.4. 2D far field distributions of the central part beam as obtained by measurements ((a)-(d)) and finite-difference time-domain (FDTD) calculations ((e)-(h)) according to the polarization. The right column ((i)-(l)) compares the 1D intensity distributions along the x direction (integrated along the y direction)

obtained from experiments (blue-solid) and from FDTD numerics (red-solid). Adapted from reference [67].

In fact, the phase transition between the nematic and isotropic states of the infiltrated LC mixture causes a remarkable change in spatial distribution of the propagating light beam. The transmission profiles in the nematic phase also show polarization sensivity due to the dependence of the effective refractive index of LCs on the angle between the LC director and the vector of light polarization.

2.5 Liquid crystalline elastomeric devices fabricated via DLW for tunable photonics

We focus now on liquid crystal based responsive structures activated by temperature and/or light and patterned via DLW. In the palette of responsive polymers, Liquid Crystalline Networks (LCNs) present many opportunities for tunable photonic devices thanks to their ability to reversibly deform and change their birefringence under an external temperature or light. Several examples about the shape-changing properties of the LCNs, patterned by DLW, which affect the optical properties of the structure and modulated by light or temperature, are now reported.

Recently, a supramolecular cholesteric liquid crystalline photonic photoresist, which exhibits a self-organized helical photonic structure that can selectively reflect light [68], has been adopted for the fabrication of 4D photonic microactuators, such as pillars, flowers, and butterflies, with submicron resolution. These micron-sized features displayed structural color and shape changes triggered by a variation of humidity or temperature (Figure 2.5) [69], generating a shift in the reflection band as a result of an anisotropic shape change of the cholesteric helix.

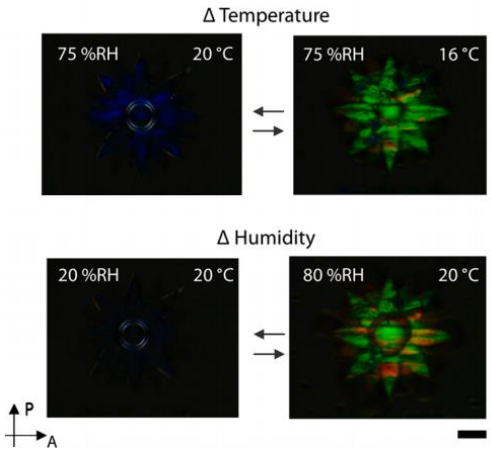

Figure 2.5. Crossed polarized optical images of the flower showing the direct (triggered by humidity) or indirect (triggered by temperature), induced color changes. Adapted from reference [69].

Another example refers to microscale color pixels with sizes as small as 15 µm × 15 µm LCE pixels, showing colors in visible range (Figure 2.6). They have been very recently designed from well-controlled thickness of LCEs, enabled by DLW system. The rotation of LCE films does not change the color but change the color brightness, while tilting of LCE films below 15° does not cause a color shifting. However, a dynamic switching of colors with change of temperature has been demonstrated [70]. These dynamic colors generated by birefringence variation opens to LCE applications in temperature sensing and information encryption.

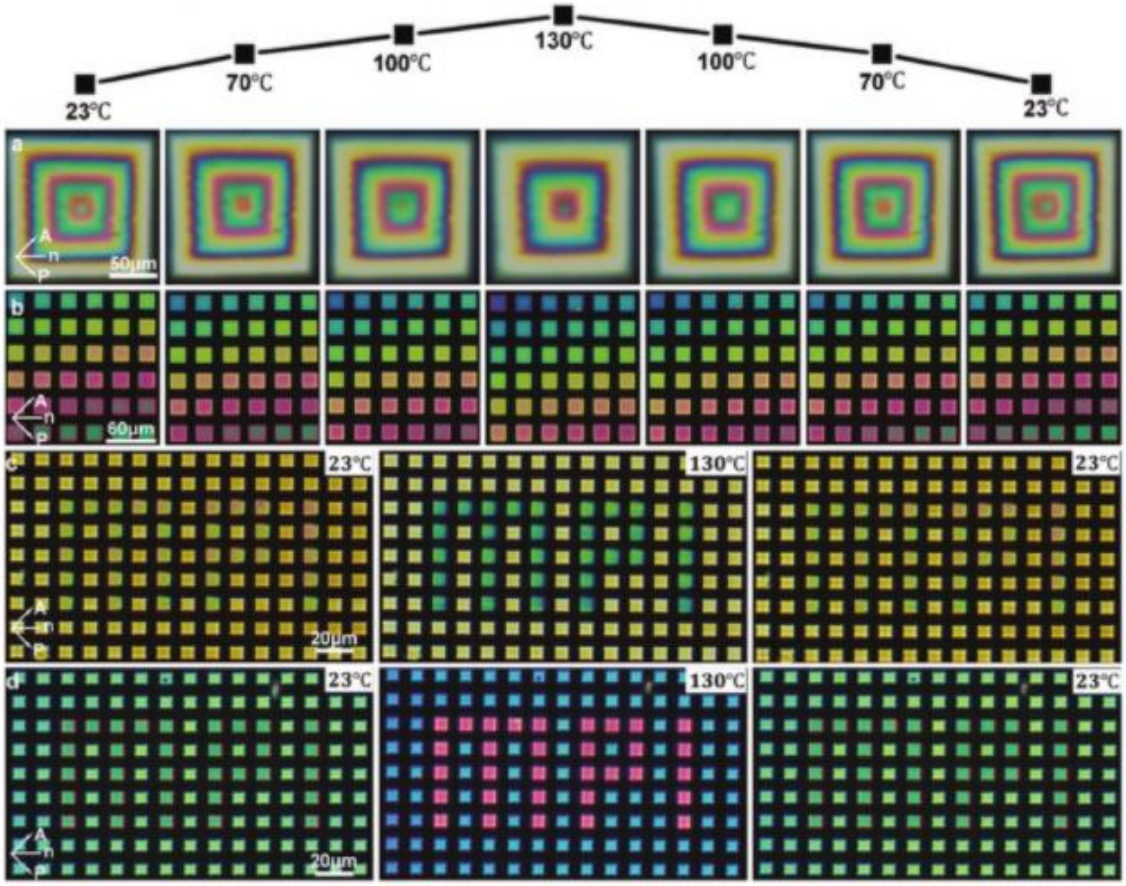

Figure 2.6. Switching of the LCE colors with temperature. a) POM images of a LCE pyramid with 10 µm height in a heating process. b) POM images of the LCE films with designed thicknesses from 4.7 µm to 8.2 µm during a heating process. c, d) Hide-and-show demonstration of "MPI" patterns during a heating and cooling process. Adapted from reference [70].

Another example is reported in Figure 2.7.a, where a polymeric micro-goblet whispering gallery mode resonator (WGMR) with an optically controlled and stable reversible tunability has been demonstrated [71]. The nematically ordered elastomeric cylinder, fabricated by DLW and placed on the top of a high Q dye-doped Polymethyl Methaclyrate (PMMA) microdisk resonator, worked as a transducer, converting the light activation into a mechanical stress that slightly varied the radius of the cavity. The mechanical and elastic reshaping of the resonators, enabled by a low pump power activation, led to a fully reversible tuning of the modes. Increasing the excitation energy leads also to a reversible red shift of the modes.

In Figure 2.7.b is reported another example of a waveguide vertically coupled to a WGMR that has been fabricated by 3D patterning of a commercial glassy polymer is shown. A LCN cylinder has been fabricated by a second writing step on the top of the IP-Dip™ cavity, creating an elastic cylindrical actuator. This architecture allows for a small, gentle and reversible deformation of the IP-Dip™ resonator when the LCN are activated via the light stimulus, thanks to the tangent pressure that the LCN actuator impresses on the underlying cavity. A controlled mechanical deformation reflects in the spectral red shift of the resonant wavelength, creating a tunable filtering effect [72].

Photonic structures can be also directly manufactured in a LCN matrix, as in case of a squared diffraction grating made of LCNs and realized by DLW (1.5 micron periodicity, Figure 2.7.c). A reversible deformation of the LCN grating is achieved in a controlled way upon illumination. When the light is turned on, the structure periodicity changed causing the deviation angle of the diffracted beams [73].

An example of material properties control by refractive index variation is the realization by DLW of photo-responsive suspended micro-membranes within an amorphous Bisphenol A derived matrix (Figure 2.7.d) [74]. Thanks to the incorporation of azobenzene units, the membranes exhibited a remarkable mechanical photo-responsivity despite the disordered, amorphous structure of the cross-linked network. The interferometric method allowed to measure the phase modulation of the transmitted beam through the membrane. The phase variation was obtained as a consequence of the shape refractive index decrease.

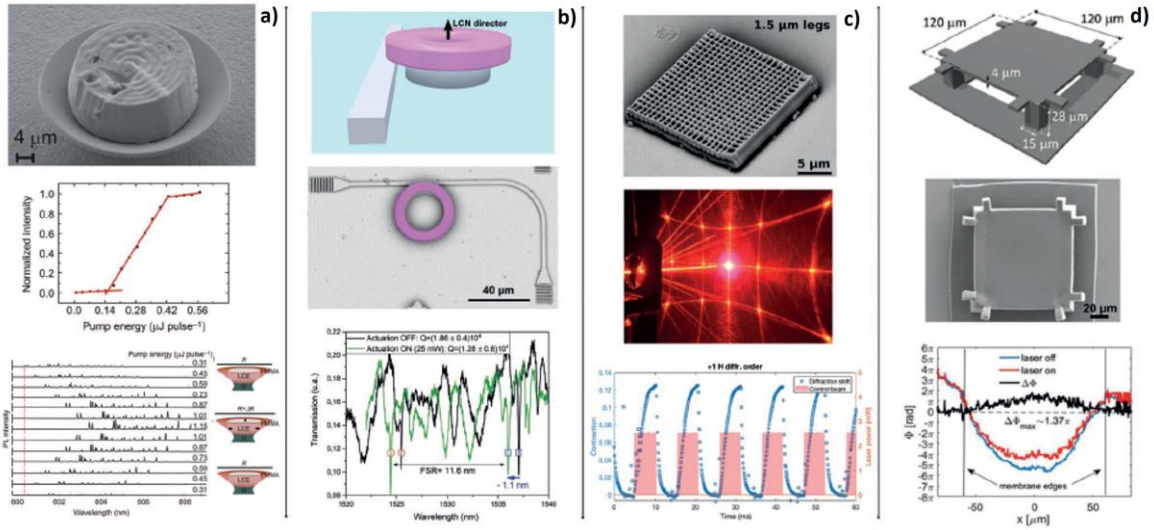

Figure 2.7. Light responsive photonic structures fabricated by DLW. a) From top to bottom: SEM image of a microdisk laser with a LCN cylindric actuator on the top, input-output curve of a dye-doped goblet micro-laser, and photo-induced tuning of LCN/microdisk laser modes for different pump energies. Adapted from reference [71]. b) Rendering (top image), SEM image (top view, false color for the LCN element) in the center, and on the bottom transmission spectrum of the waveguide coupled to LCN ring resonator. The black line spectrum is recorded without any activation of the LCN cavity, while the green one corresponds to the light-activated blue shift of the resonance. Adapted from reference [72]. c) SEM image of the LCN micro grating operating as a beam steerer (top panel), optical image of the diffracted beams (in the center), and temporal dynamics of the normalized deflection of the first diffraction order for an actuation power of 2.8 mW (bottom panel). Adapted from reference [73]. d) From top to bottom: sketch of the membrane layout, electron microscope image of the fabricated suspended membrane, and cross-sectional phase profiles along a horizontal cut passing at the membrane center induced by light irradiation. Adapted from reference [74].

References

[1] L. J. Salazar-Serrano, J. P. Torres, A. Valencia, PLoS One 2017, 2, e0169832.

[2] A. Kaur, J. C. Myers, M. I. M. Ghazali, J. Byford, P. Chahal Affordable terahertz components using 3D printing. In: IEEE 65th Electronic Components and Technology Conference, 2015.

[3] V. L. Iezzi, J. Boisvert, S. Loranger, R. Kashyap, Opt. Lett. 2016, 8, 1865-68.

[4] A. D. Squires, E. Constable, R. A. Lewis, J. Infrared Milli. Terahz. Waves 2015, 36, 72-80.

[5] K. Garrard, T. Bruegge, J. Hoffman, T. Dow, A. Sohn, Design tools for freeform optics. In: Current developments in lens design and optical engineering VI, International Society for Optics and Photonics, 2005.

[6] F. Fang, Y. Cheng, X. Zhang, Adv. Opt. Technol. 2013, 2, 445-53.

[7] T. L. R. Davenport. 3D NURBS representation of surfaces for illumination. In: International Optical Design Conference 2002, International Society for Optics and Photonics, 2002.

[8] W. J. Cassarly, M. J. Hayford. Illumination optimization: the revolution has begun. In: International Optical Design Conference 2002, International Society for Optics and Photonics, 2002.

[9] I. Kaya, J. P. Rolland, A radial basis function method for freeform optics surfaces. In: Frontiers in Optics, Optical Society of America, 2010.

[10] A. M. Herkommer, J. Opt. 2014, 43, 261-8.

[11] K. Brix, Y. Hafizogullari, A. Platen, JOSA A 2015, 32, 2227-36.

[12] J. Lim, Y. K. Kim, D. Won, I. H. Choi, S. Lee, J. Kim, Adv. Mater. Technol. 2019, 4, 1900118.

[13] S. H. Park, R. Su, J. Jeong, S.-Z. Guo, K. Daeha, F. Meng, M. C. McAlpine, Adv. Mater. 2018, 30, 1803980.

[14] H. S. An, Y. G. Park, K. Kim, Y. S. Nam, M. H. Song, J. U. Park, Adv. Sci. 2019, 1901603.

[15] K. Willis, E. Brockmeyer, S. Hudson, I. Poupyrev, Printed optics: 3D printing of embedded optical elements for interactive devices. In: Proceedings of the 25th annual ACM symposium on User interface software and technology. Washington, DC, USA, ACM, 2012.

[16] S. C. An, E. Lee, C.-H. Lee, H. Y. Jeong, T.-S. Kwon, J.-H. Lee, Y. C. Yun, Adv. Opt. Mater. 2019, 7, 1801206.

[17] A. M. Flatae, M. Burresi, H. Zeng, S. Nocentini, S. Wiegele, C. Parmeggiani, H. Kalt, D. S. Wiersma, Light Sci. Appl. 2015, 4, e282.

[18] H. Zeng, D. Martella, P. Wasylczyk, G. Cerretti, J. C. Lavocat, C. H. Ho, C. Parmeggiani, D. S. Wiersma, Adv. Mater. 2014, 26, 2319-22.

[19] S. Nocentini, D. Martella, C. Parmeggiani, S. Zanotto, D. S. Wiersma, Adv. Opt. Mater. 2018, 6, 1800167.

[20] I. De Bellis, D. Martella, C. Parmeggiani, E. Pugliese, M. Locatelli, R. Meucci, D. S. Wiersma, S. Nocentini, J. Phys. Chem. C 2019, 123, 26522-7.

[21] G. S. Kumar, D. C. Neckers, Chem. Rev. 1989, 89, 1915-25.

[22] A. Szukalski, S. Uttiya, F. D'Elia, A, Portone, D. Pisignano, L. Persano, A. Camposeo, 3D photo-responsive optical devices manufactured by advanced printing technologies. In: Organic Photonic Materials and Devices XXI. International Society for Optics and Photonics, 2019.

[23] S. Maruo, J. T. Fourkas, Laser Photonics Rev. 2008, 2, 100-11.

[24] R. Guo, Z. Li, Z. Jiang, D. Yuan, W. Huang, A. Xia, J. Opt. A: Pure Appl. Opt. 2005, 7, 396.

[25] M. Farsari, B. N. Chichkov, Nat. Photonics 2009, 3, 450.

[26] X. Xiong, Z.-H. Xue, C. Meng, S. Jiang, Y.-H. Hu, R.-W. Peng, M. Wang, Phys. Rev. B 2013, 88, 115105.

[27] M. Deubel, G. Von Freymann, M. Wegener, S. Pereira, K. Busch, C. M. Soukoulis, Nat. Mater. 2004, 3, 444.

[28] T. F. Scott, C. J. Kloxin, D. L. Forman, R. R. McLeod, C. N. Bowman, J. Mater. Chem. 2011, 21, 14150.

[29] S. Wong, M. Deubel, F. Pérez-Willard, S. John, G. A. Ozin, M. Wegener, G. von Freymann, Adv. Mater. 2006, 18, 265.

[30] Y. Li, D. B. Fullager, S. Park, D. Childers, R. Fesperman, G. Boreman, T. Hofmann, Opt. Lett. 2018, 43, 4711.

[31] M. Renner, G. von Freymann, Adv. Opt. Mater. 2014, 2, 226.

[32] M. Thiel, M. Decker, M. Deubel, M. Wegener, S. Linden, G. von Freymann, Adv. Mater. 2007, 19, 207.

[33] M. Thiel, M. S. Rill, G. von Freymann, M. Wegener, Adv. Mater. 2009, 21, 4680.

[34] A. Ledermann, L. Cademartiri, M. Hermatschweiler, C. Toninelli, G. A. Ozin, D. S. Wiersma, M. Wegener, G. von Freymann, Nat. Mater. 2006, 5, 942.

[35] A. Ledermann, D. S. Wiersma, M. Wegener, G. von Freymann, Opt. Express 2009, 17, 1844.

[36] N. Muller, J. Haberko, C. Marichy, F. Scheffold, Adv. Opt. Mater. 2014, 2, 115.

[37] C. Marichy, N. Muller, L. S. Froufe-Pérez, F. Scheffold, Sci. Rep. 2016, 6, 21818.

[38] I. Staude, M. Thiel, S. Essig, C. Wolff, K. Busch, G. Von Freymann, M. Wegener, Opt. Lett. 2010, 35, 1094.

[39] S. Wong, M. Deubel, F. Pérez-Willard, S. John, G. A. Ozin, M. Wegener, and G. von Freymann, Adv. Mater. 2006, 18, 265-269.

[40] M. Schumann, T. Bückmann, N. Gruhler, M. Wegener, W. Pernice, Light: Sci. Appl. 2014, 3, e175.

[41] P. I. Dietrich, M. Blaicher, I. Reuter, M. Billah, T. Hoose, A. Hofmann, C. Caer, R. Dangel, B. Offrein, U. Troppenz, M. Moehrle, Nat. Photonics 2018, 12, 241.

[42] N. Lindenmann, G. Balthasar, D. Hillerkuss, R. Schmogrow, M. Jordan, J. Leuthold, W. Freude, C. Koos, Opt. Express 2012, 20, 17667.

[43] A. W. Schell, J. Kaschke, J. Fischer, R. Henze, J. Wolters, M. Wegener, O. Benson, Sci. Rep. 2013, 3, 1577.

[44] T. Grossmann, S. Schleede, M. Hauser, T. Beck, M. Thiel, G. von Freymann, T. Mappes, H. Kalt, Opt. Express 2011, 19, 11451.

[45] A. Radke, T. Gissibl, T. Klotzbücher, P. V. Braun, H. Giessen, Adv. Mater. 2011, 23, 3018.

[46] M. S. Rill, C. Plet, M. Thiel, I. Staude, G. Von Freymann, S. Linden, M. Wegener, Nat. Mater. 2008, 7, 543.

[47] T. Ergin, N. Stenger, P. Brenner, J. B. Pendry, M. Wegener, Science 2010, 328, 337.

[48] T. Gissibl, S. Thiele, A. Herkommer, H. Giessen, Nat. Photonics 2016, 10, 554.

[49] L. Alloatti, R. Palmer, S. Diebold, K. P. Pahl, B. Chen, R. Dinu, M. Fournier, J. M. Fedeli, T. Zwick, W. Freude, C. Koos, J. Leuthold, Light: Sci. Appl. 2014, 3, e173.

[50] M. Lee, H. E. Katz, C. Erben, D. M. Gill, P. Gopalan, J. D. Heber, D. J. McGee, Science 2002, 298, 1401.

[51] A. Guarino, G. Poberaj, D. Rezzonico, R. Degl'Innocenti, P. Günter, Nat. Photonics 2007, 1, 407.

[52] L. Wang, Q. Li, Adv. Funct. Mater. 2016, 26, 10.

[53] C. T. Wang, C. W. Tseng, J. H. Yu, Y. C. Li, C. H. Lee, H. C. Jau, M. C. Lee, Y. J. Chen, T. H. LinOpt. Express 2013, 21, 10989.

[54] Q. Wang, E. T. Rogers, B. Gholipour, C. M. Wang, G. Yuan, J. Teng, N. I. Zheludev, Nat. Photonics 2016, 10, 60.

[55] M. Wuttig, H. Bhaskaran, T. Taubner, Nat. Photonics 2017, 11, 465.

[56] Z. Li, Y. Zhou, H. Qi, Q. Pan, Z. Zhang, N. N. Shi, M. Lu, A. Stein, C. Y. Li, S. Ramanathan, N. Yu, Adv. Mater. 2016, 28, 9117.

[57] V. R. Almeida, C. A. Barrios, R. R. Panepucci, M. Lipson, Nature 2004, 431, 1081.

[58] F. Bonaccorso, Z. Sun, T. Hasan, A. C. Ferrari, Nat. Photonics 2010, 4, 611.

[59] E. Scarpa, E. D. Lemma, R. Fiammengo, M. P. Cipolla, F. Pisanello, F. Rizzi, M. De Vittorio, Sens. Actuator B - Chem. 2019, 279, 418.

[60] A. Tudor, C. Delaney, H. Zhang, A. J. Thompson, V. F. Curto, G. Z. Yang, M. J. Higgins, D. Diamond, L. Florea, Mater. Today 2018, 21, 807.

[61] D. X. Lu, Y. L. Zhang, D. D. Han, H. Wang, H. Xia, Q. D. Chen, H. Ding, H. B. Sun, J. Mater. Chem. C 2015, 3, 1751.

[62] Y. L. Sun, W. F. Dong, R. Z. Yang, X. Meng, L. Zhang, Q. D. Chen, H. B. Sun, Angew. Chem., Int. Ed. 2012, 51, 1558.

[63] Y. L. Sun, W. F. Dong, L. G. Niu, T. Jiang, D. X. Liu, L. Zhang, Y. S. Wang, Q. D. Chen, D. P. Kim, H. B. Sun, Light: Sci. Appl. 2014, 3, e129.

[64] Y. Hu, B. T. Miles, Y. L. D. Ho, M. P. Taverne, L. Chen, H. Gersen, J. G. Rarity, C. F. Faul, Adv. Opt. Mater. 2017, 5, 1600458.

[65] M.-T. Li, Z.-S. Hou, Q.-L. Huang, S. Xu, A.-W. Li, Opt. Commun. 2020, 459, 125036.

[66] Z. He, Y. H. Lee, D. Chanda, S. T. Wu, Opt. Express 2018, 26, 21184.

[67] C.-H. Ho, Y.-C. Cheng, L. Maigyte, H. Zeng, J. Trull, C. Cojocaru, D. S. Wiersma, and K. Staliunas, Appl. Phys. Lett. 2015, 106, 021113.

[68] D. J. Mukder, A. P. H. J. Schenning, C. W. M. Bastiaansen, J. Mater. Chem. C 2014, 2, 6695-6705.

[69] M. del Pozo, C. Delaney, C.W. M. Bastiaansen, D. Diamond, A. P. H. J. Schenning, and L. Florea, ACS Nano 2020, 14, 8, 9832-9839.

[70] Y. Guo, H. Shahsavan, M. Sitti, Adv. Optical Mater. 2020, 8, 1902098.

[71] A. M. Flatae, M. Burresi, H. Zeng, S. Nocentini, S. Wiegele, C. Parmeggiani, H. Kalt, D. Wiersma, Light: Sci. Appl. 2015, 4, e282.

[72] S. Nocentini, F. Riboli, M. Burresi, D. Martella, C. Parmeggiani, D. S. Wiersma, ACS Photonics 2018, 5, 3222.

[73] S. Nocentini, D. Martella, C. Parmeggiani, S. Zanotto, D. S. Wiersma, Adv. Opt. Mater. 2018, 6, 1800167.

[74] E. Descrovi, F. Pirani, V. P. Rajamanickam, S. Licheri, C. Liberale, J. Mater. Chem. C 2018, 6, 10428.

Chapter 3

3 Modulation of optical properties in Liquid Crystalline Networks across different length scales

Photopolymerization of customized materials became a well-established technique for micro- and nano-fabrication of photonic structures and their optical properties as the refractive index should be precisely tailored to design specific photonic features. For this purpose, the refractive index determination in macroscopic samples is not exhaustive and an in-situ characterization is thus necessary both at the macro and micro scale to point out how different polymerization processes differently modulate the optical properties. In particular, Chapter 3 is focused on the determination of the refractive indices of the employed Liquid Crystalline Networks (LCNs), which have been studied as birefringent materials whose tunable response is of interest for applications in different fields such as in robotics, biomedicine and photonics. By tuning the molecular composition of LCN mixtures, e.g. modifying the cross-linker and dye amount inside the polymer network, the refractive index and the optical anisotropy of microscopic and macroscopic samples have been engineered and measured by a refractometer method in dependence of temperature or light actuation stimuli. Monitoring the refractive index at different length scales showed as two photon polymerization increases the birefringence in microscopic structures and the maximum variation of the optical anisotropy is achieved by a remote laser light stimulus.

3.1 Methods to measure material birefringence

The application of LCNs in photonics has been demonstrated in different structures such as 3D integrated circuits or suspended 2D geometries [1, 2] that have been patterned at the micro-scale by Direct Laser Writing [3-5]. Customized

LCNs [5] were printed in 3D designs with nanoscale features (around 160 nm) comparable with those ones obtained by commercial resists [6].

In order to optimize the structure design and the tunability of LCN photonic devices, the refractive index and the tunable optical anisotropy (determined by the chemical composition of the material, the fabrication parameters and the molecular ordering) should be precisely known.

While the geometrical reshaping of LCN microstructures during the phase transition can be monitored by optical microscopy, their birefringence is difficult to be dynamically measured at the microscale. The commonly used techniques to measure birefringence of liquid crystals are voltage- or wavelength-dependent phase retardation [7], interferometric [8, 9] and optical transmittance methods [10]. The birefringence dependence on the LC disordering has been previously characterized in the visible range in different anisotropic matrices [11-14], showing as the optical anisotropy can be maximised by improving the order parameter of the LC polymers, e.g. by increasing the conjugation of molecular structures [15]. On the other side, the well-established technique of ellipsometry cannot be directly applied to our wedge-cell. Only few methods, e.g. the Talbot-Rayleigh [16], Abbe refractometer [12] and the wedged cell refractometer [17-19] are thus available for individually measuring the extraordinary and ordinary refractive indices in the NIR region, the spectral range of interest for telecommunication applications.

3.2 Wedge-cell refractometer method

We have investigated the optical properties of different LCN matrices by using a characterization technique that allows to extrapolate the ordinary and extraordinary refractive index and the optical anisotropy under different stimuli, such as temperature and light, at telecom wavelength. An in-situ measurement based on the wedge-cell refractometer method allowed a direct comparison of the refractive index at different length scales, both in case of macroscopic samples prepared by UV LED lamp and micro-structures fabricated by DLW.

The refractometer method exploits the propagation of a collimated laser beam polarized at 45° with respect to the LCN director. The measurement principle consists in the evaluation of the deviation angle experienced by the laser beam due to the refraction impressed by the LC polymer wedge. When the laser beam (R_{ref}) passes through the wedged birefringent materials, it splits into two rays, the

ordinary (R_o) and the extraordinary one (R_e) - being affected by the two refractive indices, n_o and n_e – whose deviation is recorded on a NIR camera at a fixed distance.

3.2.1 Experimental set up

An in-situ measurement of the refractive indices of Liquid Crystalline Networks (LCNs) at telecom wavelengths was performed by the wedge-cell refractometer method whose mechanism principle is reported in Figure 3.1.a. The measurements have been performed in case of macroscopic samples and micro-structures. In Figure 3.1.b, the experimental setup used for the characterization of the LCN micro wedges under light irradiation is shown.

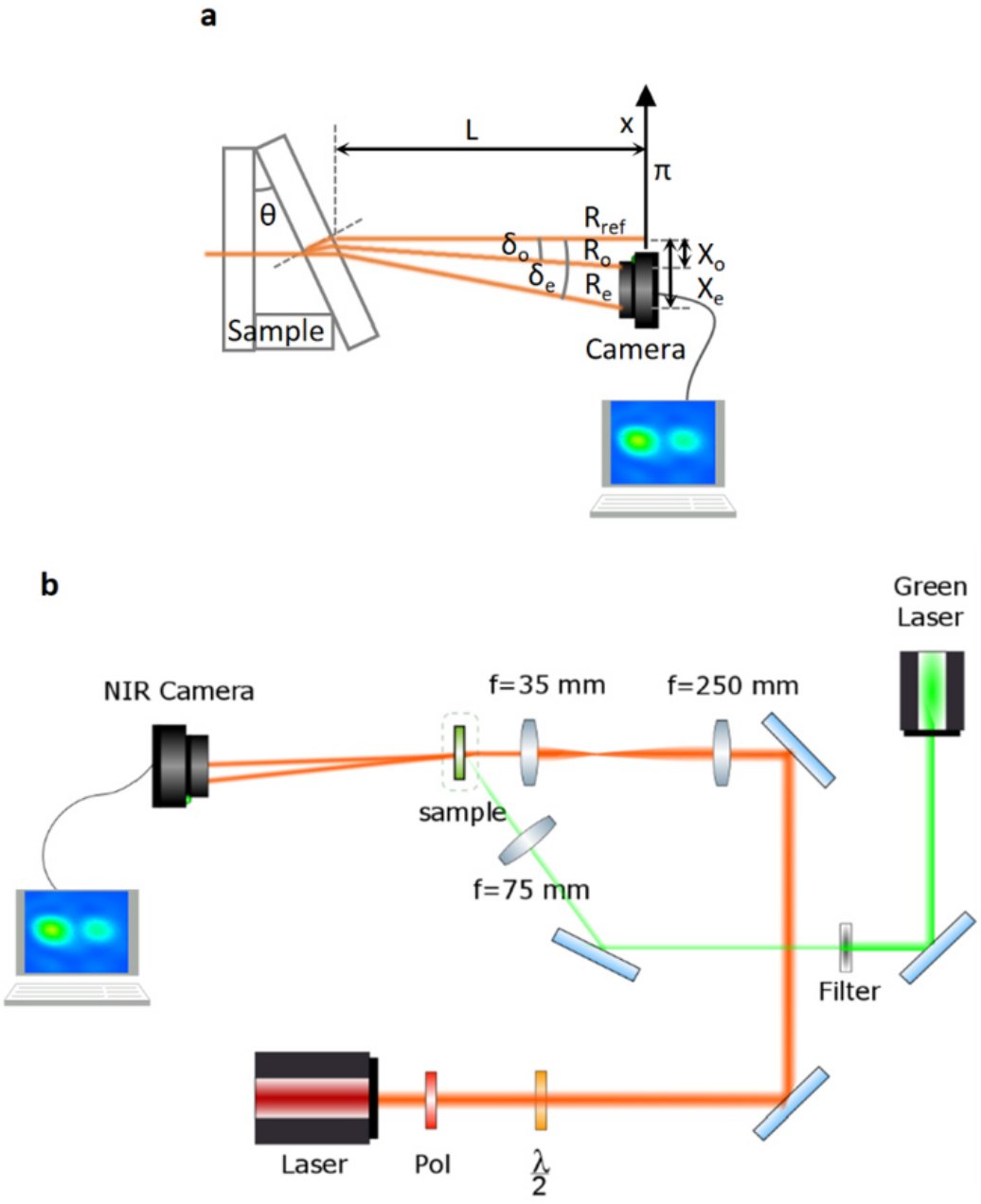

Figure 3.1. a) Geometrical ray representation of the laser beam through the LCN cell: θ is the wedge-cell angle formed by the two glasses, δ_o and δ_e are the deviation angles formed by the two beams R_o and R_e with respect to the beam R_{ref} emerging from the wedge in absence of the birefringent medium and θ is the angle of the wedge formed by the two glass plates. X_o is the camera displacement from the point O, X_e is the camera displacement from the point O and L which is the distance of the sample with respect to the camera. Exploiting all these parameters and geometrical considerations the refractive indices are retrieved. b) Experimental setup for controlling the refractive index of the microscopic wedges by light.

The laser source (supercontinuum laser Fianium in combination with an acousto-optic tunable filter (AOTF)) has been filtered to select a specific wavelength of 1550 nm. The characterization has been performed at a wavelength of 1550 nm because of the interest in photonic structures at telecom wavelength. The same method can be applied to other frequency range changing the laser source and detector accordingly [17, 19, 20]. A linear polarizer and a half-wave plate are used to control the beam polarization in order to obtain a linearly polarized light at 45° with respect to the director axis of the sample. The beam diameter of approximately 1 mm passes through the macro wedged cell composed of two glasses, and filled with the LCNs. For the microscopic samples, the collimated beam size has been reduced by two appropriate lenses in a 2f configuration, as reported in Figure 3.1.b. An imaging arm composed by a 10x objective (Mitutoyo Plan Apo NIR Infinity Corrected Objective) and its tube lens (focal length = 200 mm) enabled to verify the position of the beam in respect to the micro structure.

To control the birefringence of the LCN, two alternatively methods have been employed: temperature variation and green laser light irradiation (to match the azobenzene dye absorption). In the first case, the wedged cell is placed inside a Mettler Toledo SH82 hot stage, with the cell plate facing the laser source perpendicular to the infrared laser beam.

A light induced tuning of the refractive indices was obtained by focusing the green laser light on the microscopic wedge. Laser light is absorbed by the azobenze dye described in paragraph 1.3.9 and the absorbed energy is locally converted into heat triggering the LCN phase transition from the nematic to the para-nematic phase. Photo-response of the macroscopic sample was not possible as the wedge cell is thicker than the dye absorption length (around 6 μm).

A near-infrared camera (Phoenix Camera System INDIGO) is mounted upon a micrometric translating stage in order to change the detector position in a very precise way, across the observation plane π along the x axis (see Figure 3.1.a). First, the point where the ray, emerging from the empty wedge, encounters the observation plane π, perpendicular to laser beam direction, is determined experimentally. In presence of the filled cell with the birefringent elastomer, the collimated infrared beam passing through the sample splits itself in an ordinary ray and in an extraordinary ray. The camera is then translated in order to monitor the beam separation. The displacement X_o from the point O is recorded. Measuring the deviation angle of these rays with respect to the situation where the LCN cell is absent, we retrieve the two refractive indices of the Liquid Crystalline Networks by means of the refraction laws and geometrical considerations (see Figure 3.1.a) following the formulas:

$$n_o = \frac{\sin(\theta + \delta_0)}{sin\theta}$$

$$n_e = \frac{sin(\theta + \delta_e)}{sin\theta}$$

$$n_m = \frac{n_e + 2n_o}{3},$$

where θ is the angle of the wedge formed by the two glass plates, δ_o and δ_e are the angles formed by the two beams R_o and R_e with respect to the beam R_{ref} emerging from the wedge in absence of the LCN cell.
Therefore,

$$n_o = \frac{\sin\left(\theta + tan^{-1}\left(\frac{X_0}{L}\right)\right)}{sin\theta}$$

$$n_e = \frac{\sin\left(\theta + tan^{-1}\left(\frac{X_e}{L}\right)\right)}{sin\theta}.$$

3.3 Macro- and microscopic LCN samples

The employed molecules are depicted in Figure 3.2.a: monomer and cross-linker were purchased by Synthon Chemical, the initiator Irgacure 369™ was purchased from Sigma Aldrich and the azo dye was prepared as elsewhere described [5]. The different photoresist compositions, employed in this characterization, are reported in Table 3.1 and the mixtures were prepared by mixing the different molecules after dissolution in dichloromethane that is then removed by a vacuum pump.

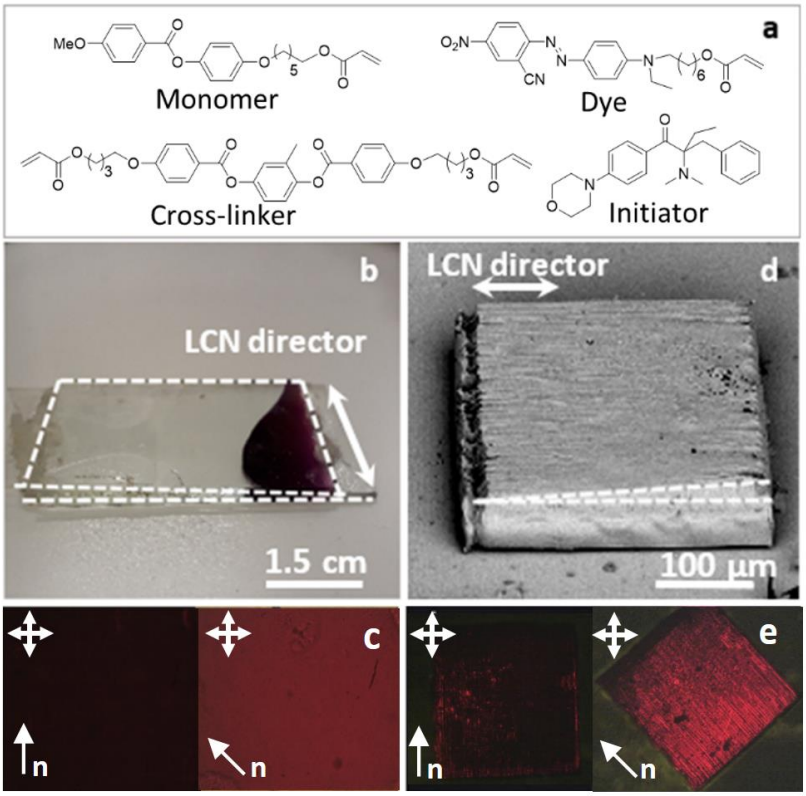

Figure 3.2. Material preparation. a) Chemical structures of the molecules employed for the LCN mixtures. Macroscopic wedge: b) optical image of the glass cell infiltrated with LCNs after UV polymerization and c) polarized optical microscope (POM) images. The LCN director is indicated by the versor **n**. Microscopic wedge: d) Scanning electron microscope (SEM) image of the wedge polymerized by Direct Laser Writing and e) its POM images. The LCN director is indicated by the versor **n**.

	Monomer	Cross-linker	Dye	Irgacure 369
Cross-linker(30%)	68	30	1	1
Cross-linker(40%)	58	40	1	1
Dye(1%)	68	30	1	1
Dye(2%)	67	30	2	1
Dye(5%)	64	30	5	1

Table 3.1. Composition of monomeric mixtures.

A reversible tuning of photonic structures' optical properties can be achieved by adding an azobenzene dye to obtain a light induced reconfiguration of the LC network. At the same time, the dye presence in the polymeric matrices influences the molecular interactions thus modifying the self-assembled alignment and the overall optical properties of the system [21]. Among the several parameters that can be controlled to tune the properties of the polymeric matrix (as polymerization intensity, chemical composition [11, 15], polymerization temperature [13]), we decide to focus on those ones that allow to preserve good optical and mechanical features required for 3D printing of photonic devices.

In this study, we evaluate both the effect of dye (from 1 to 5 % mol/mol) and cross-linker (30 or 40% mol/mol) amount in the determination of the optical properties of the material. The results shown below demonstrate as the simple mixing of different quantity of same monomers is a valuable route to fabricate polymers with specific optical properties, without further efforts on synthesis or optimization of processing protocols.

LCN wedges were prepared both in macroscopic (by polymerization with an UV lamp) and microscopic size (by two-photon polymerization using DLW).

Macroscopic samples are made by two glass substrates and an opportune spacer (at one end of the cell) to create the wedged cell shape (Figure 3.2.b) wherein the LCN mixture is infiltrated. The LCN molecules, homogenously aligned along a selected direction, are then polymerized by an UV lamp and their alignment has been verified by polarized optical microscope (POM images shown in Figure 3.2.c where the transmittance extinction is observed for sample rotation of 45°). More in detailed, the wedge-cell was assembled by two glass substrates separated by one spacer on one side and glued at both ends. Both glasses were coated by the polyimide PI 5291 (from Nissan Chemical group) and rubbed unidirectionally with a velvet cloth to achieve a planar homogenous alignment of the LC molecules. The

mixture is melted and infiltrated at 65 °C, then the cell was cooled down to reach the desired molecules alignment, that was verified by a polarizing optical microscope. For these macroscopic samples, polymerization of the mixture was done by an UV LED lamp power of 21 mW for 40 minutes at 40 °C and left at 80 °C for 20 minutes in order to terminate the polymerization process [22].

LCN micro-wedges (with a basis of 300 x 300 μm^2 and a height of about 20 µm) have been fabricated with different mixtures by the commercial Direct Laser Writing system. The micro-structure of Figure 3.2.d was polymerized with an average laser power of 30 mW and a writing speed of 90 µm/s at room temperature. The structure was subsequently developed for 50 minutes in isopropanol at 70 °C to remove the unpolymerized resist. Also in this case, the homogenous alignment quality has been verified through POM observation after polymerization, by checking the transmittance extinction with a sample rotation of 45°. Figure 3.2.d shows a SEM image of the microscopic wedge. Also in this case, the homogenous alignment has been confirmed by POM observation, as reported in Figures 3.2.e. In case of micro-structures, the choice of fabrication parameters is restricted to the conditions that allow to manufacture 3D homogeneous self-standing structures. For example, if a laser power close to the threshold value (which is the minimum laser power value needed to write structure, in our case 24 mW) is employed, the microstructure is non-homogeneous and presents many defects (Figure 3.3), limiting both the correct refractive indices values' determination and the applicability of such structures in photonics.

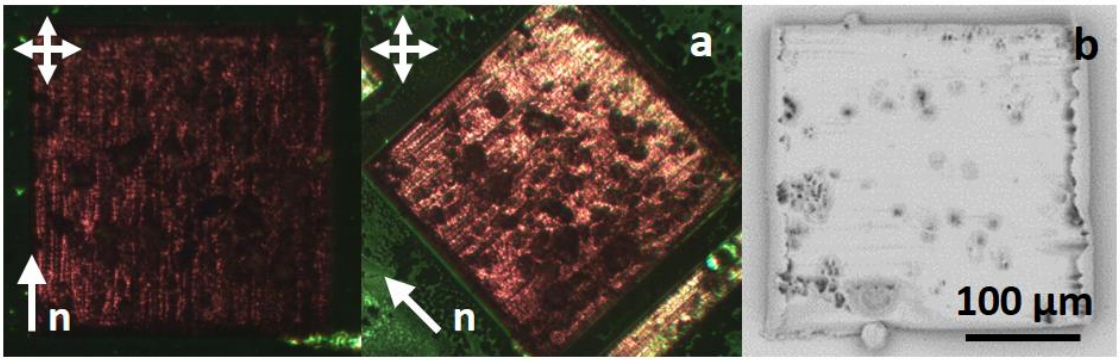

Figure 3.3. Microscopic wedge realized in correspondence of the power laser threshold value: a) polarized optical microscope (POM) images. The LCN director is indicated by the versor **n**. b) Scanning electron microscope (SEM) image of the wedge polymerized by Direct Laser Writing.

In Figure 3.3.a-b, a micro-wedge made of LCN mixture with dye(1%) has been polymerized by DLW with the power value of 24 mW (close to the polymerization threshold) and a writing speed of 90 µm/s at room temperature. In this case, the refractive indices at 30 °C are: $n_o = 1.46$, $n_e = 1.60$ and $n_m = 1.51$. Decreasing the polymerization power generates a less cross-linked network with a reduced refractive index value. For this sample, it was not possible to measure the refractive indices as a function of temperature: the extremely soft nature of the micro-wedge induced a structural deformation at about 40 °C with a strong reduction of the two light spots preventing the ray shift monitoring.

3.4 Optical characterization

3.4.1 Macroscopic wedge cell

The optical characterization has been performed by monitoring the lateral shift of the ordinary and extraordinary ray (Figure 3.4.a and Figure 3.5) that occurs by controlling the sample temperature. This is the evidence of temperature dependence of the order parameter that consequently determines the variation of refractive indices [19]. In Figure 3.4.b-c, the extraordinary, ordinary and average refractive indices of the macro-wedges are reported for samples realized with different mixtures. A higher amount of dopant leads to a more pronounced variation of the refractive indices (Figure 3.4.b) and a relevant reduction of the optical anisotropy (Figure 3.6.a) as function of the temperature.

Increasing the cross-linker mesogenic amount in the mixture (Figure 3.4.c), the refractive index values raise up while the optical anisotropy (Δn) as a function of temperature slightly decreases (Figure 3.6.b). Figure 3.6 reports the optical anisotropy as a function of the temperature for the macro-structures changing the amount of the dye (from 1 to 5% mol/mol) and the cross-linker (30 or 40% mol/mol).

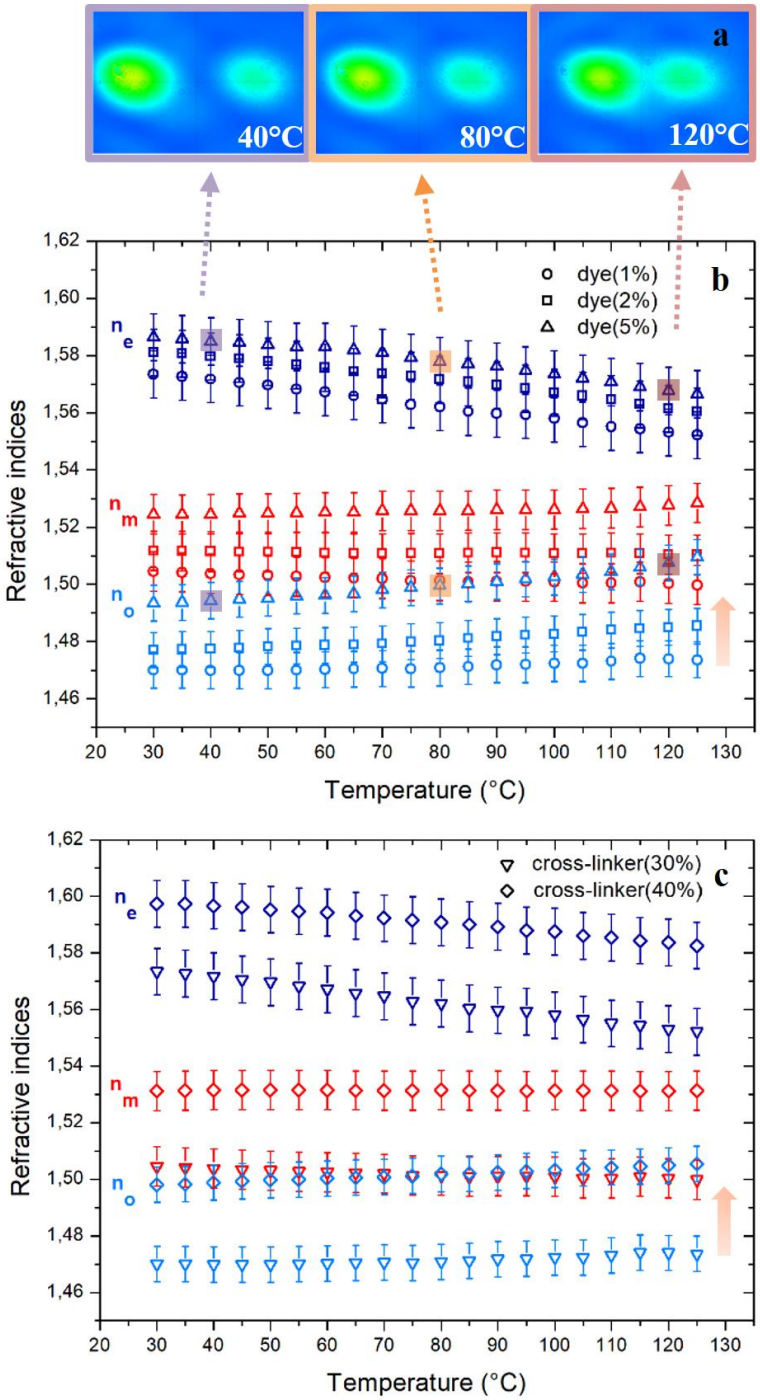

Figure 3.4. LCN macro-wedge optical characterization. a) Sequence of images recorded at different temperatures of the ordinary and extraordinary rays that result well split at room temperature, while they become closer and closer as the molecular disorder increases. b-c) Refractive index temperature dependence for different mixtures changing the amount of the dye (b) and the cross-linker (c). Increasing both the dye and the cross-linker amount in the mixture, the refractive index values increase.

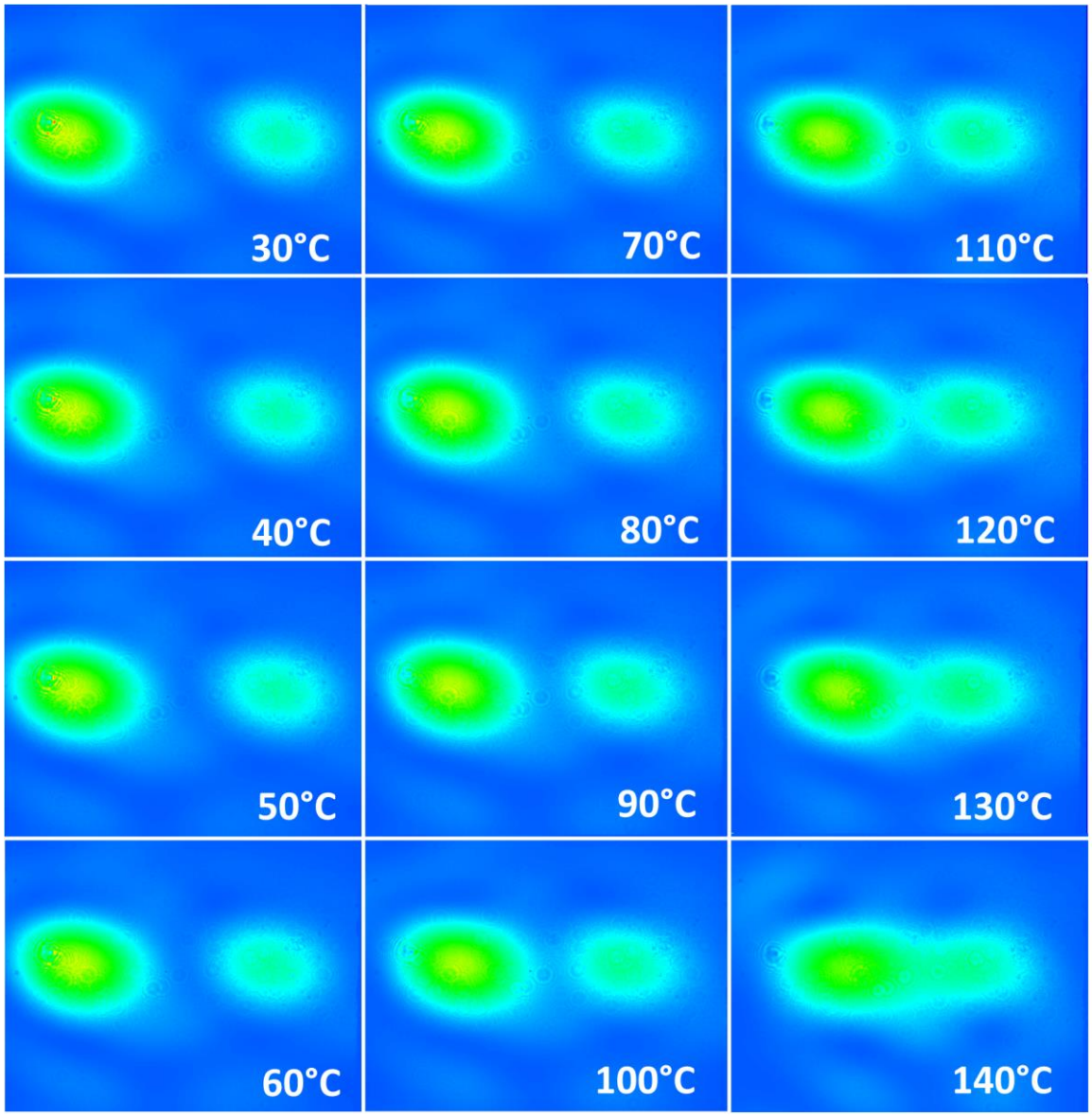

Figure 3.5. Ordinary and extraordinary beam spots on the NIR camera as function of the temperature in case of the macro-structure (dye 5%). To evaluate deviation angles of the ordinary and extraordinary rays varying the temperature, the centroid of the two beams at a fixed distance has been evaluated by a Matlab program (appropriately written) starting from these images.

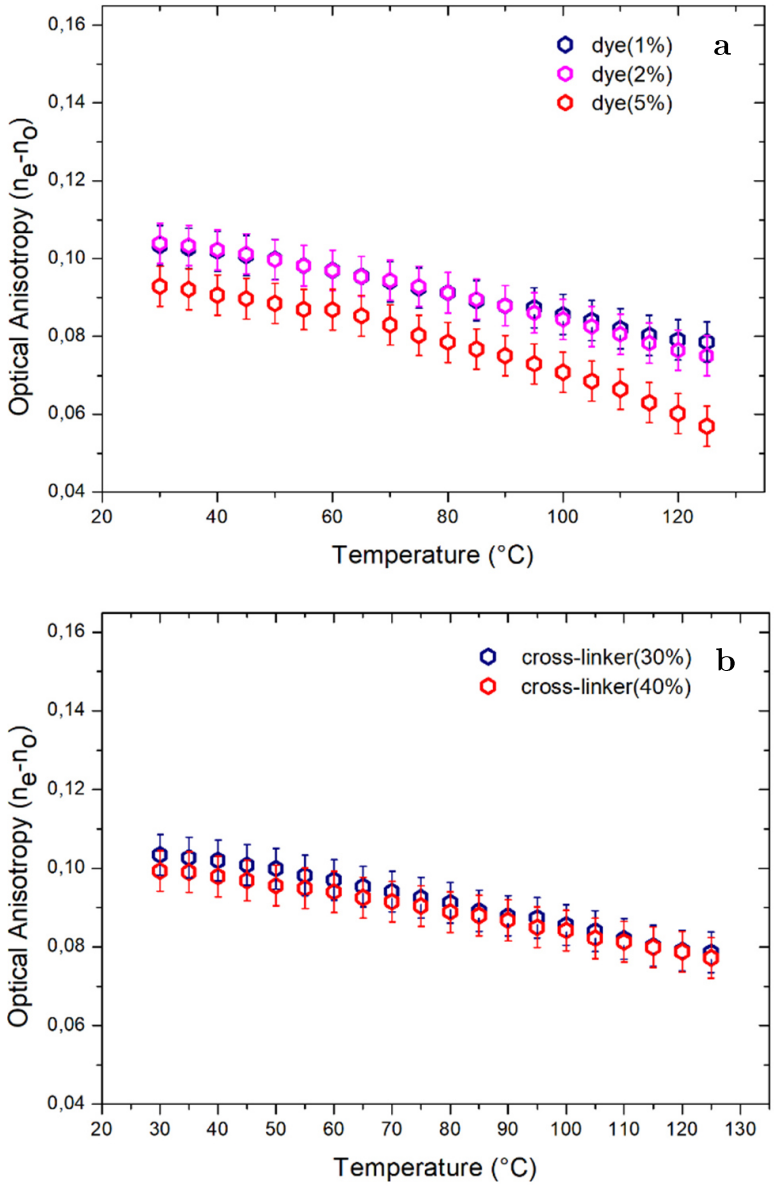

Figure 3.6. Optical anisotropy as a function of temperature with different amount of a) azo-dyes and b) cross-linker for macro samples.

These latter evidences should be respectively attributed to a density increase of the matrix and, at the same time, the reduced network mobility (for higher concentration of cross-linker) limits the refractive index variation with temperature. To evaluate the refractive index dispersion, n_o and n_e were also measured as a function of wavelength (from 1400 nm to 1600 nm) in case of dye(5%). In this case the supercontinuum laser light is filtered by using an acousto-optic tunable filter and the scan is controlled by a C++ software. The characterization shows as in this frequency range the wavelength dependence is

negligible (<1% in the selected range) (Figure 3.7). This feature is remarkable for applications where dispersion should be avoided while in other LCN formulations a strong dispersion has been obtained in the visible region towards optical compensation films [13].

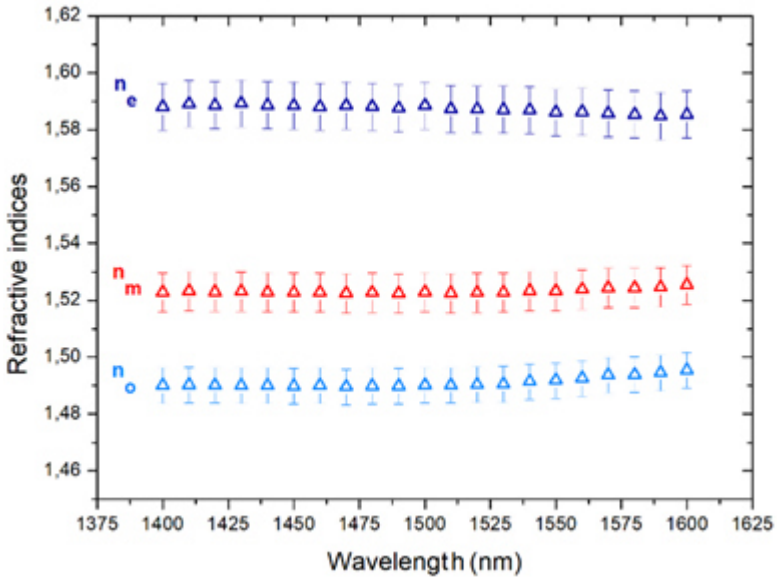

Figure 3.7. Measurement of the refractive indices as a function of wavelength (from 1400 nm to 1600 nm) for a micro wedge doped with 5% of dye.

The optical activation of the molecular disordering within the macroscopic wedge was not possible because of the thickness of the cell (few millimeters) compared to the dye absorption length (around 6 µm). By irradiating the sample with the proper wavelength, only a skin-deep modification of the sample was achieved and no variation of the beam splitting was thus observed.

3.4.2 Microscopic wedge cell

It is now interesting to compare the results obtained for the macroscopic sample with the refractive index of the micro-wedge cell. Figure 3.8.a reports the temperature dependence of the refractive indices for LCN micro-wedge made by two different mixtures changing the amount of the dye, 1% and 5% respectively.

Within 2-photon polymerized structures, the refractive index results increased with respect to 1-photon polymerized (standard UV polymerization) wedges for both mixtures. This refractive index variation can be attributed to a density increase as well as to an improved local molecular alignment along the writing

direction that results in a more birefringent medium. Indeed, both the ordinary and extraordinary refractive index result increased but the more relevant variation has been recorded along the molecular orientation axis for the micro patterned structures as evidence of an improved alignment at the microscale. Interestingly, higher refractive index values in LCN photonic microstructures do favour the electromagnetic field confinement in light guiding elements and improve the refractive index contrast in photonic crystals.

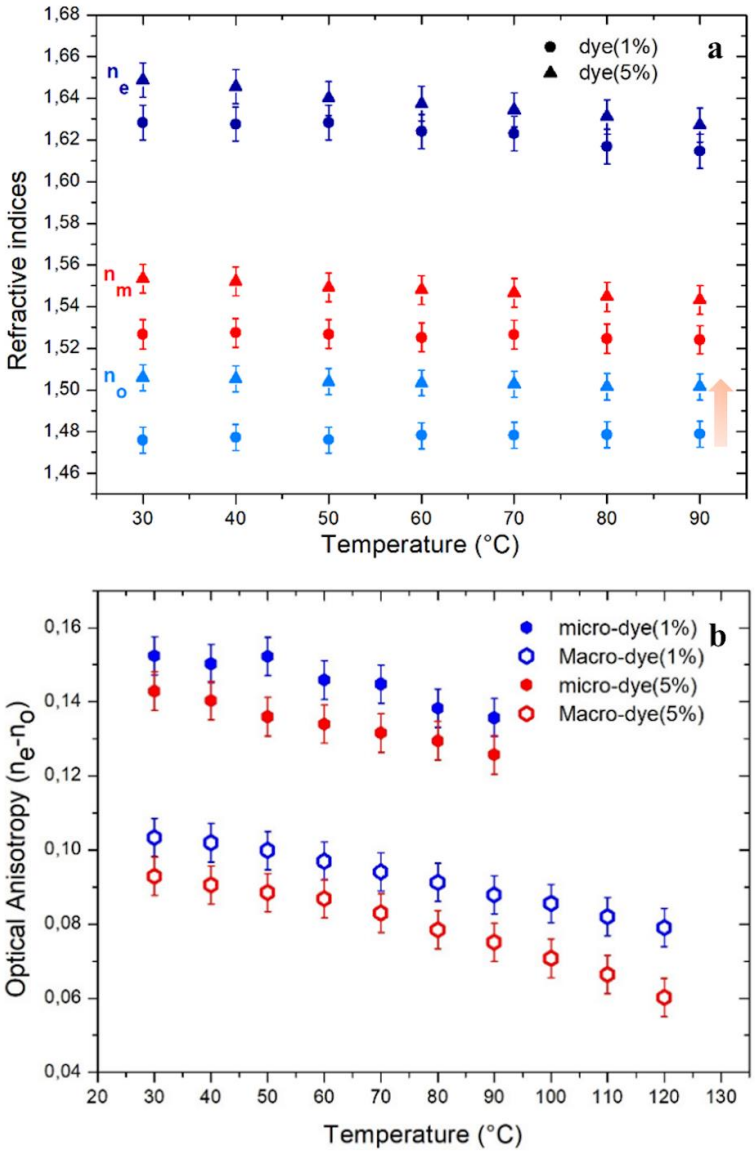

Figure 3.8. LCN micro-wedge optical characterization. a) Refractive index temperature dependence for LCN micro-wedge in case of two different mixtures changing the amount of the dye, 1% e 5% respectively. b) Optical anisotropy as a function of temperature for mixtures with different amount of azo-dye. Measurements for macro LCN cell and micro-wedge are compared.

To directly compare the data of mixtures with a different dye percentage in macroscopic and microscopic structures, the optical anisotropy as a function of temperature is reported in Figure 3.8.b. It should be noted the initial effective Δn for all the LCN samples is comparable with the values known in literature where birefringence values are between 0.05 and 0.25 depending on the molecular composition [12]. For microscopic structures, the refractive indices values are shown in a temperature range between 30 °C and 90 °C because above 90 °C the micro-wedge starts deforming, inducing a strong reduction in the intensity value of the laser spots. Indeed, a protracted exposition to high temperatures may prevent the recovering of the initial state probably due to a damage of the network. However, a further reduction of the optical anisotropy can be supposed at higher temperatures extrapolating the data trend and it is confirmed below using an activation optical stimulus. In case of macro-samples, the optical anisotropy has a comparable value but it is slightly reduced in the mixture with a dye percentage of 5%. Once the network undergoes the molecular disordering, the 5% dye-doped polymer exhibits a more pronounced temperature dependence of the optical anisotropy. While in case of micro-wedges, the optical anisotropy is considerably enhanced in both formulations and it is larger, as for the macro-structures, in the mixture with the lower concentration of azo-dye molecules. Due to the non-liquid crystalline nature of the azo-dye, it behaves as an impurity thus slightly diminishing the overall optical anisotropy.

The slow and non-local nature of the temperature variation stimulus (by using a hot-stage) prevented the complete characterization and exploitation of the whole range of tunability of the optical properties for micro-structured LCNs for practical applications. A laser light activation, was thus employed to tune the refractive indices of the micro wedges as the structure thickness is comparable with the laser light absorption length of the dye doped LC matrix. A light induced modification of the refractive indices has been attained by focalizing a green laser (532 nm) on the whole micro-structure surface and the results are shown in Figure 3.9.

The refractive index variation as a function of the irradiating laser power is reported for the LCN mixture with 5% of dye. It is interesting to notice that the local light activation of the molecular transition results in a more effective disordering of the liquid crystal alignment. This effect could be ascribed to both thermal (dissipation of light energy into heat) and optical effect (due to dye isomerization process). The latter was already demonstrated not able to induce a

shape-deformation in these formulations but inducing a photo-softening effect, it thus modifies the polymer structure at the molecular level [20]. The predominant effect in the change of birefringence is determined by the extraordinary refractive index variation and above 5 mW of laser power, the refractive index values remain constant (Figure 3.9.a) indicating that the maximum refractive index variation was achieved. The proof of such effect can be noticed also in Figure 3.9.b where the optical anisotropy value drops by half using an optical actuation.

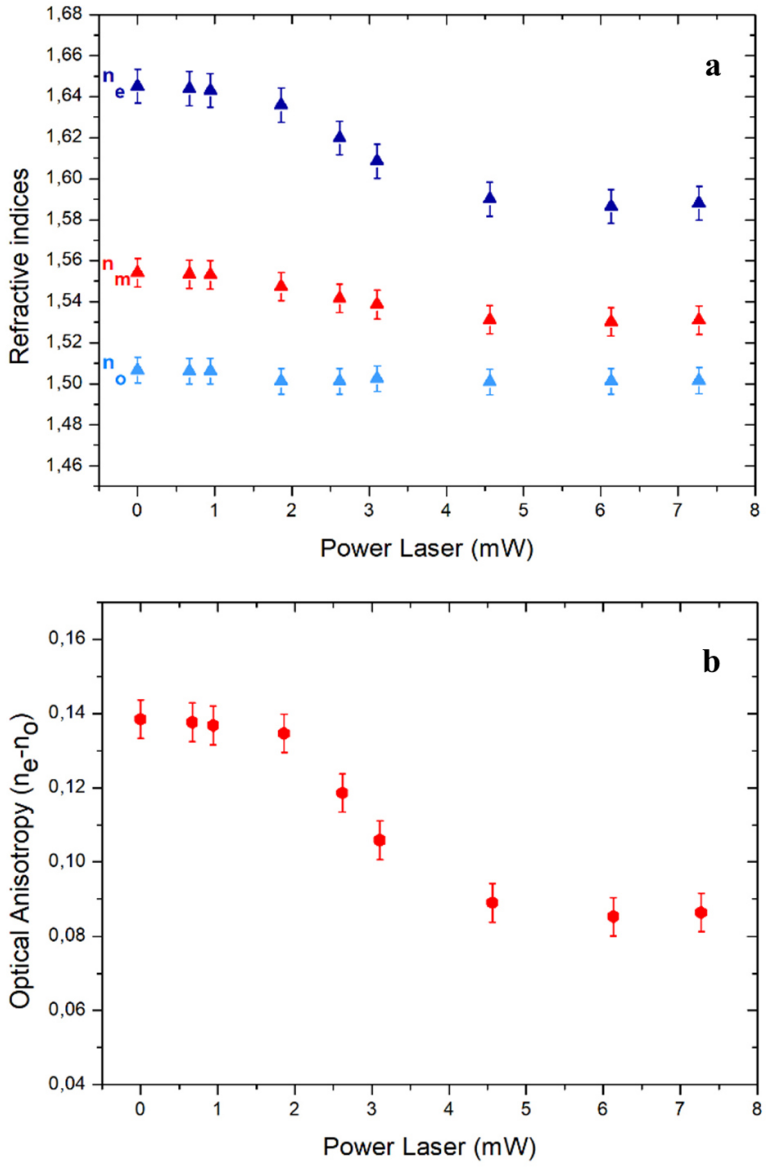

Figure 3.9. Light induced refractive index tuning of the microscopic wedge made by a 5% dye doped LCN matrix. a) Refractive indices and b) optical anisotropy are reported as a function of the laser power of the activating optical stimulus.

Such local measurements highlighted as the optical properties cannot be assumed similar in macro and micro structures as they significantly depends on the employed polymerization process. On the other side, the optical properties and their tunability under an external stimulus have been easily modulated by adjusting the cross-linker and dye concentration in the mixture. Moreover, the maximum variation of the optical anisotropy has been achieved in microstructures only by a remote laser light stimulus, making temperature less effective in the LCN disordering at this length scale.

References

[1] S. Nocentini, D. Martella, C. Parmeggiani, S. Zanotto, D.S. Wiersma, Adv. Opt. Mater. 2018, 6, 1800167.

[2] A. M. Flatae, M. Burresi, H. Zeng, S. Nocentini, S. Wiegele, C. Parmeggiani, H. Kalt, D.S. Wiersma, Light Sci. Appl. 2015, 4, e282.

[3] S. Maruo, O. Nakamaura, S. Kawata, Opt. Lett. 1997, 22, 132-134.

[4] C. N. LaFratta, J. T. Fourkas, T. Baldacchini, R. A. Farrer, Angew. Chem. 2007, 46, 6238-6258.

[5] H. Zeng, D. Martella, P. Wasylczyk, G. Cerretti, J. C. Lavocat, C. H. Ho, C. Parmeggiani, D. S. Wiersma, Adv. Mater. 2014, 26, 2319-2322.

[6] S. Nocentini, D. Martella, C. Parmeggiani, D. S. Wiersma, Materials 2016, 9, 525.

[7] S. T. Wu, U. Efron, L. D. Hess, Appl. Optics 1984, 23, 3911-3915.

[8] W. Kuczyński, B. Stryła, Mol. Cryst. Liq. Cryst. 1975, 31, 267-273.

[9] Y. Hu, B. T. Miles, D. Ho, M. P. C. Taverne, L. Chen, H. Gersen, J. G. Rarity, C. F. Faul, Adv. Opt. Mater. 2017, 5, 1600458.

[10] B. L. Lachut, S. A. Maier, H. A. Atwater, M. J. de Dood, A. Polman, R. Hagen, S. Kostromine, Adv. Mater. 2004, 16, 1746-1750.

[11] A. J. J. Kragt, I. P. M. van Gessel, A. P. H. J. Shenning, D. J. Broer, Adv. Opt. Mater. 2019, 1901103.

[12] D. Liu, D. J. Broer, Langmuir 2014, 30, 13499-13509.

[13] C.-S. Hsu, H.-L Chen, J. Polym. Sci. Pol. Chem. 1999, 37, 3929–3935.

[14] Y. Yusuf, Y. Sumisaki, S. Kai, Chem. Phys. Lett. 2003, 382, 198-202.

[15] K. Okano, O. Tsutsumi, A. Shishido, Y. Ikeda, J. Am. Chem. Soc. 2006, 128, 15368-15369.

[16] M. Warenghem, G. Joly, Mol. Cryst. Liq. Cryst. 1991, 207, 205-218.

[17] J. Li, S.-T. Wu, S. Brugioni, R. Meucci, S. Faetti, J. Appl. Phys. 2005, 97, 073501.

[18] S. Brugioni, R. Meucci, Infrared Phys. Technol. 2007, 49, 210–212.

[19] S. Brugioni, S. Faetti, R. Meucci, Liquid Crystals 2003, 30, 927-930.

[20] S. Brugioni, R. Meucci, S. Faetti, J. Optical Technol. 2006, 73, 315-317.

[21] D. Martella, S. Nocentini, F. Micheletti, D. S. Wiersma, C. Parmeggiani, Soft Matter 2019, 15, 1312-1318.

[22] D. Martella, D. Antonioli, S. Nocentini, D. S. Wiersma, G. Galli, M. Laus C. Parmeggiani, RSC Advances 2017, 7, 19940–19947.

Chapter 4

4 Temperature role in two-photon polymerization in birefringent materials

Shrinking down various applications to the microscale employing soft stimuli responsive requires polymeric materials patterned with high resolution. In Chapter 4, we point out how refined resolutions, never yet reached for Liquid Crystalline Networks, can be achieved by using a temperature controlled two photon polymerization process and opportune writing parameters. The resulting 3D polymerizable unit size, now comparable with the typical voxel of commercial resists, enlarges the application field of photo-responsive elastic materials for photonics without degradation of the patterned structure rigidity.

4.1 Stimuli responsive soft polymers: resolution increase at the microscale

First demonstrations of stimuli responsive photonic structures made by Liquid Crystalline Networks [1-17] have been recently reported [18-27]. Their structuration at the microscale has been achieved with direct laser writing. While these materials promise a new route for light tunable photonic structures, the first examples of Liquid Crystalline Networks patterned with DLW recently appeared for robotic [28-30] and photonic applications [19-21] but their further development and expansion is still limited by resolution and mechanical property control. Therefore, lithographic performances on soft polymers have to be pushed towards the results obtained for glassy commercial resists, still preserving their peculiar elasticity, in order to make them really competitive and appealing for nanometric featured devices.

The interest in shrinking down various applications to the microscale requires high resolution lithographic techniques as soft lithography and photolithography (described in Chapter 1) [12]. While they offer good resolution in 2D structures,

truly three dimensional designs in polymeric matrices can be obtained in a single step process only by a two-photon polymerization based lithography, the direct laser writing (see Chapter 1 for more details). Increasing the dimensionality of soft structures introduces a rigidity/softness balance quests. In three-dimensional photonic crystals, chiral photonic structures, as well as in opto-mechanics applications, the typical structure periodicity/dimension for visible and near infrared applications ranges from few hundreds of nanometers up to few microns requiring sub-diffraction limited resolution. Furthermore, moving towards tunable shape changing structures, whose geometry can be externally controlled by a light induced actuation, as local and wireless control, stable and reversible deformation should be pursued.

4.2 Strategies and studies to improve resolution

In two photon polymerization (TPP), to reduce the smallest polymerizable unit (namely the voxel, volume-pixel), different strategies have been proposed either exploiting the addiction of polymerization inhibitors to the photosensitive mixture [31] or translating the stimulated-emission depletion (STED) fluorescence microscopy principle into the lithographic analogue [32]. In the first case, an approximately resolution of 70 nm has been reported for commercial polymers [31], while with STED lithography 65 nm thick lines were obtained [32]. However, the STED implementation requires more complex optical setup with delicate laser beam alignment and specialized photo-initiators with both high two-photon cross-section and fluorescence quantum efficiency [32]. To improve the TPP performances, new photo-initiators have been tested [33, 34]. However, understanding and controlling the voxel formation enlarges the application field avoiding new synthesis and extending the employ of the mixture under study. In the last decade, a more rigorous approach to the photo-polymerization process has been also developed [35-37] including few experimental studies on the polymerization mechanism [38] and kinetics [39, 40] on commercial resists. On the other side, for arbitrary complex 3D shapes, it is of fundamental importance the self-standing nature of soft polymeric structures achievable by tuning their chemical-physical properties and the lithographic polymerization parameters. Properties as Young's modulus and the degree of polymer cross-linking were investigated respectively using nano-indentation [41] and coherent anti-Stokes Raman scattering microscopy [42-44]. These works provide a fundamental insight

into the laser writing mechanism for homogeneous glassy materials while the light induced polymerization in soft responsive materials remains still unexplored.

The patterning of LCNs with DLW showed that tuning the lithographic setting and varying the chemical composition of the mixture, a lateral resolution of 160 nm can be achieved, for mixtures with the higher content of the cross linking agent (40% mol/mol) [45]. Despite this first characterization, a comprehensive analysis on the polymerization phenomenon should be performed to understand and improve the existing limits and constraints about rigidity and dimension of the polymerizable unit.

4.2.1 Temperature role on resolution

Among the different parameters to tune the lithographic properties, special mention is deserved to temperature. Several phenomena (e.g. swelling, polymerization shrinkage, monomer diffusion), having a temperature dependence, contribute to determine the voxel dimensions. In particular, diffusion of the liquid monomers affects both structural resolution and rigidity and it is ruled by material properties as viscosity and external parameters as temperature [37]. Temperature is particularly effective for phase changing materials as liquid crystal based compounds that show a strong temperature dependent behavior. Interestingly, the light induced polymerization with high power femtosecond lasers does not induce a local heating of the exposed area that has been estimated to be smaller than 5 K for laser powers well above the polymerization threshold, confirming the photo-chemical nature of the process rather than a photo-thermal one [46]. An external temperature control over the process should be then achieved by a customized heating/cooling system. Kawata et al. carried out a temperature dependent polymerization characterization on commercial resins demonstrating as reducing temperature slightly lowers the voxel size, while increasing temperature leads to improved resolution (from 1.4 µm at 20 °C to 1 µm at 80 °C for 512 ms exposure time) [47]. Such behavior has been attributed to a reduction of the monomer diffusion at negative temperatures whereas, at higher temperatures, the accelerated termination of the polymerization reaction results in improved lateral resolution [47].

To generalize this approach, we here propose a temperature dependent analysis of photopolymerization on different materials, focusing the attention on anisotropic shape changing birefringent polymers (the LCNs) and compared them to a different

isotropic shape changing soft polymer: the hydrophilic polymeric network of PEG hydrogels and adopting as a reference a commercial glassy polymer (IP-Dip™). The molecules used for these experiments are reported in Chapter 1.

In our studies, in order to pattern hydrogel and IP-Dip™ structures with DLW system, the reversed z-axis configuration has been used: the structures were anchored to the central part of the glass and were realized from the top to the bottom. The hydrogel micro-structures were later developed in a bath of diethylether for 20 minutes at room temperature. The final IP-Dip™ structures have been developed in two solvent bath of a duration of 10 minutes at room temperature, the first in PGMEA (propylene glycol methyl ether acetate) and the latter in 2-propanol.

4.3 Materials characterization

In order to control resolution in bi-acrylate based micro devices avoiding the degradation of the mechanical properties, we exploited dependence on temperature of the chemical-physical property of stimuli responsive shape-changing materials (LCNs and hydrogels). In our study, the investigated temperature range was fixed among 5 °C - temperatures below 5 °C were not explored since air condensation on the substrate limits the writing performances - and room temperature, to maintain a stable LC nematic phase. In fact, the LCN mixture with a 30% of mol/mol cross-linker content shows a wide nematic phase window from 50 °C up to zero degree [47]. Writing structures in such interval freezes the desired alignment into the final polymerized device. We investigated homogenously (liquid crystalline molecules parallel to the glass substrate) or homeotropically (liquid crystalline molecules orthogonal to the glass substrate) aligned structures as the most widely exploited molecular ordering that originates contraction movement (in plane and orthogonally to the substrate, respectively). The characterization has been performed using the commercial platform for DLW (Nanoscribe GmbH) with a home-made Peltier stage (RS components) adapted to the sample holder with mechanical components (Figure 4.1). The temperature feedback controller allows to stabilize the writing temperature at a desired value (In Figure 1.5 of Chapter 1 the complete experimental set up is reported, while technical information about the commercial DLW system are presented in the Paragraph 1.2.3).

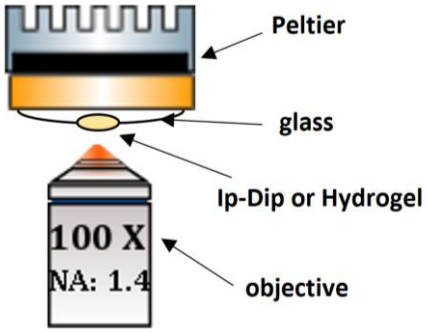

Figure 4.1. Home-made Peltier stage with cell position with respect to the objective.

The main features, considered in our study, because they give an insight on the molecular dynamics and the physical chemical process, are the polymerization threshold, the voxel dimensions (planar and vertical resolution) and the structure rigidity. Such quantities have been retrieved varying the lithographic writing speed and the laser power value.

4.3.1 Polymerization threshold

The polymerization threshold, given a certain writing velocity, is the lowest power value able to create a well-defined polymeric line at the glass-resist interface. 20 µm long lines have been realized at the glass-resist interface varying the polymerization temperature from 22 °C to 5 °C and the laser power value for each segment at a fixed writing speed (from 90 µm/s to 15 µm/s). A scanning electron microscope image of such calibration is reported in Figure 4.2.a for the elastomeric mixture at 5 °C and 22 °C. From this calibration, we observed for the IP-Dip™ resist and the hydrogel mixture only a small variation of the polymerization threshold: it remains almost constant around 6 mW within this temperature range (Figure 4.2.b). A relevant dependence has been found instead for liquid crystalline networks, whose polymerization threshold passes from around 7.5 mW at room temperature down to 3 mW at 5 °C (Figure 4.2.b). At a glance, polymerization threshold may be attributed mainly to the activation of the photo-initiator while it is inherently defined by the termination kinetics and molecular reactivity [37, 49]. The kinetic behavior is dominated by photo-initiator depletion and radical quenching [50, 51]. The model that describes the photo-polymerization process relies on a system of partial differential equations for the photo-initiator, the monomer, the radical and the general inhibiting molecules concentration [49]. Once

the initial concentration of each species, the incident laser flux and the different quantum yields are fixed, the parameters that affect the polymerization are the diffusions of each molecule type and the termination constants (due to radical-radical termination, radical trapping in the polymeric network and combination of radical with inhibiting molecules, as oxygen) [49]. For liquid crystalline networks formation, the temperature decrease favors polymerization at lower laser power that can be explained as a reduction of the diffusion coefficients, an enhanced molecule reactivity, or a more efficient termination kinetics. As these two last contributes decrease with temperature with the Arrhenius law [49], the dominant effect should be attributed to molecule diffusion that promotes the formation of a solid voxel. This effect is evident only within the LCN matrix probably because in this temperature window the diffusion coefficients vary more considerably getting closer to the glass temperature. Thus lowering the temperature, monomers and radicals have a reduced diffusion coefficient that promotes the termination into a polymeric chain forming a smaller voxel even for a reduced polymerization power.

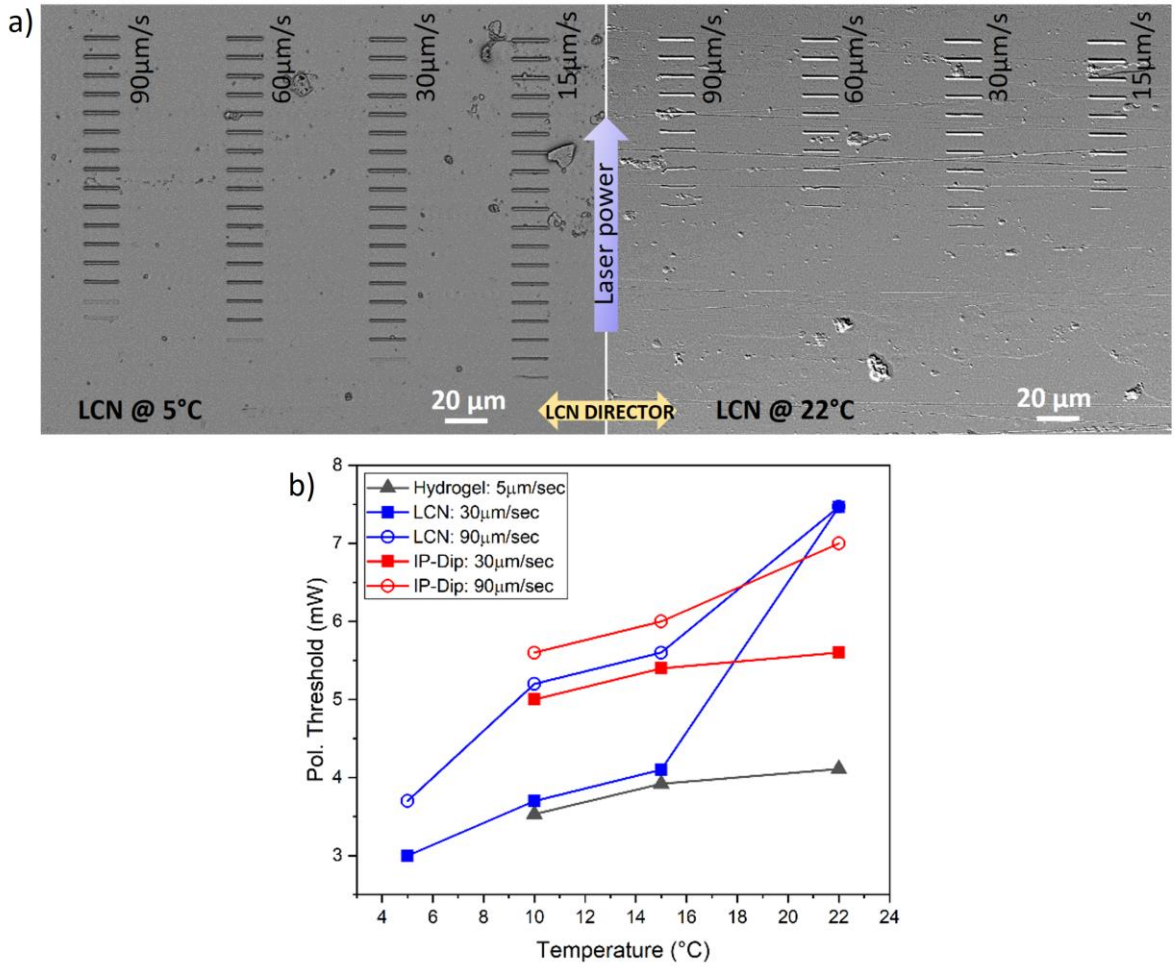

Figure 4.2. Polymerization Threshold. a) SEM image of a polymerization threshold characterization for the LCN mixture. The 20 µm segments have been written at the glass-resist interface varying the writing speed (from left to the right) and increasing the laser power (from the bottom to the top of the image). The shown characterization was done at 5 °C (on the left) and 22 °C (on the right). b) Polymerization thresholds for the different mixtures (Hydrogel, LCN and Ip-Dip™) as a function of temperature. Two different writing speed (90 µm/s and 30 µm/s) are reported for the LCN and IP-Dip™ resists.

4.3.2 Voxel dimension

To further exploit this peculiar trend, we investigated the voxel dimension variation as a function of temperature. Improving the 3D DLW resolution implies to minimize both the lateral resolution and the vertical one as well. In fact, a spheroidal voxel would be the best polymerization unit to fabricate three dimensional structures, especially in 3D photonic structures as woodpile photonic crystals or chiral photonic crystals for which isotropic voxel dimensions are needed.

Due to the non-linear photo absorption in the focal volume of the laser beam, the polymerized unit has an ellipsoidal shape whose aspect ratio (ratio of the major and minor axis of the ellipsoidal voxel) should then be minimized. For commercial resists, an aspect ratio of 2.7 have been achieved [52]. Our study is firstly focused on the lateral resolution of the different mixtures at different temperatures. For the characterization of the liquid crystalline mixture, homogenously and homeotropic aligned cells have been employed. The resolution has been evaluated from suspended lines fabricated on squared grids of 20 µm in size varying the writing velocity and the laser power as shown in Figure 4.3.a in case of IP-Dip™ structures.

From the analysis of the SEM images, both the minor and the major axis have been measured and reported as a function of the writing power at different temperatures (10 °C and 22 °C). The lateral resolution does not show a significant dependence on temperature for the IP-Dip™ resist reaching, at the polymerization threshold, a voxel's minor axis of 130 nm (writing speed 90 µm/s). For the hydrogel mixture, instead, the decrease in temperature creates an opposite effect making thicker the written lines. While for LCN compounds, controlling both the polymerization energy and temperature, the lateral resolution of the suspended lines can be improved below 100 nm decreasing the temperature of the monomeric mixture down to 10 °C (Figure 4.3.b).

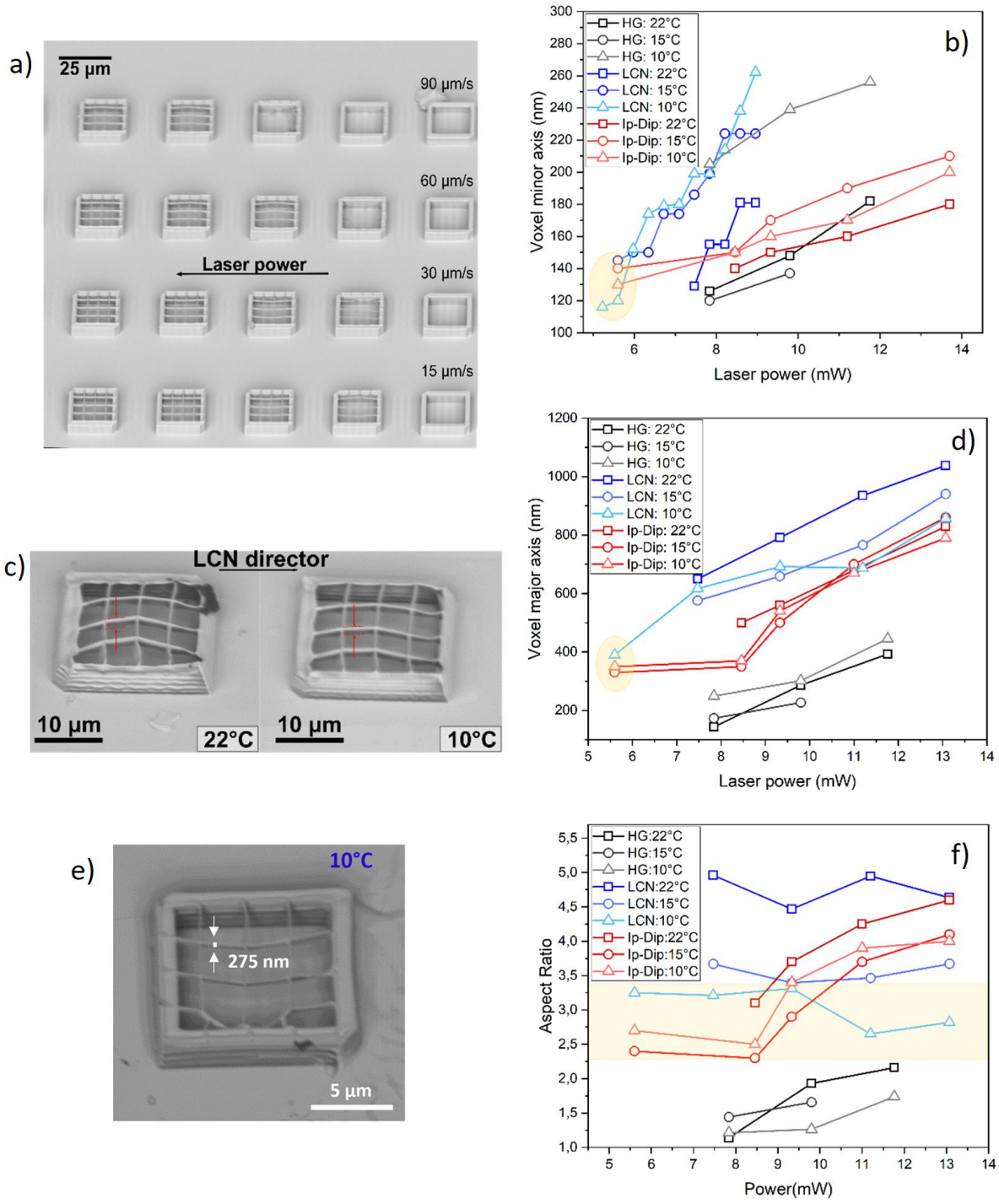

Figure 4.3. a) SEM image of a series of suspended grids to evaluate the line minor and major axis. The reported characterization have been realized for the IP-Dip™ resist at room temperature. The writing parameters are varied: laser power increased form right to left and the laser scanning speed from the bottom to the top. b) Evaluated minor axis as a function of power for the three resists at different writing temperatures. In the yellowish circle the best resolution performances of LCN are comparable with the commercial resist. c) SEM image that shows the major axis reduction at lower temperature (10 °C) for the LCN

mixture. d) Evaluated major axis as a function of power for the three resists at different writing temperatures. In the yellowish circle the best resolution performances of LCN are comparable with the commercial resist. e) SEM image of the major axis of the voxel at 10 °C. f) Evaluated aspect ratio (ratio between the major and the minor voxel axis) as a function of power for the three resists at different writing temperatures. In the yellowish rectangle, the best resolution performances of LCN are comparable with the commercial resist.

This improved performance at lower temperature is even straightened for the major axis ending up in a more spheroidal voxel (Figure 4.3.c.d). At room temperature the best writing parameters create a voxel height of around 700 nm whereas at 10 °C, it decreases up to 390 nm (Figure 4.3.d). In fact, at 10 °C the best writing parameters (90 µm/s and 5.5 mW) create a voxel height of around 390 nm. The value was estimated by measuring major axis of suspended lines reported in the SEM image of Figure 4.3.e. Lowering the temperature brings to a reduction of the aspect ratio from 5 to 3 independently on the employed power as shown in Figure 4.3.f that becomes comparable with the values obtained for commercial resists. The best resolution and aspect ratio is achieved for the hydrogel mixture whose aspect ratio at 10 °C describe an almost spherical voxel. This achievement highly enlarges the application of LCNs and hydrogels to any kind of three dimensional structures being both the resolution and the geometrical feature pushed toward the performances of well-known commercial polymers.

4.3.3 Swelling

With a further look at Figure 4.3.c, another effect can be noticed: decreasing the temperature, the suspended lines result more parallel, thus better reproducing the intended structure design. We hence decided to undergo a systematic analysis of this effect, that can be better appreciated in Figure 4.4.a, in LCNs. The segment's bending of soft materials in the photo-polymerization process is due to the swelling of the unpolymerized monomers inside the polymerized network. This liquid migration into the solid elements leads to a line warping that is definitely undesired within a lithographic process. The idea here is that, by reducing the temperature of the liquid mixture, the diffusion of monomers inside the polymerized volume is reduced accordingly. This effect has been evaluated through a quantitative estimation of the line warping. Line warping is defined as the deviation from linearity, as shown in Figure 4.4.a and quantitatively estimated in Figure 4.4.b. It

has been quantified measuring the lateral displacement of the first written line of the grid. This choice is motivated by the fact that the first written segment of the grid has more time to deform compared to the other lines (about 10 seconds). Only the warping of horizontal lines has been considered, as vertical lines have been written later: hence, they were forced not to warp by the existing constraint (the intersection with the horizontal lines).

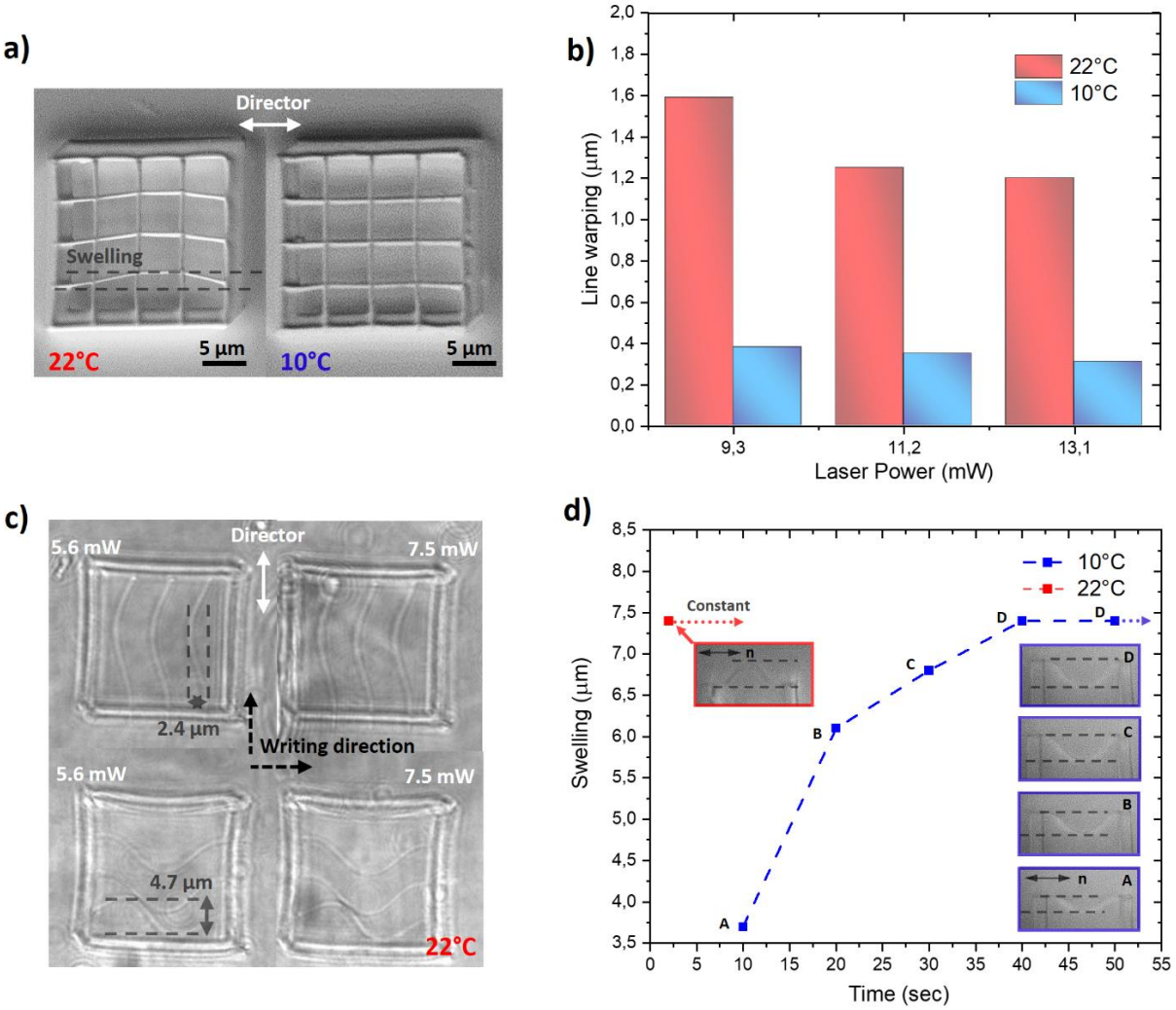

Figure 4.4. Swelling in LCN structures. a) SEM images of the grids realized in LCN mixture at 22 °C and 10 °C showing the line warping effect. b) Line warping as a function of laser power for the first line written parallel to the director in homogenously aligned grids at 22 °C and 10 °C, respectively. c) Suspended lines parallel to the director direction showing a lower line warping than perpendicular ones. d) Time evolution of the line warping of suspended lines written at 22 °C and 10 °C. Images in (a) are obtained with scanning electron microscopy of the developed sample, while images in (c) and (d) are collected through the objective of the direct laser writing apparatus from the LCN cell before development.

The deformation is larger along the direction perpendicular to the director, as demonstrated in Figure 4.4.c which shows suspended lines, parallel and perpendicular to the director direction, written at room temperature with a writing speed of 90 µm/s and varying the laser power. This phenomenon can be explained considering that the Young's modulus is higher along the director direction than the perpendicular one ($E_{\perp} < E_{//}$) [53]. In case of the employed LCN mixture, Young's modulus of the polymerized structure also increases of an order of magnitude from 22 °C to 5 °C justifying the rigidity increase with the temperature decrease [48] and also prevailing over the anisotropic properties of the diffusion coefficients ($D_{\perp} < D_{//}$), which also decrease with temperature. Finally, Figure 4.4.d shows the time evolution of line warping of suspended lines during the writing process. A comparable line warping is reached at 22 °C in 2 sec whereas at 10 °C, 40 sec should pass before having the same line deformation.

In literature, the reduction of line warping is attributed to the increase of laser power that favors a more efficient crosslinking degree. However, the laser power to increase the degree of polymerization and cross-linking results detrimental in terms of resolution [44]. Here we demonstrated how to reduce swelling simply by lowering the temperature thanks to a reduced monomer diffusion. In such a way, a more efficient polymerization process is achieved that improve both the resolution and the structures' rigidity.

4.3.4 Anisotropic resolution in LCN mixture

A careful analysis of the voxel dimensions unearthed another interesting unexpected behavior. In a LCN aligned cell, the voxel dimensions depend on the writing direction respect to the LCN director, while the other isotropic resists do not express such dependence because of their isotropic molecular matrices. A scheme of the LCN grids is reported in Figure 4.5.a to clarify the obtained results. We investigated such phenomenon using both a homogeneous and homeotropic alignment.

In the first case, Figure 4.5.b shows as, if the writing direction is parallel to the molecular alignment, the polymerized lines are characterized by a larger major axis and a shorter minor axis. The minor axis of orthogonally realized lines, in homogeneous and homeotropic LC cells, are retrieved and plotted in Figure 4.5.c at room temperature. To verify the influence of the molecular anisotropy also on the voxel major axis, we reported their values in Figure 4.5.d. In homeotropic cells

(purple dashed lines), with the director orthogonal to the glass substrate, both the minor and the major axis of the two differently oriented lines remains equal within the estimated error (30 nm), as expected. The laser writing direction does not influence the dimension of the voxel itself. Such observations underline that the voxel dimensions are affected by the liquid crystalline molecule orientation. As the director lays in the x-y plane, the in-plane molecular anisotropy determines the polymerized voxel dimensions while in the homeotropic case, no differences are present.

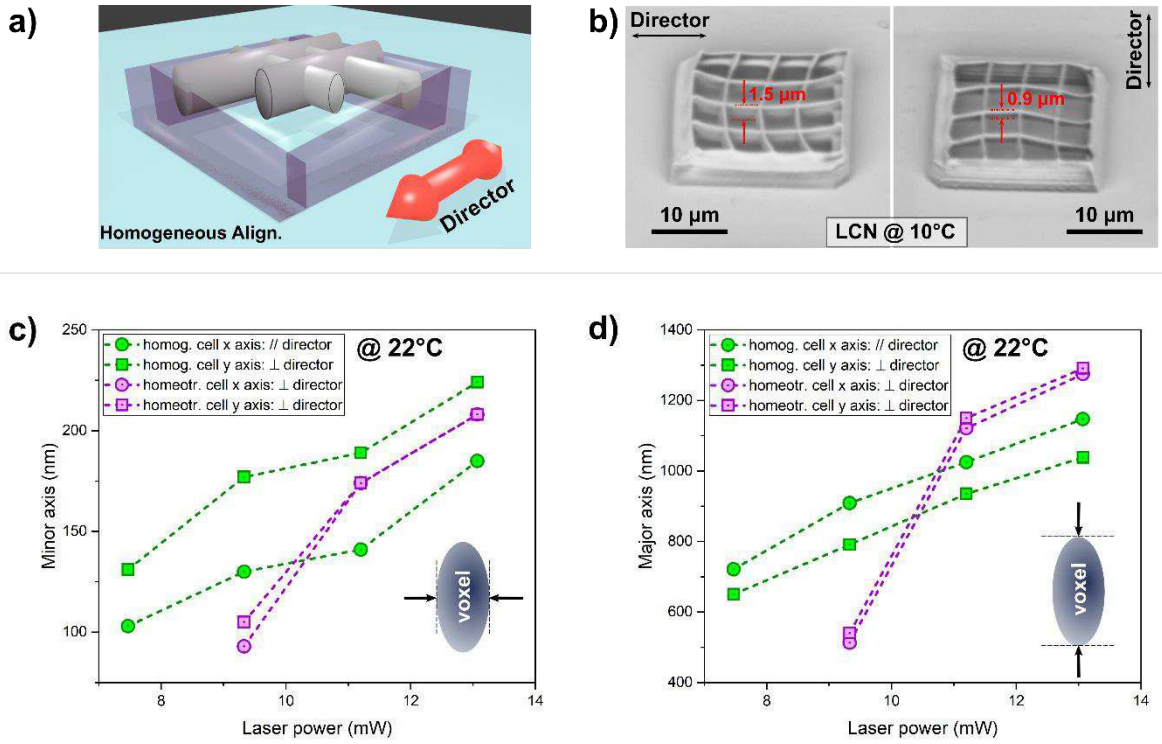

Figure 4.5. Anisotropic resolution in LCN mixture. a) Scheme of the anisotropic line resolution in a homogenously aligned LC cell. b) SEM pictures of the grid realized in LCN mixture at 10 °C, whose lines have been written parallel and orthogonally to the director direction. c) Minor axis size as function of writing power for a homogenously and homeotropically aligned cell. d) Major axis size as function of writing power for a homogenously and homeotropically aligned cell.

Several phenomena (e.g. swelling, polymerization shrinkage, monomer diffusion) contribute to determine the voxel dimensions and it is not trivial to distinguish between them. In literature is reported that lines, written by DLW along the rubbing are thicker, without any visible curl along the rubbing direction [54]. Also the polymerization shrinkage, which is the volume contraction due to the polymerization, depends on the molecular orientations and temperature [55, 56].

However, as previously discussed, we believe the main influence is due to the anisotropy of monomer diffusion. In fact, in the homogeneous alignment, the different segment thickness, obtained parallelly and perpendicularly to the director, can be explained by the anisotropy of the self-diffusion coefficients in liquid crystalline mixtures [57, 58]. In nematic liquid crystals, the diffusion coefficient $D_{//}$ parallel to the liquid crystal director is larger than the orthogonal component $D_{\perp}$ [58]. A higher rate of molecule diffusion along the LC orientation, together with the high anisotropy of the molecule dimensions combined with all the other parameters, affect the voxel dimension that, therefore, is thinner and taller in the writing direction parallel to the director.

References

[1] R.K. Iha, K.L. Wooley, A.M. Nystrom, D.J. Burke, M.J. Kade and C.J. Hawker, Chem. Rev. 2009, 109(11), 5620-5686.

[2] E. Smela, 2003, 15(6), 481-494.

[3] C. F. Carlborg, T. Haraldsson, K. Öberg, M. Malkoch, and W. van der Wijngaart, Lab on Chip 2011, 11(18), 3136-3147.

[4] A.C. Edrington, A.M. Urbas, P. DeRege, C.X. Chen, T.M. Swager, N. Hadjichristidis, M. Xenidou, L.J. Fetters, J.D, Joannopoulos, Y. Fink, and E.L. Thomas, Adv. Mater. 2001, 13(6), 421-425.

[5] L. Hines, K. Petersen, G.Z. Lum, and M. Sitti, Adv. Mater. 2017, 29(13), 1603483.

[6] J.F. Lutz, J. Polym. Sci. A Polym. Chem. 2008, 46(11), 3459-3470.

[7] D. Martella, P. Paoli, J.M. Pioner, L. Sacconi, R. Coppini, L. Santini, M. Lulli, E. Cerbai, D.S. Wiersma, C. Poggesi, and C. Ferrantini, Small 2017, 13(46), 1702677.

[8] D.W. Smith Jr, S. Chen, S.M. Kumar, J. Ballato, C. Topping, H.V. Shah and S.H. Foulger, Adv. Mater. 2002, 14(21), 1585-1589.

[9] M.A.C. Stuart, W.T. Huck, J. Genzer, M. Müller, C. Ober, M. Stamm, G.B. Sukhorukov, I. Szleifer, V.V. Tsukruk, M. Urban, and F. Winnik, Nat. Mater. 2010, 9(2), 101.

[10] J. Küpfer, and H. Finkelmann, Rapid Comm. 1991, 12(12), 717-726.

[11] M.-H. Li, and P. Keller, Philos. Trans. Royal Soc. A. 2006, 364(1847), 2763-2777.

[12] A. Buguin, M.-H. Li, P. Silberzan, B. Ladoux, and P. Keller, J. Am. Chem. Soc. 2006, 128(4), 1088-1089.

[13] K.D. Harris, C.W. Bastiaansen, J. Lub, and D.J. Broer, Nano Lett. 2005, 5(9), 1857-1860.

[14] M.-H. Li, P. Keller, B. Li, X. Wang, and M. Brunet, Adv. Mater. 2003, 15(7-8), 569-572.

[15] T. Ikeda, J.I. Mamiya, and Y. Yu, Angewandte Chemie International Edition 2007, 46(4), 506-528.

[16] T.J. White, and D.J. Broer, Nat. Mater. 2015, 14(11), 1087.

[17] S. Nocentini, C. Parmeggiani, D. Martella, and D.S. Wiersma, Adv. Opt. Mater. 2018, 1800207.

[18] G. Wu, Y. Jiang, D. Xu, H. Tang, X. Liang, and G. Li, Langmuir 2010, 27(4), 1505-1509.

[19] A. M. Flatae, M. Burresi, H. Zeng, S. Nocentini, S. Wiegele, C. Parmeggiani, H. Kalt, and D. S. Wiersma, Light Sci. Appl. 2015, 4(4), e282.

[20] S. Nocentini, D. Martella, C. Parmeggiani, S. Zanotto, and D. S. Wiersma, Adv. Opt. Mater. 2018, 1800167.

[21] S. Nocentini, F. Riboli, M. Burresi, D. Martella, C. Parmeggiani, and D.S. Wiersma, D. S. Three dimensional photonic circuits in rigid and soft polymers tunable by light. ACS Photonics 2018, 5(8), 3222-3230.

[22] S. Cosson, M. P. Lutolf, Sci. Rep. 2014, 4, 4462.

[23] L. D'eramo, B. Chollet, M. Leman, E. Martwong, M. Li, H. Geisler, J. Dupire, M. Kerdraon, C. Vergne, F. Monti, Y. Tran, Microsyst. Nanoeng. 2018, 4, 17069.

[24] A. Nishiguchi, A. Mourran, H. Zhang, M. Möller, Adv. Sci. 2018, 5(1), 1700038.

[25] R. A. Barry III, R. F. Shepherd, J. N. Hanson, R. G. Nuzzo, P. Wiltzius, J. A. Lewis, Adv. Mater. 2009, 21(23), 2407-2410.

[26] L. Brigo, A. Urciuolo, S. Giulitti, G. Della Giustina, M. Tromayer, R. Liska, N. Elvassore, and G. Brusatin, Acta Biomat. 2017, 55, 373-384.

[27] E. Käpylä, T. Sedlačík, D. B. Aydogan, J. Viitanen, F. Rypáček, and M. Kellomäki, Mater. Sci. Eng. C 2014, 43, 280-289.

[28] S. Palagi, A. G. Mark, S. Y. Reigh, K. Melde, T. Qiu, H. Zeng, C. Parmeggiani, D. Martella, A. Sanchez-Castillo, N. Kapernaum, F. Giesselmann, D. S. Wiersma, E. Lauga, and P. Fischer, Nat. Mater. 2016, 15, 647.

[29] H. Zeng, P. Wasylczyk, C. Parmeggiani, D. Martella, M. Burresi, and D. S. Wiersma, Adv. Mater. 2015, 27(26), 3883-3887.

[30] D. Martella, S. Nocentini, D. Nuzhdin, C. Parmeggiani, and D. S. Wiersma, Adv. Mater. 2017, 29, 1704047.

[31] I. Sakellari, E. Kabouraki, D. Gray, V. Purlys, C. Fotakis, A. Pikulin, N. Bityurin, M. Vamvakaki, and M. Farsari, Acs Nano 2012, 6(3), 2302-2311.

[32] J. Fischer, G. von Freymann, and M. Wegener, Adv. Mater. 2010, 22(32), 3578-3582.

[33] K. S. Lee, D. Y. Yang, S. H. Park, and R. H. Kim, Polym. Adv. Technol 2006, 17(2), 72-82.

[34] S. M. Kuebler, M. Rumi, T. Watanabe, K. Braun, B. H. Cumpston, A. A. Heikal, L. L. Erskine, S. Thayumanavan, S. Barlow, S. R. Marder, and J. W. Perry. J. Photopolym. Sci. Tec. 2001, 14(4), 657-668.

[35] K. Sugioka, and Y. Cheng, Appl. Phys. Rev. 2014, 1(4), 041303.

[36] C. N. LaFratta, and T. Baldacchini, Micromachines 2017, 8(4), 101.

[37] A. Pikulin, and N. Bityurin, Phys. Rev. B 2007, 75(19), 195430.

[38] J. Fischer, J. B. Mueller, J. Kaschke, T. J. Wolf, Opt. Express 2013, 21(22), 26244-26260.

[39] J. B. Mueller, J. Fischer, F. Mayer, M. Kadic, and M. Wegener, Adv. Mater. 2014, 26(38), 6566-6571.

[40] E. Stankevičius, E. Daugnoraitė, A. Selskis, S. Juodkazis, and G. Račiukaitis, Opt. Express 2017, 25(5), 4819-4830.

[41] K. Cicha, T. Koch, J. Torgersen, Z. Li, R. Liska, and J. Stampfl, J. Appl. Phys. 2012, 112(9), 094906.

[42] L. J. Jiang, Y. S. Zhou, W. Xiong, Y. Gao, X. Huang, L. Jiang, T. Baldacchini, J. F. Silvain, and Y. F. Lu, Opt. Lett. 2014, 39(10), 3034-3037.

[43] T. Baldacchini, and R. Zadoyan, Opt. Express 2010, 18(18), 19219-19231.

[44] A. Žukauskas, I. Matulaitienė, D. Paipulas, G. Niaura, M Malinauskas, and R. Gadonas, Laser Photonics Rev. 2015, 9(6), 706-712.

[45] S. Nocentini, D. Martella, C. Parmeggiani, and D. S. Wiersma, Materials 2016, 9(7), 525.

[46] J. B. Mueller, J. Fischer, Y. J. Mange, T. Nann, and M. Wegener, Appl. Phys. Lett. 2013, 103(12), 123107.

[47] K. Takada, K. Kaneko, Y. D. Li, S. Kawata, Q. D. Chen and H. B. Sun, Appl. Phys. Lett. 2008, 92(4), 041902.

[48] D. Martella, D. Antonioli, S. Nocentini, D. S. Wiersma, G. Galli, M. Laus, M. and C. Parmeggiani, RSC Adv. 2017, 7(32), 19940-19947.

[49] N. Uppal, and P. S. Shiakolas, J. Micro Nanolithogr. MEMS MOEMS. 2008, 7(4), 043002.

[50] C. Decker, and K. Moussa, 1989, 22(12), 4455-4462.

[51] S. C. Ligon, B. Husár, H. Wutzel, R. Holman, and R. Liska, Chem. Rev. 2013, 114(1), 557-589.

[52] I. Staude, M. Thiel, S. Essig, C. Wolff, K. Busch, G. Von Freymann, Opt. Lett. 2010, 35(7), 1094-1096.

[53] R. A. M. Hikmet, and D. J. Broer, Polymer, 1991, 32, 1627.

[54] H. Zeng, D. Martella, P. Wasylczyk, G. Cerretti, J-C. G. Lavocat, C.-H. Ho, C. Parmeggiani and D. S. Wiersma, Adv. Mater. 2014, 26, 2319-2322.

[55] R. A. M. Hikmet, B. H. Zwerver, and D. J. Broer, Polymer, 1992, 33(1).

[56] E. Anglaret, M. Brunet, B. Desbat, P. Keller, and T. Buffeteau, Macromolecules, 2005, 38, 4799-4810.

[57] S. Hess, D. Frenkel, M. P. Allen, Mol. Phys. 1991, 74(4), 765-774.

[58] G. J. Kruger, Phys. Rep., 1982, 82.4, 229-269.

Chapter 5

5 Tunable elastomeric photonic crystals

In Chapter 5 we demonstrate how taking advantage of the measured refractive index values of liquid crystalline network and using a temperature controlled photopolymerization, well-engineered 3D photonic crystals can be designed and fabricated in smart polymers. In particular, DLW lithographic technique enabled the fabrication of 3D woodpile photonic crystals in rigid and light responsive soft polymers. The aim of this work is to demonstrate that using stimuli responsive polymers is possible to achieve a reversible, fast and non-invasive tunability of photonic structures. The photonic structure that was chosen as case study is a 3D photonic crystal with a woodpile geometry. This structure whose optical properties tuning has been activated either by temperature or light variations behaves as a tunable filter at telecom wavelength. In addition, the improvement of the optical properties of the elastomeric photonic crystal has been demonstrated by using fabrication at low temperature (10 °C) via DLW.

5.1 Photonic crystals

Photonic crystals (PCs) are materials characterized by a periodic modulation of the dielectric constant in one, two or three directions (Figure 5.1) on a length scale of the same order of magnitude of the wavelength used to investigate them.

It was Lord Rayleigh in 1887 who first showed that it was possible to fabricate artificial materials in which light cannot propagate in a certain frequency range called photonic band-gap (PBG). Two- and three-dimensional structures with a photonic band-gaps were first introduced by Roland Zengerle [1], Eli Yablonovitch [2] and Sajeev John [3] in 1987 in order to control the spontaneous emission of light.

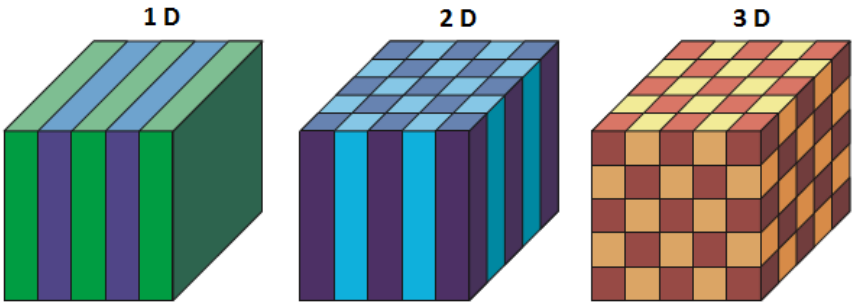

Figure 5.1. Schematic representation of the three categories of photonic crystals with the permittivity modulation in 1, 2 or 3 dimensions. Adapted from reference [4].

As in solid physics, the theoretical description of a PC can be made using a band diagram giving, for each value of the wave vector (**k**), taken in the crystal Brillouin zone, the frequencies corresponding to the electromagnetic modes supported by the structure. In order to predict the behavior of an electromagnetic wave in a PC, we must solve the Maxwell equations relative to a periodically modulated dielectric constant medium obtaining in this way the relative band diagram.

The simplest form of a PC is a periodic one-dimensional structure of a multilayer stack also called Bragg mirror, whose dielectric constant is periodic in one dimension. The structure is characterized by an alternation of dielectric layers with different permittivities ϵ_1 and ϵ_2. Two-dimensional photonic crystals, instead, are periodic in two directions and homogeneous in the third. These systems can have a photonic band-gap in the plane of periodicity. To open a band-gap in the plane or space, all uni-directional band-gaps must overlap at least partially on the first Brillouin zone. The most favorable situation is where the Brillouin zone is the most isotropic possible. Defects in two-dimensional crystals can localize modes in the plane, while the faces of the crystal can support surface states. Finally, three-dimensional photonic crystals are periodic along three axes. It is a remarkable fact that such a system can have a complete photonic band-gap, so that no propagating states are allowed in any direction of the crystal.

5.1.1 Three-dimensional photonic crystals

In three-dimensional PCs, the formation of a complete band-gap depends on several factors: the Brillouin area should be spherical because in this way the gaps

in the various directions tend to overlap. Moreover, it is fundamental a high index contrast of the PC with respect to the surrounding greater than 1.9. For this reason, silicon, which has a refractive index of around 3.5 is typically employed for 3D PCs. In case of low refractive index contrast, the structures do not have a complete band-gap, (i.e. propagation is not inhibited for all the directions of the incident light). In this particular case, we refer to a "stop band": it is created an interval of frequencies reflected only for a defined direction, perpendicular to the structure.

The first 3D PC was Yablonovite, working in the microwave range and made in 1993 by E. Yablonovitch [4] in holes in plexiglass at three azimuthal angles separated from ±120°. Fabrication methods for 3D PCs include drilling under different angles, stacking multiple 2D layers on top of each other, direct laser writing, or instigating self-assembly of spheres in a matrix and eventually dissolving the spheres for inverse designs. The two 3D PCs that have attracted the most research efforts are the woodpile (Figure 5.2.a) and the opal structures (Figure 5.2.b).

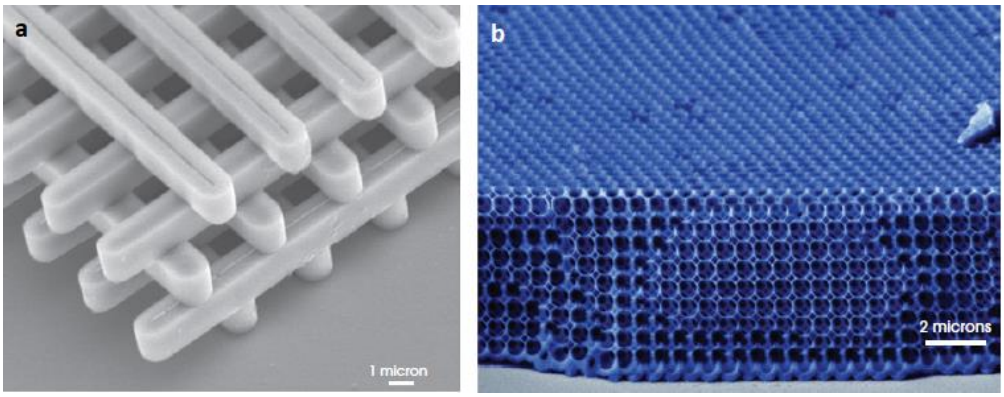

Figure 5.2. a) SEM image of a woodpile structure fabricated by UV-lithography in silicon. b) SEM image (artificial coloring) of inverse-opal structure. Adapted from reference [4].

Three-dimensional photonic crystals are expected to provide a fundamental building block for the realization of three-dimensional manipulation of photons. Actually, they have been developed and employed for several applications taking advantage of their defects for the realization of 3D waveguides, Bragg mirrors, switches, filters, superprisms, waveguides, optical resonators [5-7].

Historically, PCs have been made of inorganic high refractive index materials coupled to air to maximize the refractive index contrast and, therefore, the light confinement. However, these systems are complex, costly, and time-demanding, and the fabrication processes are difficult to scale. Polymers are good candidates to win this challenge [8]. Our experiments are focused on the fabrication of the first 3D woodpile PCs made of Liquid Crystalline Networks.

We report now more details about the 3D woodpile structure, object of study of this thesis.

5.2 Woodpile photonic crystal

The first three-dimensional photonic crystal with a complete band-gap that has been fabricated on micron scales, for light at infrared wavelengths, was the crystal shown in Figure 5.2.a. It is named "woodpile" and it is formed by a stack of dielectric "logs" (generally rectangular) with alternating orthogonal orientations. The woodpile-like stack have a four-layer ABCDABCD… sequence, in which C and D are layers with the same orientation as A and B, but are offset by half of the horizontal spacing.

Using a sequence of layers deposited and patterned by lithographic techniques, such as electron beam lithography the woodpile structure was fabricated out of silicon ($\varepsilon \approx 12$) logs by Lin et al. (1998) and a band-gap was measured around a wavelength of 1.2 μm. Deubel and co-workers [9] in 2004 demonstrated the possibility to obtain photonic stop band in the telecommunication range. By using direct laser writing, they manufactured high quality woodpiles made of SU-8™ (a commercial polymeric material), with fundamental stop bands ranging from 1.3 μm to 1.7 μm and a maximum transmission attenuation of about 70%. Marichy and co-workers [10] in 2015 achieved a direct inversion of polymer templates into TiO_2 based woodpile photonic crystals. The obtained structures show remarkable optical properties, in particular a complete photonic band-gap in the near-infrared region. Frölich and co-workers in 2013 demonstrated for the first time, photonic crystals with a complete photonic band-gap in the visible spectrum using STED-inspired direct laser writing and a novel titania double-inversion procedure [11].

Besides improving the photonic crystal optical properties and controlling the spectral range of the stop band, a reliable demonstration of the tuning of the

transmission dip of woodpiles has not yet been reported. The tuning of the optical properties has been demonstrated for other type of photonic crystals, such as opals and their inverse structure [12]. The first mechanically tunable woodpile PCs, exhibiting a strong peak in reflection in the mid-infrared, have been achieved by Chernow and co-workers in 2015 [13]. Another study toward tunable woodpile structure, realized via DLW, with reversibly addressable refractive indices, using polymerizable redox-active materials, have been shown in 2017 from Hu and co-workers [14]. Despite the refractive index switching reported in this work, the reversible stop band tuning has not been reported.

We demonstrate, here, the first 3D woodpile photonic crystals, fabricated via DLW in LCN matrices, with tunable optical properties using temperature as external stimulus. Moreover, for the first time, we demonstrate the effectiveness of the developed controlled temperature fabrication method for LCN matrices (previously described in Chapter 4) that enables to improve the attenuation of the stop band for woodpile structure direct laser written at 10 °C.

5.3 3D woodpile PC made of Liquid Crystalline Networks

Aiming to a tunable filter with an attenuation of the transmission at telecom range that can be controlled by temperature variations, we focused our research on the study, design, fabrication by Direct Laser Writing and optical characterization of a microscopic woodpile made by Liquid Crystalline Networks.

5.3.1 Fabrication of a LCN woodpile by DLW at room temperature

The LCN mixture employed as monomeric matrix for the fabrication of the first LCN micro-woodpile has been presented in Table 3.1 of Chapter 3: Cross-linker(30%). This choice has been dictated by the good rigidity of the mixture that allows to fabricate 3D structures with nanometric suspended elements, without losing its elasticity. After the definition of the suitable geometry to have a stop band in the NIR, the fabrication parameter, i.e. the power laser and the writing speed, have been set in the writing code file in such a way to obtain the desired structure. We set respectively 13 mW and 90 µm/s at room temperature.

In Figure 5.5 is reported the rendering of the 3D microscopic woodpile PC: the side view (Figure 5.3.a) and the top view (Figure 5.3.b), respectively. This 3D LCN woodpile is characterized by a face-centered cubic (fcc) lattice. It is made of 16 layers (4 periods), the length of each rod is 50 µm and the periodical pitch is

1.2 µm. The structure is sustained from a LCN base and four corner edges in order to reduce the shrinkage effect during the development process, of the upper layers compared to the lower ones. In addition, an elastomeric base has been introduced to facilitate the deformation of the woodpile structure as it reduces the anchoring of the photonic structure to the glass.

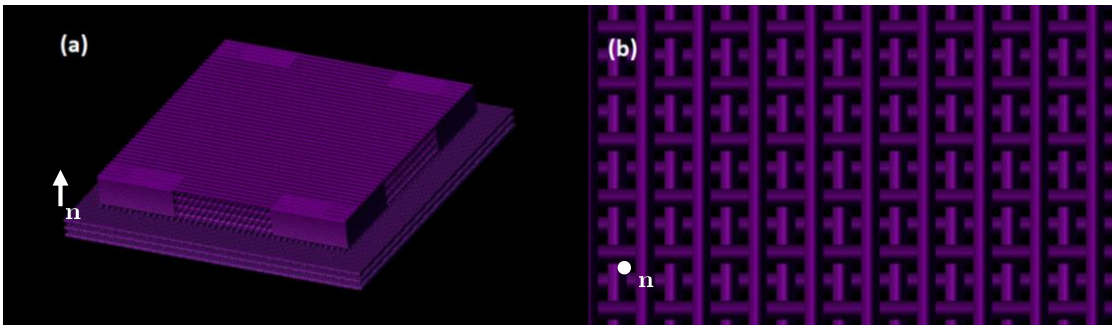

Figure 5.3. LCN woodpile realized via DLW technique: a 3D rendering of the structure, a) side view and b) top view, respectively. **n** is the LCN director.

The liquid crystal molecule alignment for these structures is homeotropic with the director parallel to the woodpile height. The chosen alignment allows under actuation to vary the periodicity along the LC director and therefore the stop band frequency range without introducing anisotropic deformation in the x-y plane. After the writing process, the LCN cell was removed from the sample holder, opened with a blade, and put in two development baths of 2-propanol at 75 °C, for 20 minutes and 10 minutes respectively in order to dissolve the unpolymerized material without any degradation of the polymerized structures. The molecular alignment has been verified using a polarized optical microscope. In Figure 5.4, POM images show that there is no difference in the transmittance for sample rotation of 45° demonstrating a good homeotropic alignment.

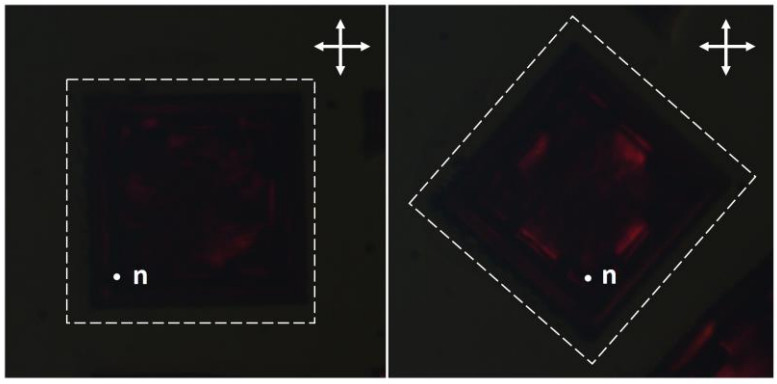

Figure 5.4. POM images. The LCN director is indicated by the versor **n**, perpendicular to the plane. The white arrows indicate the polarizer axes.

In order to improve the structure rigidity and reduce the stickiness, an UV post curing process has been performed on the micro-structure. Since DLW does not generate a full conversion of the acrylate moieties, the mechanical properties of the written structure can be improved by immersion into 12 mL 2-propanol and 50 mg of photo-initiator and irradiation with a UV lamp for 30 minutes, completing in this way the conversion of the polymerizable groups (see paragraph 1.3.5). Finally, the glass slide with the woodpile structure was once more gentle dipped into clean iso-propanol and air-dried. Figure 5.5 shows the woodpile PC structure, using an optical microscope (50x), before and after the UV post curing treatment without any degradation.

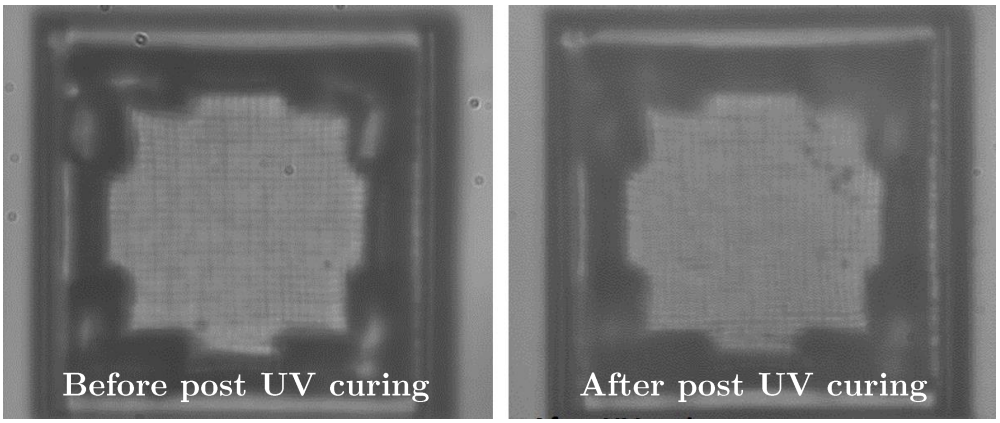

Figure 5.5. Post-print UV curing method: optical microscope images show the same final structure developed directly after writing (on the left) and subjected to UV curing (on the right).

In Figure 5.6 is reported the SEM image of a typical LCN woodpile polymerized by direct laser writing at room temperature (22 °C) with a power laser of 13 mW and a writing speed of 90 µm/s. In this sample, the four edges have not been fabricated in order to highlight the complete layered structure of the LCN woodpile PC and appreciate the shrinkage effect on the PC top layers.

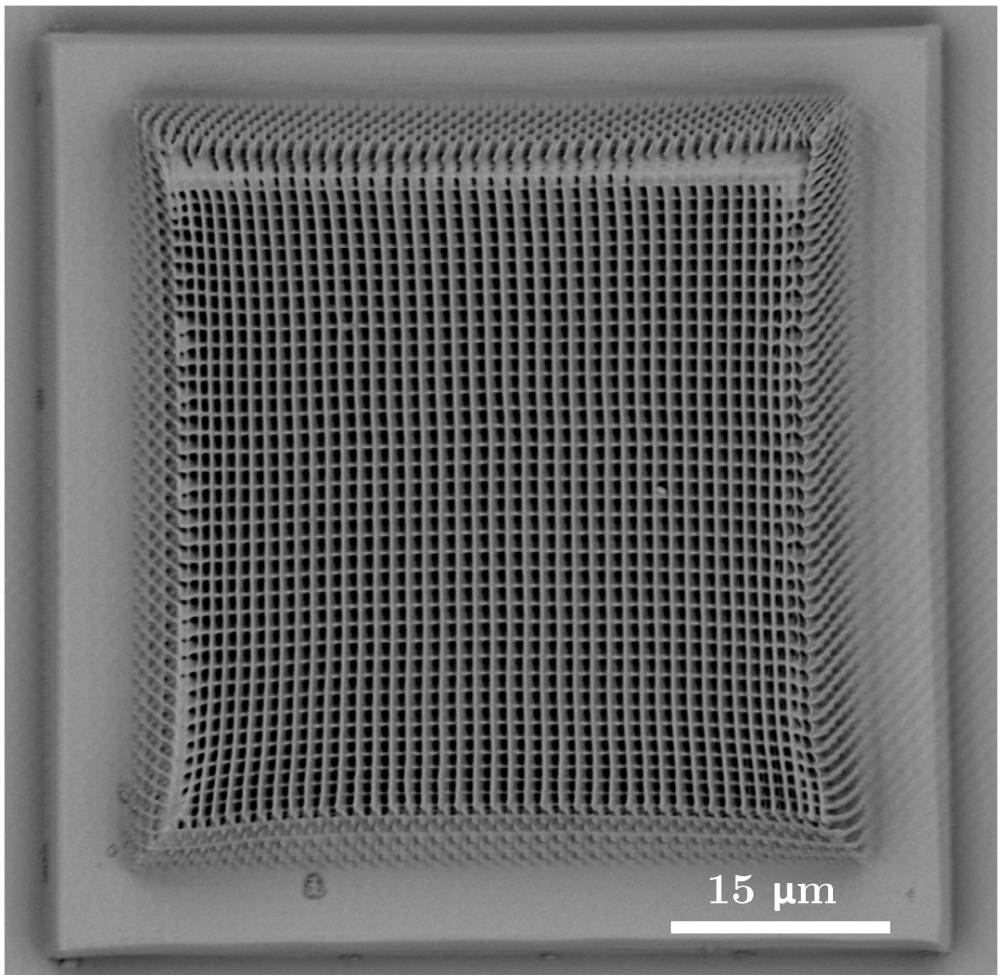

Figure 5.6. SEM image of the LCN woodpile PC polymerized by DLW.

5.3.2 Optical characterization

The woodpile response, working as a telecom optical filter, has been measured with the experimental setup reported in Figure 5.7. The transmission spectroscopy setup is constituted by a super-continuum source (Fianium Whitelase supercontinuum laser SC-400-4) linearly polarized through a high damage threshold polarizing cube beam splitter. An acousto-optic tunable filter (AOTF) is used to rapidly and dynamically select a specific wavelength from the broadband laser source in the range from 1300 nm up to 1800 nm. The monocromatic light, having a spectral resolution of around 1 nm, is then focused on the sample with a lens doublet for the infrared with a focal length of 35 mm. The transmitted light is collected with a long working distance objective 20x (Mitutoyo Plan Apo NIR Infinity Corrected Objective). A tube lens with a focal length of 200 mm focalizes the image in a back focal plane, in which a spatial filter is placed in order to collect only the k vectors perpendicular to the substrate. A flipping mirror allows to

deviate the beam on a near-infrared camera (Indigo Phoenix) in order to locate the woodpile with a defocused laser light and put the focused spot in the middle of the chosen structure. Once aligned the sample, the transmitted light is collected by an InGaAs photo-diode (Hamamatsu-G12182). A signal frequency modulation done with a chopper in combination with a lock in are used to reduce the noise.

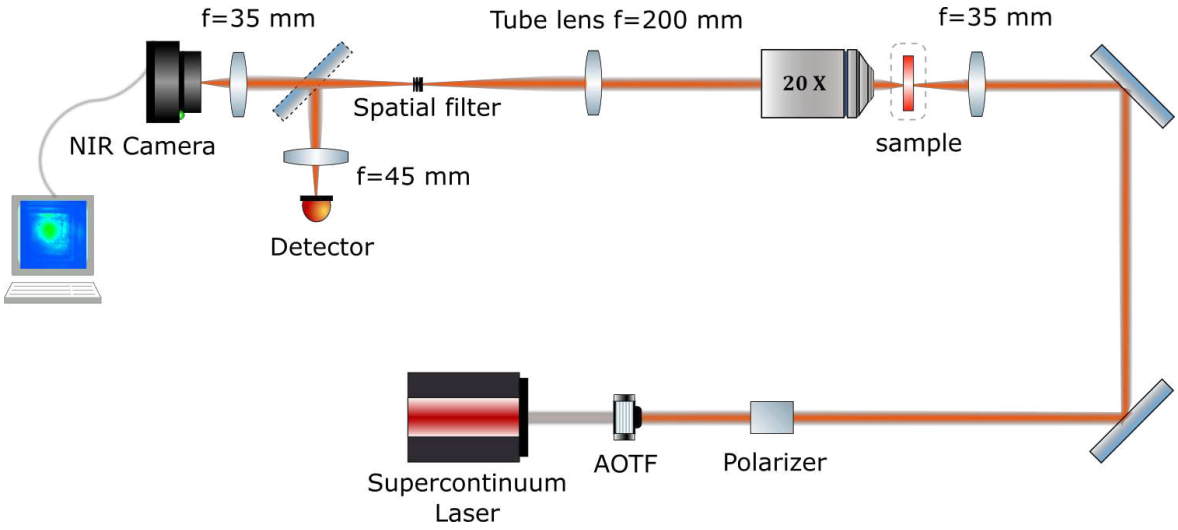

Figure 5.7. Experimental set up for the optical characterization of woodpile PCs.

Due to the not perfect reproducibility of the fabrication process on soft materials, two nominally identical structures create different transmission spectra as shown in Figure 5.8.

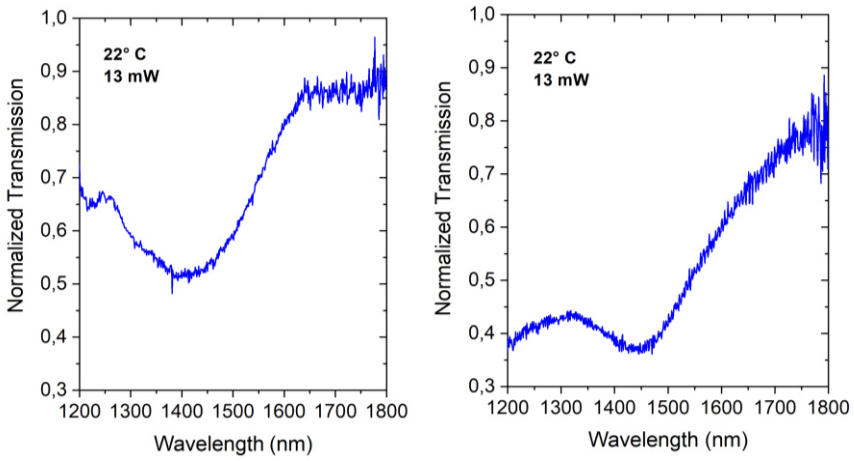

Figure 5.8. Stop band of two different woodpile PCs fabricated using the same writing parameters at room temperature.

In Figure 5.9.a is reported a typical transmission spectrum of a LCN woodpile PC (before and after UV curing), measured with the optical set up shown in Figure 5.7. Because of the non-perfect homogeneity of the structures, scattering phenomena occur with a consequent decrease of the transmitted intensity. For this reason, the total transmittance is less than the 60% (The transmission spectrum has been normalized to the glass substrate reference). At present, the transmission attenuation of 63% for the LCN woodpile is lower and cannot be compared with respect to the one of about 90%, obtained in case of the IP-Dip™ woodpile (Figure 5.9.b). However, if we consider the soft and elastic nature of these elastomeric materials, the achieved result represents a first step in the manufacture of woodpile photonic structures made with these smart photonic materials.

In case of the commercial material Ip-Dip™, the good transmission attenuation is due to the better resolution and less shrinkage of the fabricated structure, as shown in the SEM image of Figure 5.9.c, in which a 50 µm x 50 µm IP-Dip™ woodpile, fabricated at 90 µm/s at 13.8 mW is reported and in Figure 5.9.d, in which a detail magnification of the same structure is shown. The rods separation is 1200 nm.

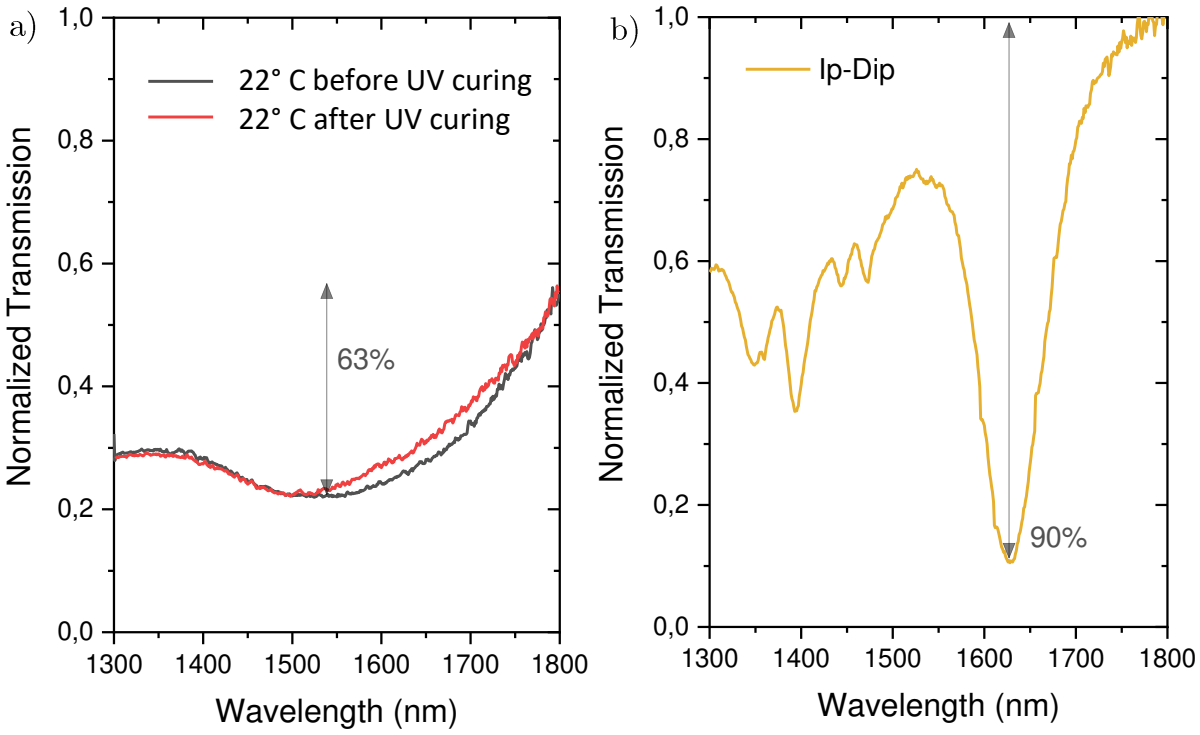

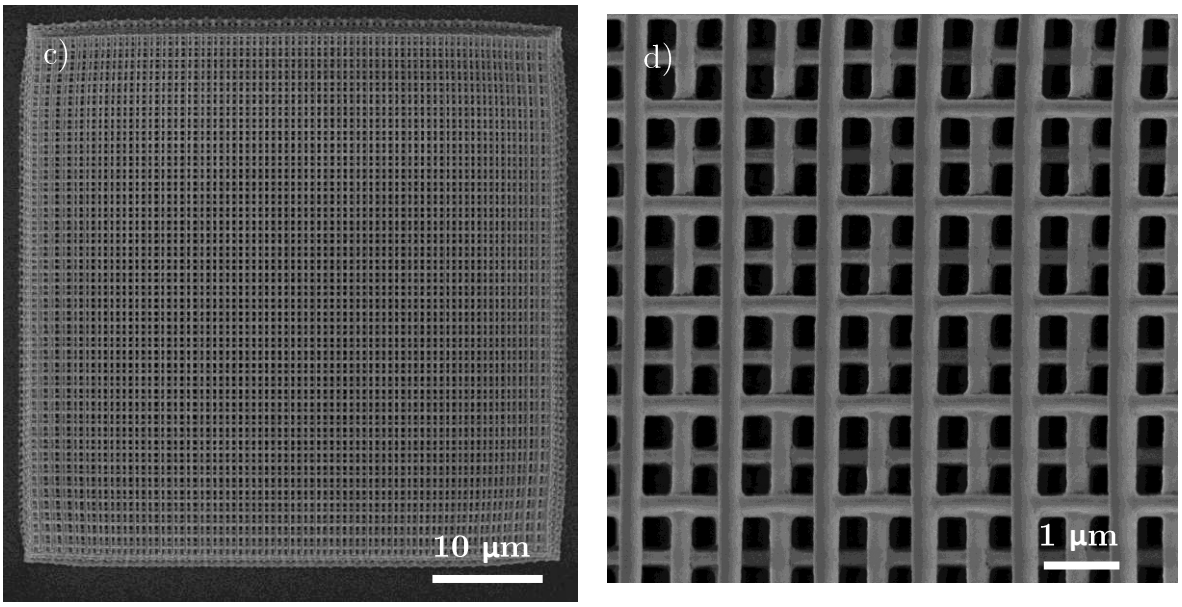

Figure 5.9. a) Stop band before (black line) and after (red line) post UV curing of a typical LCN woodpile PC. The transmission attenuation is 63%. b) Stop band of a typical IP-Dip™ woodpile PC. The transmission attenuation is 90%. c) SEM image of a 50 µm x 50 µm IP-Dip™ woodpile. d) SEM detail magnification of a 50 µm x 50 µm IP-Dip™ woodpile.

5.3.3 LCN woodpile fabricated via DLW at 10 °C

To improve the optical properties, reducing the swelling and decreasing the aspect ratio of the voxel, we adopted the best fabrication parameters selected in Chapter 4, controlling the polymerization temperature. In this case, the 3D polymerizable unit, obtained at 10 °C with a writing speed of 90 µm/s and a laser power of 11.2 mW, is now comparable with the typical voxel dimensions of commercial resists and enlarges the application field of photo-responsive elastic materials without degradation of the patterned structure rigidity. In particular, a spheroidal voxel would be the best polymerization unit to fabricate three-dimensional structures, especially in 3D photonic structures as woodpile photonic crystals and in our case, this has enabled to pattern a LCN woodpile with a better rigidity and resolution.

The optical characterization of three different elastomeric woodpile PCs with the same fabrication parameters is shown in Figure 5.10.a. We can assert that controlling the polymerization temperature is possible to obtain highly reproducible photonic structures with negligible differences in the stop band. In Figure 5.10.b is

reported a comparison of the optical characterization of the LCN woodpile fabricated via DLW at 10 °C with the LCN woodpile fabricated at 22 °C and the transmission spectrum of an IP-Dip™ woodpile. In case of LCN woodpile fabricated at room temperature, we measured a maximum transmission attenuation of 63%, while for the structure at 10 °C, an attenuation of transmission of 83% has been measured. This result, for the first time achieved in the state of the art, is more close to the transmission attenuation of 90% of the commercial IP-Dip™ woodpile and demonstrates the effectiveness of the previously developed low temperature fabrication method for LCN matrices.

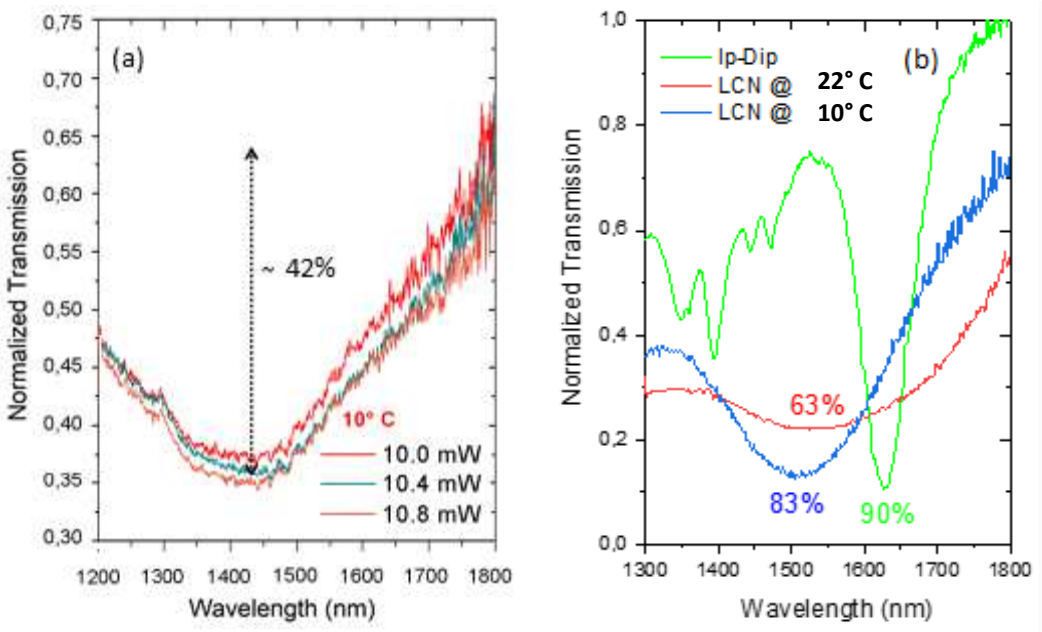

Figure 5.10. a) Optical characterization of three different elastomeric woodpile PCs fabricated at 10 °C via DLW with the same fabrication parameters. b) Transmission spectrum of a LCN woodpile realized at 10 °C (blue), at 22 °C (red) and IP-Dip™ woodpile PC (green).

5.3.4 UV post curing of LCN woodpile photonic crystals

We show here the possibility to employ Liquid Crystalline Networks as "smart" stimuli responsive materials to tune the optical properties of a LCN woodpile, using temperature as an external stimulus. As a first step we applied the post-print UV curing method on the LCN woodpile PC, fabricated via DLW.

In Figure 5.11.a, the transmission spectra (before and after the UV post curing) for a typical LCN woodpile structure are reported, showing as the chemical treatment promotes a slight increase of the transmission attenuation from 49% to 57%. The here analyzed woodpiles have been fabricated without the elastomeric base and it is possible to observe that in this case, the PC has an unitary transmission for wavelength above the stop band, showing that the base presence introduces some defects limiting the transmission.

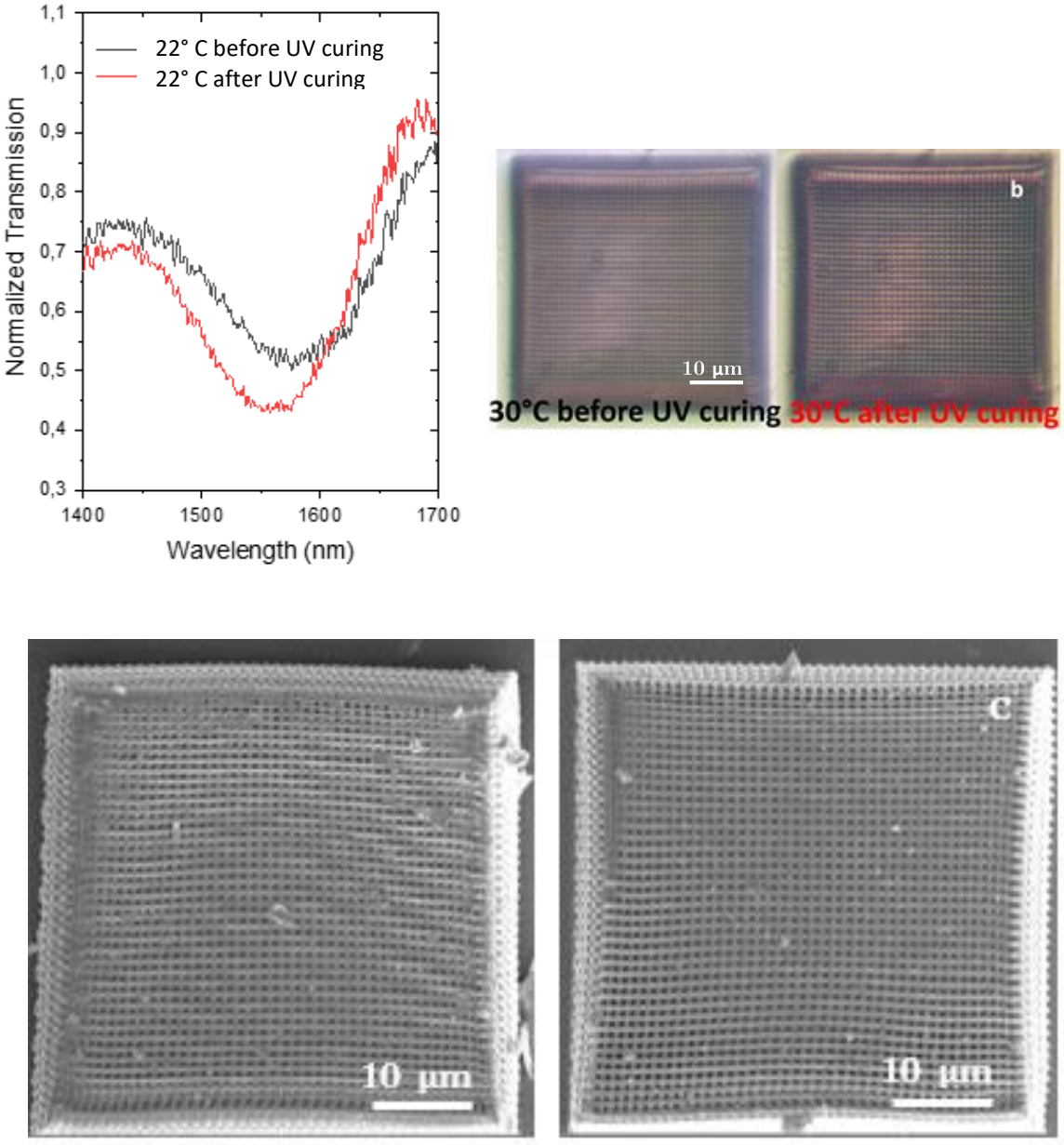

Figure 5.11. a) Stop band of a LCN woodpile without the base, realized at room temperature via DLW, before (black line) and after (red line) the UV post curing. The treatment promotes a transmission attenuation from 49% to 57%.

b) LCN woodpile before and after the UV post curing, observed under an optical microscope (50x). c) SEM images of LCN woodpile before and after the UV post curing showing as the treatment increases the rigidity with a reduction of the rods swelling.

Figure 5.11.b reports the woodpile structure (before and after the UV curing), observed under an optical microscope (50x). Optical images show that after UV post curing there are no appreciable geometric variations without any degradation. While SEM images of Figure 5.11.c show as the treatment increases the rigidity with a reduction of the rods swelling.

5.3.5 Tuning of the stop band at telecom range by temperature variation

As a second step, the LCN woodpile has been inserted in a hot stage to vary the sample temperature. In this way, the stop band shift has been triggered by changing temperature from 30 °C to 50 °C, as reported in Figure 5.12, obtaining a transmission red shift. Decreasing the temperature up to room temperature (30 °C), the stop band acquires its initial shape again showing a reversible optical properties tuning.

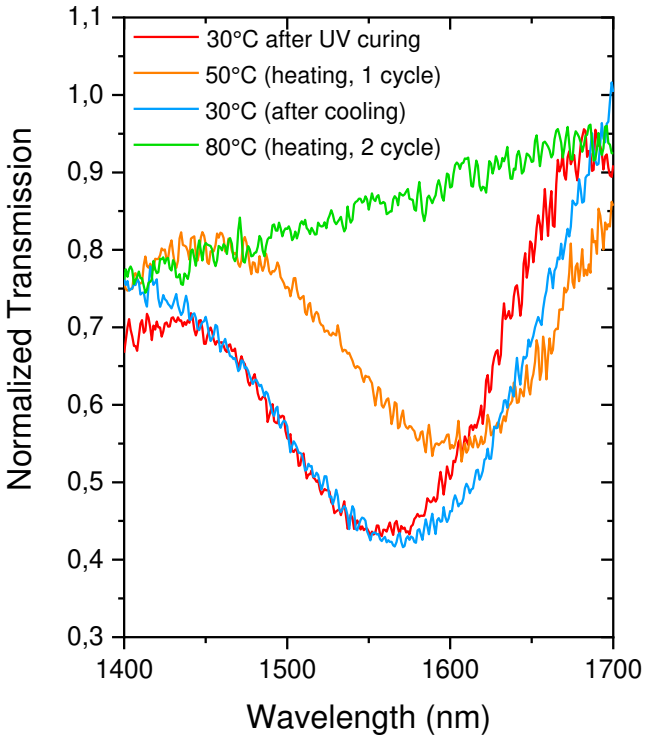

Figure 5.12. Optical characterization of a LCN woodpile PC, realized at room temperature, reporting the temperature variation spectra.

However, increasing further the temperature up to 80 °C the spectrum becomes completely flat. At this point the woodpile is irreversibly damaged due to the important material deformation that favors the rod merging in a bulk structure as shown in Figure 5.13.

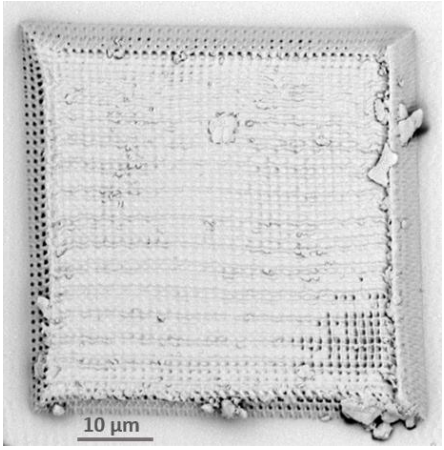

Figure 5.13. SEM image of a LCN woodpile PC after heating at 80 °C showing the link of the rods and resulting in a bulk structure.

It has not been yet possible observing the stop band tuning reversibility under several cycles. Therefore, at present, it is necessary to further reduce the material stickiness with proper chemical treatments. However, these experiments based on temperature modulation open the door to the possibility of demonstrating a reversible optical tuning, the final goal of this work, which will have a technological impact on the optical switching at telecom wavelengths. In the following paragraph we describe the first results towards this goal, using light as activation stimulus.

5.3.6 Towards the tuning of the woodpile stop band by light

In order to have a photo-responsive woodpile PC, an azo-dye (depicted in Figure 1.11), having a minimum absorption around 390 nm and a transparency window above 700 nm [15], has been added to the mixture. Therefore the elastic PC has been then illuminated via a continuous wave (CW) green diode laser (532 nm).

We have observed the woodpile activation with the consequent deformation when the structure, after the UV post curing, was illuminated by the green laser, as shown in Figure 5.14. In the woodpile structure, detached from the substrate, the deformation is more evident.

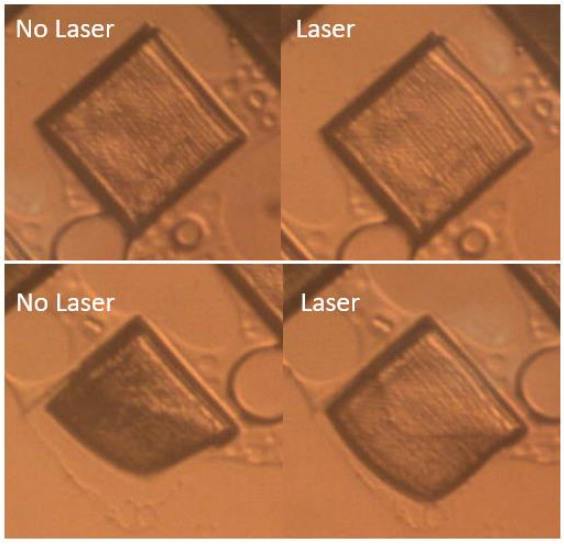

Figure 5.14. Deformation of two different LCN woodpiles illuminated by a CW green laser diode.

However, despite the low power values used to illuminate the micro-structures (up to ≈ 7 mW), light-induced tuning of the transmission spectra has not been observed. The laser illumination obtained by focusing the green laser spot in the center of the microscopic LCN woodpile damaged the structures that show the rods merging as shown in Figure 5.15, in which the LCN woodpile, observed under optical microscope, is reported before (a) and after (b) the green laser illumination. Also in this case it is necessary a further increase of the rigidity of the LCN polymerized structure.

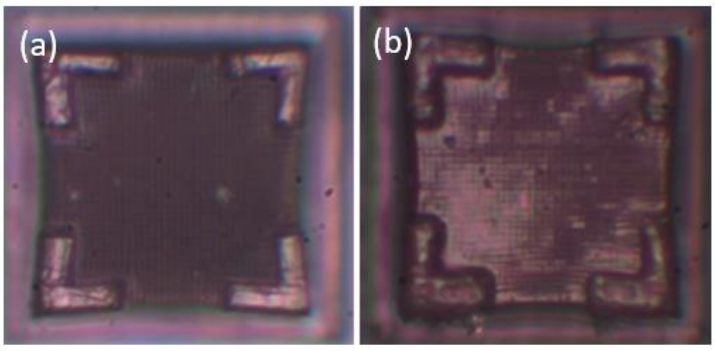

Figure 5.15. Optical microscope images show the same structure before (a) and after (b) CW green diode laser illumination with the consequent structure damage.

References

[1] R. Zengerle, J. Mod. Opt., 1987, 34, 1589-1617.

[2] E. Yablonovitch, Phys. Rev. Lett., 1987, 58, 2059-2062.

[3] S. John, Phys. Rev. Lett., 1987, 58, 2486-2489.

[4] J. D. Joannopoulos, S. G. Johnson, J. N. Winn, and R. D. Meade. Photonic crystals. Princeton University Press, 2008.

[5] K. Ishizaki, M. Koumura, K.Suzuki, K.Gondaira, and S.Noda. Nat. Photonics, 2013, 7, 133-137.

[6] C. Paquet and E. Kumacheva. Mater. Today, 2008, 11, 48-56.

[7] Y. Ohtera and H. Yamada. IEICE Electron. Expr., 2013, 10, 8, 1-13.

[8] P. Lova, H. Megahd, P. Stagnaro, M. Alloisio, M. Patrini and D. Comoretto, Appl. Sci. 2020, 10, 4122.

[9] M. Deubel, G.von Freymann, M. Wegener, S. Pereira, K. Busch, C. M. Soukoulis, Nat. Mater. 2004, 3, 444−447.

[10] C. Marichy, N. Muller, L. S. Froufe-Pérez, and F. Scheffold, Sci. Rep. 2016, 6, 21818.

[11] A. Frölich, J. Fischer, T. Zebrowski, K. Busch, and M. Wegener, Adv. Mater. 2013, 25, 3588-3592.

[12] B. C. I. Aguirre, E. Reguera, and A. Stein, Adv. Funct. Mater. 2010, 20, 2565-2578.

[13] V. F. Chernow, H. Alaeian, J. A. Dionne, and J. R. Greer, Appl. Phys. Lett. 2015, 107, 101905.

[14] Y. Hu, B. T. Miles, Y. L. D. Ho, M. P. Taverne, L. Chen, H. Gersen, J. G. Rarity, C. F. Faul, Adv. Opt. Mater. 2017, 5, 16004.

[15] H. Zeng, D. Martella, P. Wasylczyk, G. Cerretti, J.C.G. Lavocat, C.H. Ho, C. Parmeggiani, and D. S. Wiersma, Adv. Mater. 2014, 2, 2319.

Chapter 6

6 Color modulation in *Morpho* butterfly wings using Liquid Crystalline Elastomers

In Chapter 6 the research work, developed during a six-month period in collaboration with Prof. Li and Prof. Keller group in Paris, at Chimie ParisTech, is described. A new biotic-abiotic platform capable of color tuning in response to temperature changes is presented. We explored the integration of the Morpho butterfly wing, owing an optimized structural coloration due to its natural photonic crystal structure and superhydrophobic properties, and the efficient thermo responsive deformation of Liquid Crystalline Elastomers, whose properties have been customized at Chimie ParisTech laboratories. The novelty of our demonstration is not represented by the singular materials but by their combination into a first proof of a smart visualizable sensor. This combination leads to a thermo sensitive tuning of the optical and mechanical properties of the hybrid bilayer that changes its color and create a self-cleaning platform exploiting the butterfly hydrophobicity. At the same time, the thermally driven mechanical control of the color tuning allowed also to better understand the mechanism of structural coloration and how the different geometrical parameters contribute to the resulting reflectance.

6.1 Natural photonic crystal as template for tunable structural colors

The study of evolutionarily optimized solutions of animals and plants is used in biologically inspired engineering to find inspiration for the development of better devices and technology. In nature, the morphology of living systems is responsible not only for the biological functions but frequently also for their appearance. A fascinating feature based on material architecture is that of structural coloration,

which receives growing interest for the development of efficient reflective coatings, photonic devices as well as optical sensors [1-3].

An inspiring example is provided by the nano architecture of the butterfly wings. Among them, the color of *Morpho Menelaus* [4-6] is mainly determined by the interaction of light with the wing's complex scale morphology that produces a brilliant blue structural color as a sum of multiple optical effects.

A specific characteristic of this species is the low angular dependence of wing coloration that remains bluish over a wide range of viewing angles, in contrast to what is typically observed in many other structural colors [7]. This unique property motivated a profound exploration of the morphology of the wing scales that are constituted by nanostructured cover and ground scales. The scales are nanostructured in ridges with a lamellar structure ("Christmas tree" like structure) with slightly different periodicity and a certain ridge height distribution [4]. Such complex quasi periodic arrangement rules the *Morpho* butterfly appearance: a quasi-multilayer interference at the lamellae level combines with diffraction of the ridges creating a brilliant slightly angle-dependent iridescence [5].

Morpho species have been classified according to the overlapping of ground and cover scales and the number of lamellae [6]. For *Morpho* species with a ridge morphology constituted by a small number (three or four) of lamellae, a successful replica has been reported using ferroelectric ceramic materials that however do not offer any tunability effects [8]. Although many strategies have been reported aiming at replicating the butterfly structure [9-13], a faithful replica of the more complex morphologies (characterized by the multi-scale periodicity of the *Morpho Menelaus* butterfly scales, and the aspect ratio of its 3D nanostructuration), is still missing using non commercial polymers. In fact, structural colors were recently generated by *Morpho*-inspired structures, realized via DLW, but employing commercial polymers [14]. In order to obtain a tunable structural colored surface, we think soft deformable materials, as PDMS mold or Liquid Crystalline Elastomers, are good candidates and should be envisioned for the replica of the butterfly. Achieving this goal would open new routes for photonic applications, sensing applications, tunable colors and colorful hydrophobic coating [11, 15, 16].

Aiming at a responsive tunable optical platform, *Morpho* butterfly wings were demonstrated to be suitable not only as a template but also as a main constituent of integrated responsive devices. By coating the *Morpho* wing with photo-responsive linear polymers, a light induced color change with a 70 nm blue shift has been

demonstrated [17]. In sensing application, a bio-hybrid platform made by a multi-layered structure of cardiomyocytes and carbon nanotubes superimposed to the butterfly wing showed a relevant color variation in response to the beating of cardiac muscle cells [18]. In both cases, polymers or cardiomyocytes and carbon nanotubes were placed on the top face of the wing with multi-scale periodic structures. Consequently, the appearance of the butterfly wing is strongly affected by the coating layers that change the structural coloration by modifying the refractive index contrast.

6.2 *Morpho* butterfly wing integrated with liquid crystal elastomers

To preserve the natural coloration of the *Morpho* butterfly, we investigated an assembled hybrid system made by the butterfly wing and an artificial muscle based on Liquid Crystal Elastomers (LCEs), where LCEs were placed on the back side of the wing thus keeping the color-generating top face free of contamination. This hybrid system benefits from both the optimized reflectance of the butterfly wing and the large and easily controllable contraction/expansion of the LCE artificial muscles. Such biotic-abiotic composite materials provide not only a mechanical actuation to tune the optical properties of the wings but also a deeper insight in the mechanism underlying the principle of the coloration of the *Morpho* butterfly. Moreover, such integration explores a new route for functional optical devices where an optimized photonic architecture can be coupled to a stimuli responsive material to tune the optical properties. In our study, a natural optimized platform was employed, but this approach could be further extended to other devices with selective reflection properties such as Bragg multilayers [2], flexible metal coatings and photonic crystals [19].

6.2.1 LCE artificial muscles

The remarkable property of LCE artificial muscles [20-26] is their shape change under an external stimulus such as temperature variation or light illumination. Taking advantage of their responsiveness to different stimuli and specifically to light [26, 27], they have been extensively explored in many research fields, from robotics [28, 29], to microfluidics [30], and photonics [31]. Within the latter, LCE

deformable elements can be used as actuators to remotely control the position of optical components as a mirror to steer a beam towards different adjacent directions [32], or they can work themselves as photonic materials whose refractive indices and shape can be dynamically tuned by light [33, 34]. Furthermore, an example of hybrid material composed by LCEs and a synthetic photonic crystal (a silica opal) has been recently described [35] while the interplay of LCE with natural structural color has been rarely explored [17].

For this application/demonstration, the employed artificial muscles are nematic LCEs made of slightly cross-linked main-chain LC polymers. The principle of artificial muscle's contraction/elongation resides in the conformational change of the nematic LC polymer chain upon nematic (N)–isotropic (I) phase transition at T_{NI}. In the LC phase, the conformation of the macromolecular backbone is coupled with the orientational order of the mesogen units. In the nematic phase, the orientated mesogens force the polymer chains to stretch along the direction of the orientation [36-38]. However, when the transition from nematic to isotropic phase takes place, the orientational order is lost; consequently, the polymer chains can go back to the usual random coil conformation. Meanwhile, thanks to the cross-linked network, the orientational order of mesogens and the elongation of polymer chains can be restored to their original states at the nematic phase temperature. In an aligned macroscopic sample (monodomain), this reversible conformational change of polymer chains results in the reversible macroscopic shape change of LCEs, whose contraction/elongation behaves similarly to real muscles.

6.2.2 Two coupling integration strategies

The control over the structural color of the *Morpho* butterfly is achieved by exploiting two different LCE coupling strategies. LCE film can be firstly prepared by photopolymerization and then paired on the back and uncolored side of the *Morpho* wing. This way, the color variation induced by the natural wing flapping is reproduced upon thermally activated contraction/elongation of the LCE film (effect on the macroscale). Alternatively, thin LCE film can be prepared in-situ by direct infiltration of monomeric mixtures in the wings' back side followed by polymerization in their aligned state. A local deformation of the scales' dimensions and nano-structuration is thus achieved (effect on the nanoscale). In the former approach, the mechanical energy obtained by the thermosensitive deformation of the LCEs is used to reversibly control wing flapping, changing the resultant

structural coloration for a fixed viewing angle. Interestingly, the variation of the contact angle is also observed, which has been exploited to control liquid droplet rolling along the ridge direction. In the latter approach, LCEs allow to elastically deform the single scale and thus the nanostructure periodicity that is thus responsible for the blue shift of the reflectance peak. In brief, the assembled biotic-abiotic hybrid systems described here afford a smart multifunctional platform that shows structural color tuning and droplet motion on its super-hydrophobic surface in response to temperature variation. More details about the delicate processing steps, which characterize the two coupling integration strategies, are described later. We focus now on the description of the natural photonic structure employed in this work: the *Morpho Menelaus* blue butterfly.

6.3 *Morpho Menelaus* blue butterfly

6.3.1 Morphology

In this work, a highly iridescent butterfly specie, the *Morpho Menelaus*, was studied (Figure 6.1a) which has a bright blue coloration with a particular viewing-angle dependence of the wing color. The nanostructured morphology determines an extremely high reflection, which depend strongly on the wavelength, polarization state, angle of incidence and the refractive index of the ambient medium [5]. *Morpho Menelaus* butterfly wing has two types of scales (cover and ground scales, shown in Figure 6.1b-c), both of which have straight ridges of a height of 2-3 µm, separated by a distance of about 1 µm [39]. Both cover and ground scale ridges are characterized by a lamellar structure that determines the *Morpho* butterfly iridescence. Each scale is characterized by ridges (or vanes) aligned along the long size of the scale whose periodicity mainly affects the butterfly appearance. The distance between adjacent ridges of the cover scale is approximately 1700 nm (Figure 5.1.d), while in the ground scales the vanes are approximately 700 nm apart (Figure 5.1.e). The two scales have a different role in the color determination: the cover scale mostly diffuses light while the ground scale is responsible for the structural color. The superposition of the two determines the blue coloration [40].

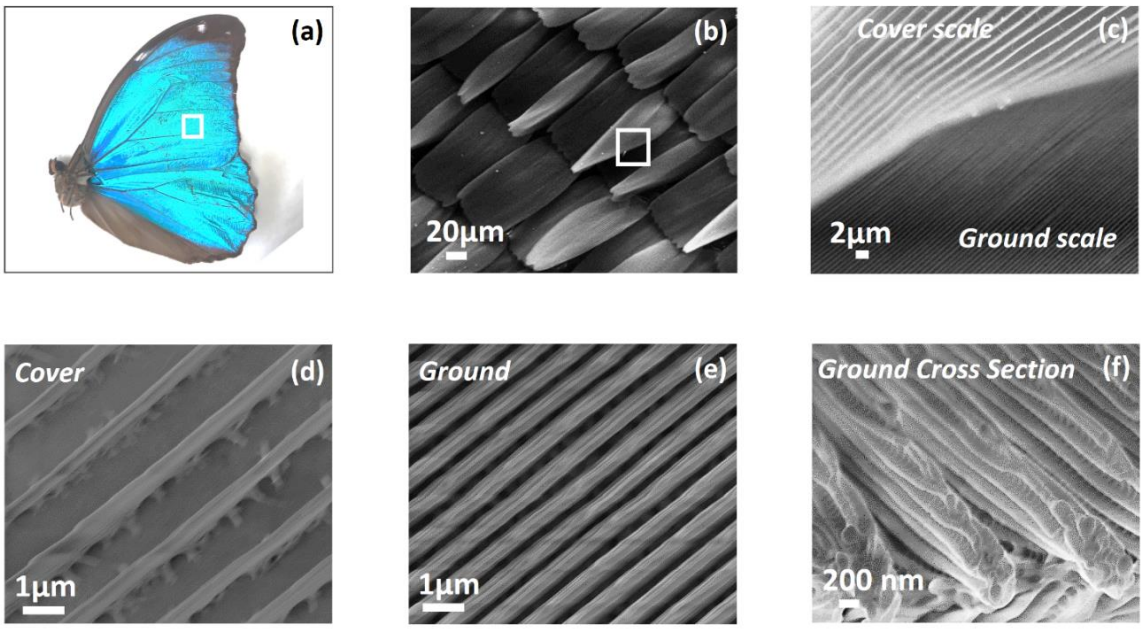

Figure 6.1. a) *Morpho Menelaus* blue butterfly. b) SEM (scanning electron microscope) image. The ground scales have a rectangular shape and a typical size of 160 µm in length and 90 µm in width, while the cover scales have a quasi-rectangular shape and a reduced lateral size. c) SEM image magnification of ground and cover scale detail. Both scales show a periodic arrangement of longitudinal vanes (or ridges). d) SEM image of cover scale vanes showing 1700 nm separation between adjacent ridges. e) SEM image of ground scale vanes showing 700 nm separation between adjacent ridges. f) A lateral SEM image of the ridges of the ground scale cross-section, showing structures with overlapping lamellae.

The nanometric structure has been characterized using scanning electron microscope (SEM) images shown in Figure 6.1d-f. The ground scales have a rectangular shape, whose typical size is 160 µm in length and 90 µm in width. Cover and ground scales are attached to the wing membrane alternately through holes called sockets. The shape of the cover scales varies from species to species. In *Morpho Menelaus*, the shape is quasi-rectangular, but the lateral size is shorter.

A single cover scale and a ground scale, isolated from the wing of *Morpho Menelaus* butterfly, have been observed both in transmission (Figure 6.2.a) and under white light (Figure 6.2.b). The cover scale looks transparent, while the ground scale looks dark brown, meaning that a pigment also induces the coloration. Moreover, white light reflectance shows that the ground scales have a deep blue

coloration because the internal scale nanostructures are responsible of the butterfly appearance. Also, in Figure 6.2.c, the cover scales are not clearly visible because they are transparent, while under white light of Figure 6.2.d, the bright blue coloration increases when ground and cover scale overlapped each other.

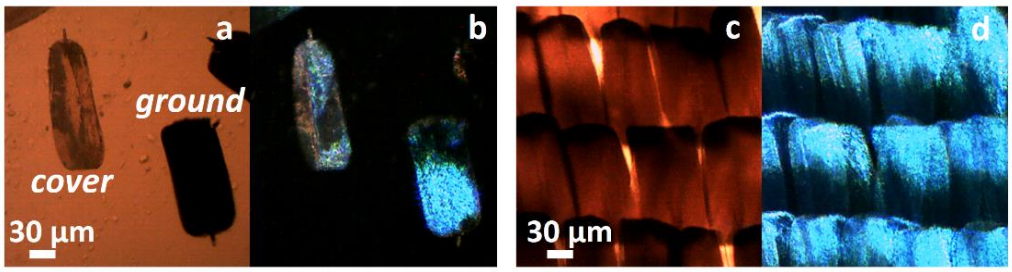

Figure 6.2. a) Single cover and ground scale observed by a transmission optical microscope. b) Reflection of the same scales illuminated by white light at 45°. c) Transmission optical microscope image of the *Morpho* butterfly wing in which cover scales and ground scales are overlapped. Cover scales seem absent because they are almost completely transparent. d) Reflection of the butterfly wing illuminated by white light.

Looking from above and illuminating with white light at 45° with respect to wing normal (Figure 6.3.a), an in-plane rotation (in the wing plane) shows that the reflectance depends on the orientation of the scale with respect to the illumination direction (Figure 6.3.b).

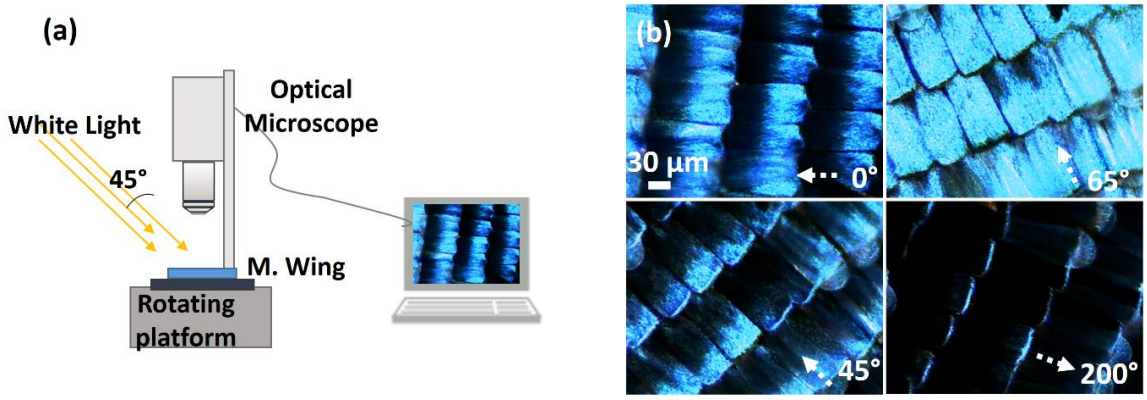

Figure 6.3. a) Schematic of the experimental set-up in which the incident light direction with respect to butterfly wing sample is drawn. b) Images of *Morpho Menelaus* butterfly wings (for different angles: respectively 0°, 45°, 65° and 200°)

for an in-plane rotation with white light illumination fixed a 45° with respect to the wing normal.

A careful observation of the ground scale morphology shows that each ridge has a laminated structure of several lamellae superimposed on each other and slightly tilted on the scale plane (Figure 6.1.f and Figure 6.4.a). From an optical point of view, these scales behave like a two-dimensional periodic structure. In the scale plane, previous characterizations report that a ridge separation of 600 nm (in our sample 700 nm) results in a diffraction effect, while the lamellae of a mean thickness of 100 nm (in our case 110 nm), having a multilayered ordered structure, produce interference in the blue part of the visible spectrum [41].

The ground scale cross section, observed with scanning electron microscope (Figure 6.4.a), allowed determining the lamellae arrangement in ridges. They appear to be disposed in alternated fashion on both sides of the trunk of the ridge. The lamellae thus form a reflection plane that is not perpendicular to the axe of the ridge, but inclined at a slight angle ($\theta \approx 20°$ for *Morpho Menelaus*) [42], as shown on the bottom magnification of Figure 6.4.a.

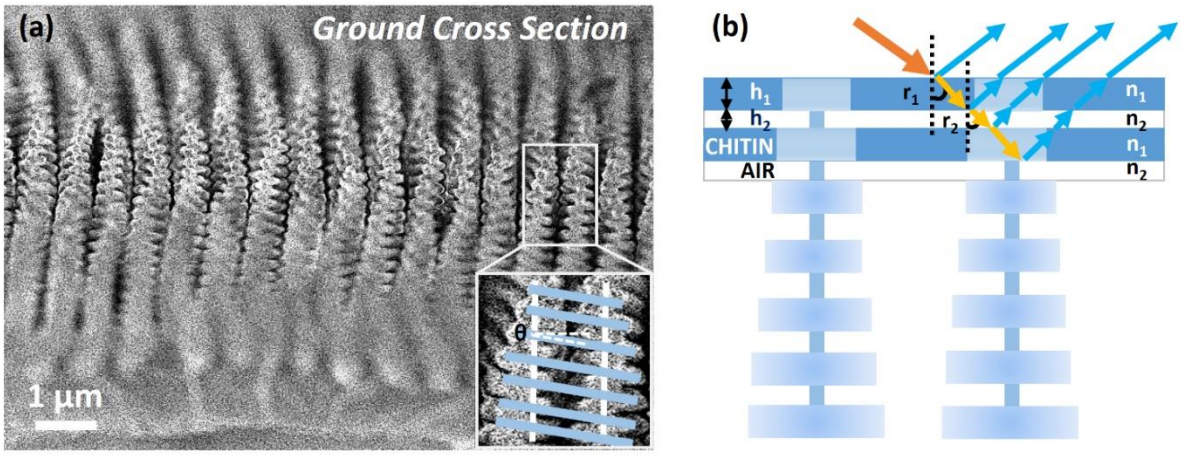

Figure 6.4. a) SEM image of ground scale cross section showing the "Christmas-tree" nanostructure of the ridges composed of alternating layers of chitin and air. In the magnification, a schematic representation of the thin layers formed by the lamellae is drawn. The lamellae are inclined of a slight angle ($\theta \approx 20°$ for *Morpho Menelaus*) with respect to the axe of the ridge. b) 1D simplified model based on the multilayer-thin-film interference.

To calculate the peak wavelength of the reflectance, we used a 1D simplified model based on the multilayer-thin-film interference: the lamellae (Figure 6.4.b) are considered symmetrically distributed on both sides of the trunk and parallel to the base. We measured the various thicknesses from the SEM image. The chitin and air layers are designed with thicknesses $h_1 = 112 \pm 5$ nm and $h_2 = 65 \pm 5$ nm and the refractive indices are set to $n_1 = 1.555$ and $n_2 = 1$, respectively. The thin-film multilayer interference can be applied as follows [43]: $\lambda_{\text{max peak}} = 2\,(n_1 h_1 \cos r_1 + n_2 h_2 \cos r_2)$, where the angles of refraction within the layers of chitin and air are r_1 and r_2, respectively. The wavelength of reflected light changes with the thickness, refractive indices, and the reflection angle. In case of normal incidence $r_1 = r_2 = 0$, we obtained a calculated peak of 478 ± 18 nm, where the error has been calculated according to the error propagation.

6.3.2 Reflectance characterization

The spectral characterization was done by using the optical setup reported in Figure 6.5.a. The light emitted from a halogen lamp was first collimated through a system of lenses and then focused on the butterfly sample by a doublet lens (30 mm focal length). A 10x objective collected the reflected light that is analyzed by an Ocean Optics USB4000 spectrometer having an optical resolution of about 1.5 nm. We focused on the reflectance spectrum in the visible spectra range from 400 nm to 650 nm. To characterize the wing iridescence, the sample has been tilted at different angles from 0° to 50° with steps of 10° (Figure 6.5.b and Figure 6.6.a), keeping fixed the illumination and collection direction. The sample was always oriented with scale ridges perpendicular to the plane of incident light because reflectance is higher in this configuration [44]. The wavelength shift and the maximum intensity of the reflectance as a function of the tilting angle show as increasing the angle, a progressive blue shift occurs from 469 ± 1 nm at 0° to 438 ± 1 nm at 50° together with the reflectance reduction from 53% to 26% (Figure 6.6b). Similar values have been previously measured and reported in literature [45].

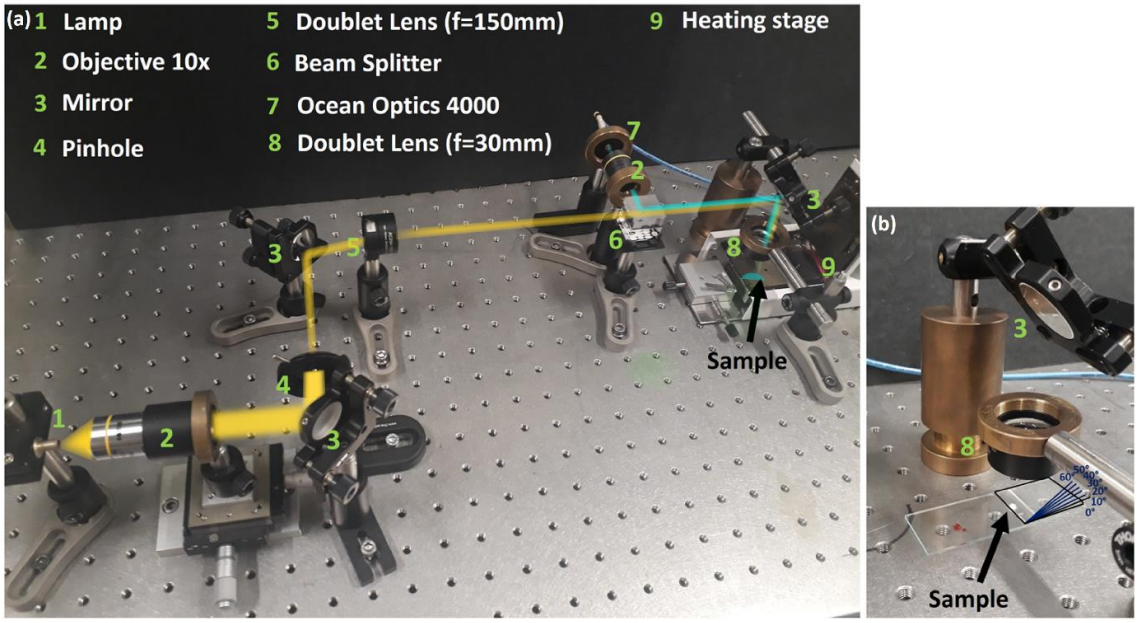

Figure 6.5. a) Experimental setup for spectroscopic measurements. b) Configuration used to measure the reflectance spectra of the butterfly wing at different angles: : different wedged platforms, made of two glasses forming angles from 0° to 50°, have been employed to tilt the sample surface.

As we aimed to make a thermo-responsive biotic-abiotic assembly, we first measured the reflectance of the pure butterfly wing as a function of temperature. The appearance of *Morpho* butterfly was monitored by an optical microscope (equipped with a 10x objective) in a temperature range from 30 °C to 160 °C (Figure 6.6.c).

We can suppose that the thermal expansion causes an increase in spacing between the ridges, an expansion of the lamellar structure and a thermally induced reduction in the refractive index of chitin [46]. It has been noticed that the contribution of the refractive index variation and expansion of the tree-like lamellar structure can be neglected [47], while the dominant effect should be attributed to the increasing spacing between the ridges. No significant color variation can be observed as it was confirmed by the reflectance spectra measured and reported in (Figure 6.6.d) that do not show a spectral shift (the lamellae separation remains unvaried) but only a reflectance efficiency decrease due to a constructive interference reduction.

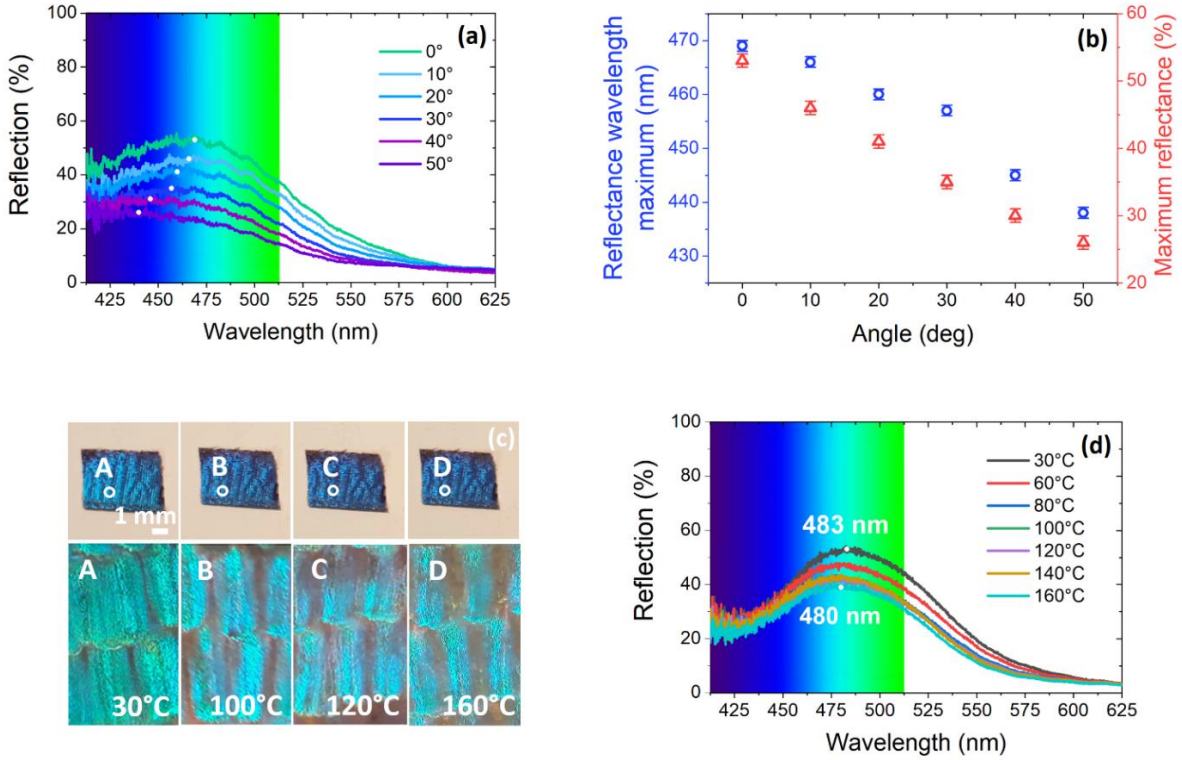

Figure 6.6. a) Reflectance spectra of the original flat wing tilted from 0° to 50° with step of 10°. b) Tilting angle dependence of the reflectance spectrum peak and its maximum intensity. c) *Morpho* butterfly appearance monitored by an optical microscope (equipped with a 10x objective) in a temperature range from 30 °C to 160 °C. No significant color variation can be observed. d) Reflectance spectra of a single point of the original wing changing the temperature from 30 °C to 160 °C.

To calculate the expected peak wavelength of the reflectance, we used a simple 1D optical calculation based on the configuration of multilayer-thin-film interference (Figure 6.4.b), obtaining the reflectance peak at 478 ± 18 nm. Such estimation has been compared with the experimentally measured reflectance whose maximum value is about 55% at 483 ± 1 nm. The peak wavelength corresponds to a vivid blue coloration. This maximal reflectance wavelength is not constant all over the entire wing, as every point has a slightly diverse geometry and therefore a spectral response whose maximum value is in the range of 460-500 nm. In Figure 6.7.a, we report the reflectance for another wing point whose peak is at 487 ± 1 nm. Moreover, also in this case, changing the sample temperature from 30 °C to 160 °C no evident color variation has been observed. In our sample, by exploring several different points on the entire wing, we measured a maximum reflectance variation of 18 nm, from 487 nm to 469 nm. Therefore, the position inaccuracy affects the spectrum measurement. However, after fixing the point under analysis,

the error of 1 nm has been evaluated as the maximum deviation from the mean value of the maximum reflectance wavelength of ten acquisitions. In our characterizations, we fixed the wing point under analysis and thus observed the induced color shift induced by the different effects. It is interesting to note in Figure 6.7.b that the reflectance wavelength maximum is highly sensitive to minute lamellae thickness variations: fixing the air spacing at 65 nm, a 10 nm lamella thickness increase leads to a pronounced spectrum red shift up to 503 nm showing as few nanometers can create a pronounced blue or a red shift of the reflectance maximum.

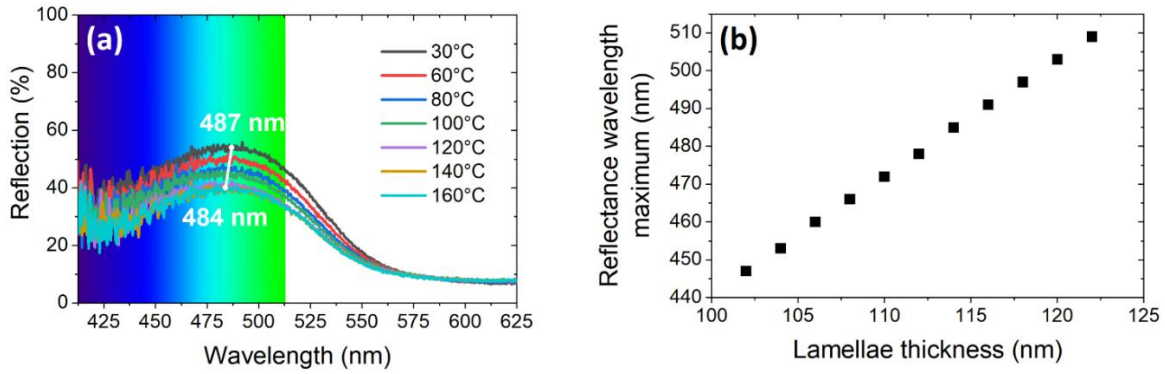

Figure 6.7. a) Reflectance spectra of a second point of the original wing changing the temperature from 30 °C to 160 °C. b) Reflectance wavelength maximum as a function of the lamellae thickness (h_1).

6.4 Artificial muscle of liquid crystal elastomer

To obtain a thermosensitive mechanical control on the wing properties, we used LCE artificial muscles [48] made by photopolymerization of a thiol-ene/acrylate formulation [45]. The molecular structures of all components are listed in Figure 6.8, which are similar to a formulation previously described [46], but slightly different in spacer lengths of LC monomers. The mixture contains LC monomer (C4, synthesized from the group of chemists at Chimie ParisTech), chain extender (EDDET™) and LC cross-linker (RM82™) in a molar ratio of 1:1:0.4. The initiator Irgacure 369™ was added in 2wt%. The molecular formulation has been optimized by the group of Prof. Li at ParisTech. Triggered by the UV light trigger, radical thiol-ene reaction is initiated for polymerization and cross-linking of C4/RM82™ and EDDET™. RM82™ is usually called cross-linker [49, 50], because in the

absence of RM82™, only linear polymers but not elastomers are obtained [49]. RM82™ can undergo both the thiol-ene reaction and polyacrylate-type homopolymerization, which result in the networking. The synthetic details of aligned LCE preparation are described in ref. [48].

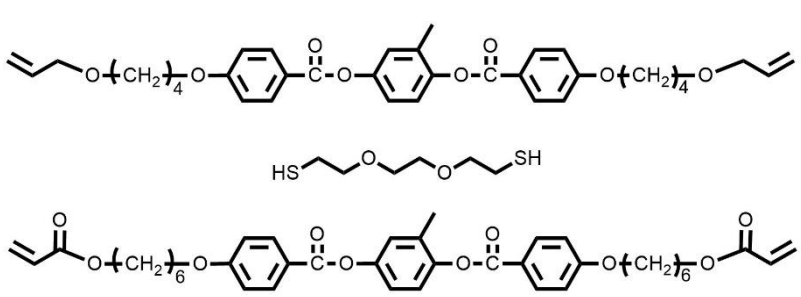

Figure 6.8. The molecular structures of main components in the LC mixtures for LCEs preparation. The mixture contains LC monomer (C4), chain-extender (EDDET™) and LC cross-linker (RM82™) in a molar ratio of 1:1:0.4.

Note that to get enough mechanical actuation, LCE muscles of 160 µm and 1 mm thickness were prepared and the detailed process is described in ref. [48] and in the next paragraph.

6.4.1 Fabrication procedure of the LCE film

A soft poly(dimethylsiloxane) PDMS mold was prepared employing optical microscope glasses with a thickness of 160 µm and 1 mm respectively, cut according to the desired pattern and covered with the liquid polymer (PDMS, Sylgard 184) (see (1) of Figure 6.9). PDMS mold was prepared using a 10:1 ratio of the elastomer base and the curing agent. Bubbles inside PDMS mixture have been removed by a vacuum pump, and subsequently, the sample has been heated at 70 °C for two hours (see (2) of Figure 6.9) for the thermal crosslinking/curing. After peeling (see (3) of Figure 6.9), the mold was used to fabricate the macroscopic cell: a glass from one side and the soft PDMS mold on the other side. The LCE mixture with photoinitiator Irgacure 369™ was heated to the isotropic phase (110 °C) and filled

in the rectangular mold made of PDMS, see (4) of Figure 6.9). The cell was then placed between two permanent NdFeB magnets (size: 20 mm x 20 mm x 10 mm, strength: approx. 118 N), fixed at a distance of 2 cm. The LCE mixture was later cooled down until room temperature at a slow rate (-1 °C/minute) (see (5) of Figure 6.9) to favor the nematic alignment. During the cooling process, the magnetic field aligns the mesogens along the direction of the magnetic field for a spatially homogeneous nematic phase. The cell was kept for one hour at room temperature in an oxygen-free environment by placing the alignment setup in a zip-lock bag flushed with a slow stream of argon to prevent oxygen radical inhibition during UV polymerization. It is then removed from the magnetic set up and an UV light source (30 mW/cm^2) was used to initiate the LCE photo-polymerization for 120 minutes (see (6) of Figure 6.9). The LCE film was obtained after removing the PDMS mold from one side (see (7) of Figure 6.9) and the glass from the other side (see (8) of Figure 6.9).

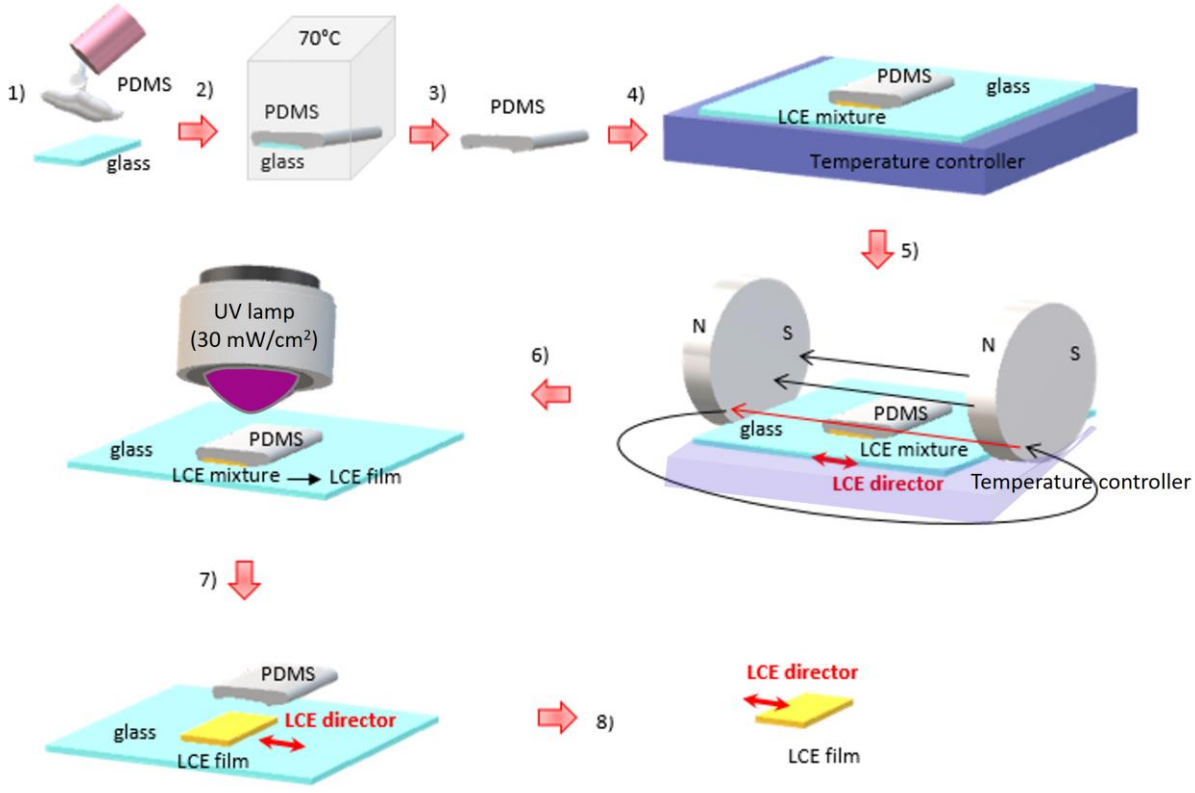

Figure 6.9. LCE film fabrication procedure.

Typically, the obtained LCE exhibits a contraction of 50% along the director when heating from 30 °C to 150 °C with a steep contraction around nematic to isotropic phase transition (T_{NI} = 120 °C) as shown in Figure 6.10.

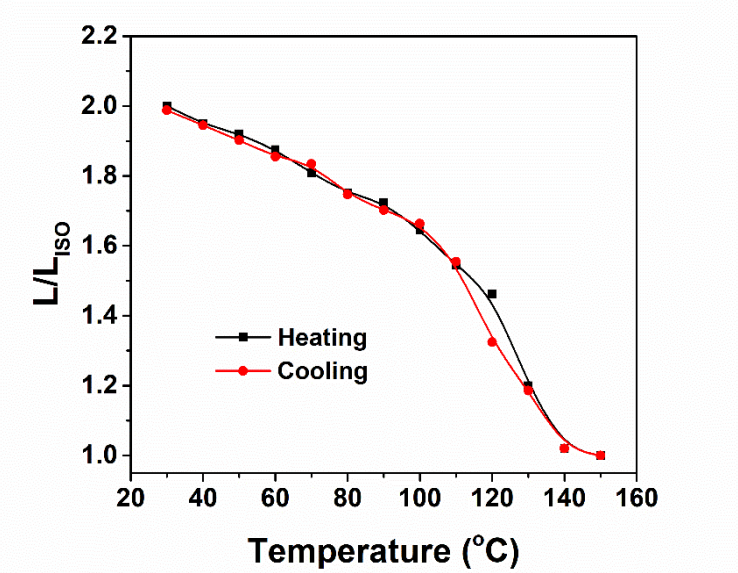

Figure 6.10. The contraction and relaxation length variation normalized to the dimension in the isotropic phase (L/L_{iso}) measured along director of the LCE film in heating and cooling process. L is the sample length at temperature T, L_{iso} is the sample length in the isotropic phase at T = 150 °C. The LCE film thickness is 160 µm. The same deformation was measured for the millimetric thick film as the molecular composition, alignment procedure and polymerization process are unvaried for the infiltrated LCE layer of 160 µm and 1 mm.

6.5 Biotic-abiotic hybrid system made by *Morpho Menelaus* butterfly and LCE artificial muscle

6.5.1 LCE film integration in *Morpho Menelaus* wing

A piece of the butterfly wing is cut with a blade, and a small amount of LC monomeric mixture (used as glue for the bilayer assembly) heated at 100 °C is gently placed on the back side of the wing. LCE film is placed on the LC monomeric mixture, which is then photopolymerized at room temperature for 60 minutes. This process is to ensure the adhesion of the LCE film to the back of butterfly wing. Both LCE films with a thickness of 160 µm (Figure 6.11.a) and 1 mm (Figure 6.11.b) were fabricated and then integrated on the back of the wing. The LCE film with a thickness of 1 mm allows for a more efficient and symmetric control of the structure deformation with respect to the thinner film of 160 µm as demonstrated in Figure 6.11 and therefore it has been selected to develop the structural color tuning experiments.

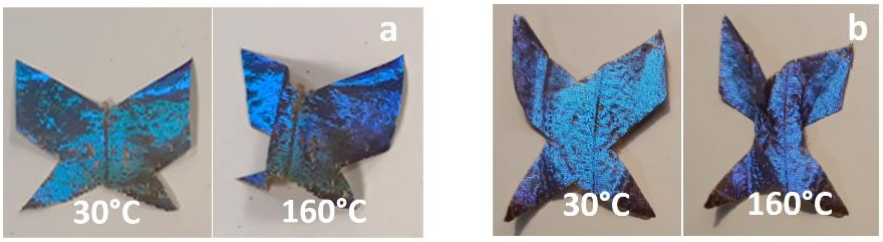

Figure 6.11. Hybrid systems with LCE films of different thickness e (a) $e = 160$ µm (b) $e = 1$ mm, integrated on the back of the wing. When heating from 30 °C to 160 °C, the structural deformation is more controlled and symmetric using the thicker film actuator (b).

The piece of LCE muscle with a thickness of 1 mm, as shown in Figure 6.12.a is then glued on the back of a piece of wing cut in a cross shape (Figure 6.12.b) or a rectangular shape (Figure 6.12.c).

Once integrated on the back of the wing, the contraction of a small piece of the LCE induces a mechanical stress on the butterfly wing (whose surface area is larger than the actuator one) (Figure 6.12.c). In response to different temperatures, a gradual shape change of the film is obtained leading to the angular control of the butterfly wing flapping (Figure 6.12.d). While at room temperature the wing lays flat over the elastomeric actuator, increasing the temperature, it bends up to 30° once the film is heated at 120 °C. The sample has been recycled for several times under temperature cycles before its damage. If the reflectance of the bent part of the wing is monitored, a blue shift of 15 nm is observed, and the value of the reflectance reduces by 18% (Figure 6.12.e-f). Comparing such values with the ones obtained by the angular measurement for the *Morpho* butterfly wing without the LCE actuator (see Figure 6.6.b), as reported in Figure 6.12.f, allows us to explain the spectral shift as a change in coloration induced by the butterfly iridescence at different bending angles. The slightly different value of the spectral shift can be attributed to an inaccuracy in the angle measurement and a not perfect flat bending of the wing.

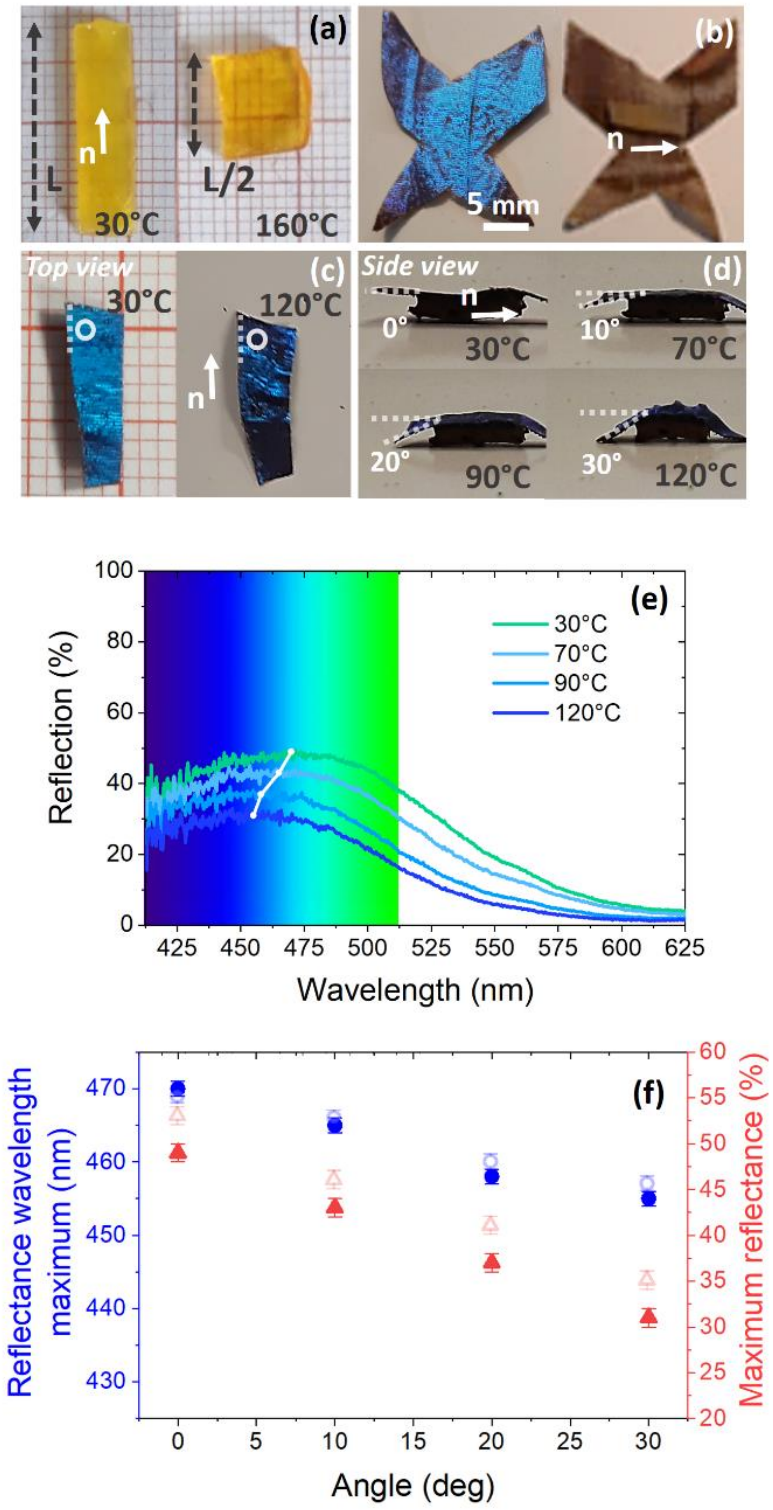

Figure 6.12. a) LCE film with a thickness of 1 mm at 30 °C and at 160 °C. The slight opacity of the LCE film is because of the rather high thickness of the film (1 mm) and the non-perfect monodomain alignment, which however do not affect the big deformation of the sample. A small piece of the film was cut to be integrated underneath the ventral (back) side of the butterfly. b) LCE film

integration on the back side of a cross shape wing. c) and d) LCE film integration on the back side of a rectangular shape wing, with top view (c) of hybrid system's contraction and color change, and side view (d) of hybrid system's bending upon heating from 30 °C to 120 °C. e) Reflectance spectra of the hybrid rectangular shape wing as a function of temperature. The reflection is collected from the end part of the wing stripe that shows a bending of 0°, 10°, 20° and 30°, at 30 °C, 70 °C, 90 °C and 120 °C respectively. f) Reflectance wavelength maximum and maximum reflectance intensity of the hybrid rectangular shape wing as a function of the bending angle. Empty markers refer to the corresponding values for the original butterfly tilted at different angles.

The hierarchical micro/nano structuration of the scales also generates a superhydrophobic platform. The thermal control of the angular bending of the butterfly piece induces not only a blue shift of the color surface but also a self-cleaning effect (Figure 6.13.a), which is independent of the cut wing shape. The drop contact angle variation in forward and backward direction relative to the system is shown in Figure 6.13.a-b as a function of the increasing temperature up to 160 °C. At room temperature, a small difference between the advancing and receding angles (low contact angle hysteresis defined as the rose petal effect) does not perturb the droplet position, while increasing such difference by raising up the temperature up to 80 °C the drops start to roll out along the ridges until it slides out of the butterfly.

In Figure 6.13.c, two different glycerol drops (A and B), placed on the cross shape wing, exhibit anisotropy in the sliding direction [51]. Indeed, a droplet easily rolls along the radial outward (RO) direction (denoted by the arrow in the SEM image of Figure 6.13.d) but is tightly pinned in the orthogonal direction (perpendicular to the scale vanes) [51]. The macroscopic LCE contraction induces the droplet A sliding along the parallel groove microstructures, while induces droplet B moving along the direction perpendicular to RO. Therefore, droplet A easily rolls along the RO direction while droplet B remains pinned in the orthogonal direction. A SEM magnification of a cover scale detail is reported in Figure 6.13.d highlighting the radial outward direction.

This self-cleaning effect is independent of the cut wing shape. Figure 6.14 shows as in response to different temperatures, a gradual shape change of the rectangular wing induces the sliding of a glycerol drop on its surface.

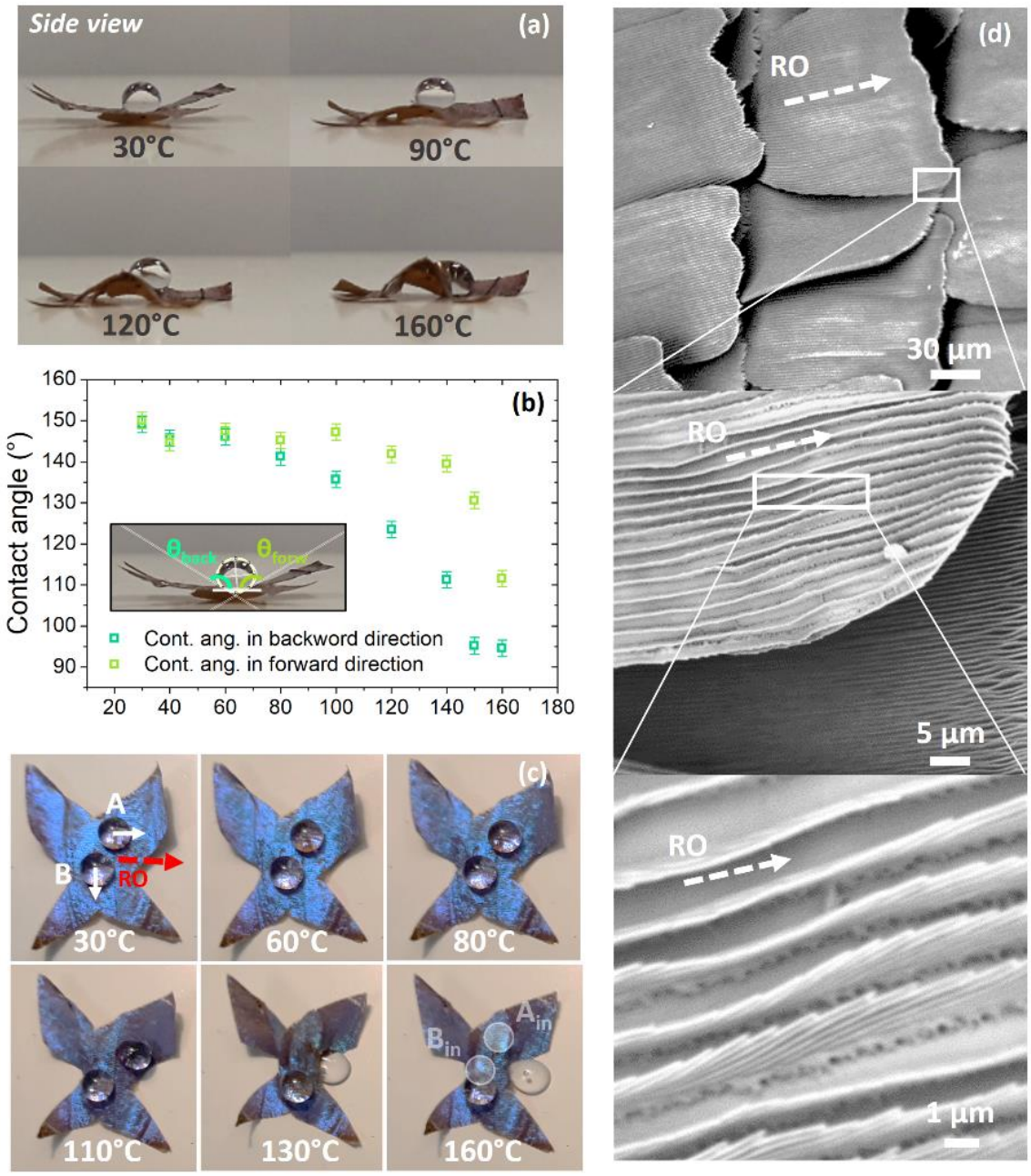

Figure 6.13. a) Side view of a glycerol drop sliding along the longitudinal vanes direction when the hybrid cross-shape wing is activated and deformed by heat. b) Contact angle variation in backward and forward direction (advancing and receding contact angle measurement) of the glycerol drop as a function of temperature. c) Movement of drop A and drop B during the butterfly deformation at different temperatures. Drop A slides out of the wing because it is rolling along the vanes direction. The initial positions of the droplets (A_{in} and B_{in}) are marked for reference in the image taken at 160 °C. d) SEM images of cover scales for

different magnifications. The arrow in the SEM images denotes the radial outward (RO) direction along which a drop slides easily.

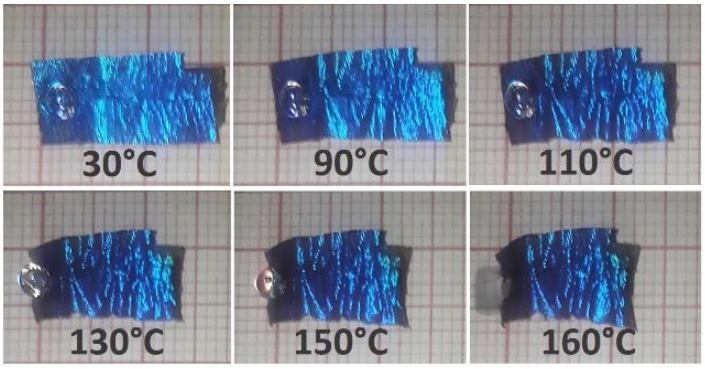

Figure 6.14. Glycerol drop sliding on a rectangular shape wing.

6.5.2 LCE layer infiltrated in *Morpho Menelaus* blue butterfly wing

In order to improve the coupling between the two components and the protocol reproducibility, direct infiltration of the mixture of LC molecules on the back side of the wings was evaluated.

The LC monomeric mixture is placed at 100 °C on the uncolored back side of a wing stripe and diffuses along the ridges by capillary forces creating a thin layer of less than a few microns. The ventral wing membrane where scales are inserted into sockets (see SEM image in Figure 6.15) further prevents the LC monomeric mixture infiltration among the scales of the dorsal upper side. In such a way, we obtained a quite homogenous film that covers the brown and jagged scales of the ventral side of the wing without affecting the natural photonic structure (present on the upper surface).

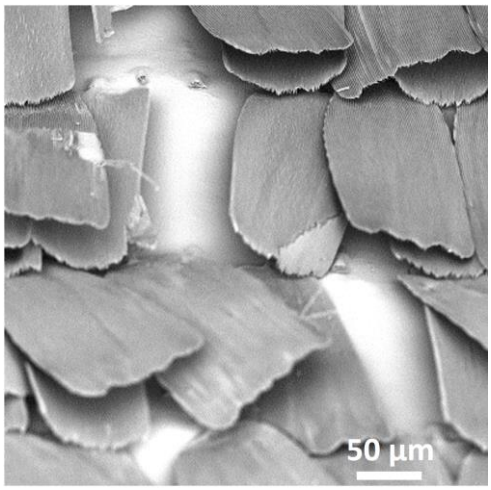

Figure 6.15. Wing membrane seen from the upper side, where cover and ground scales are inserted into sockets.

The LC monomeric mixture has been first homogeneously aligned along the direction perpendicular to the scale length and vanes direction by two magnets, and cooled until room temperature with a slow temperature ramp (-1 °C/minute) to align the LC molecules. The whole setup was placed in an oxygen-free environment flushed with a slow stream of argon to proceed the polymerization/crosslinking under UV light (30 mW/cm^2 for 60 minutes) [48, 52, 53].

Figure 6.16.a reports the optical image of the back of the hybrid sample (piece of wing with infiltrated LCE) in which the director **n** indicates the direction of the molecular alignment. The good homogeneity of the final LCE layer can been observed in the SEM images (Figure 6.16.b) with different magnifications, while the LCE alignment has been verified by a polarized optical microscope (POM images are shown in Figure 6.16.c, where the transmittance extinction is observed for sample rotation of 45°, while in case of the untreated original butterfly no color intensity variation was observed).

Looking at the microscope images of each single ground scale in Figure 6.16.d, the untreated wing, reported on the left panels, has no scale deformation increasing temperature up to 160 °C. In the same temperature range instead, the hybrid LCE infiltrated system at 30 °C (on the top right) shows a 10% width scale contraction due to an initial strain induced by the polymerization of the LC monomeric mixture, and the increase of temperature up to 160 °C leads to a further size reduction of 15% (on the bottom right). The underlying LCE layer induces a slightly curved shape at the stripe edges at room temperature, that is lost at 80 °C when the system flattens out (Figure 6.16.e' (top view) and Figure 6.16.e'' (side view). This effect is absent in the untreated butterfly that shows a negligible bending behavior when it is heated as no external stress is present. The bi-layered system returns in a reversible way to its initial shape in 70 seconds when room temperature is restored (Figure 6.16.e'''). In order to investigate the LCE role, we measured the reflectance spectra of the flat part of the sample (Figure 6.16.f), indicated with a light blue circle in Figure 6.16.e', for different values of temperature in between 30 °C and 160 °C, reporting also the wavelength of the reflectance peak and the maximum reflectance as a function of temperature in Figure 6.16.g. The sample has been recycled for several times under temperature cycles before its damage.

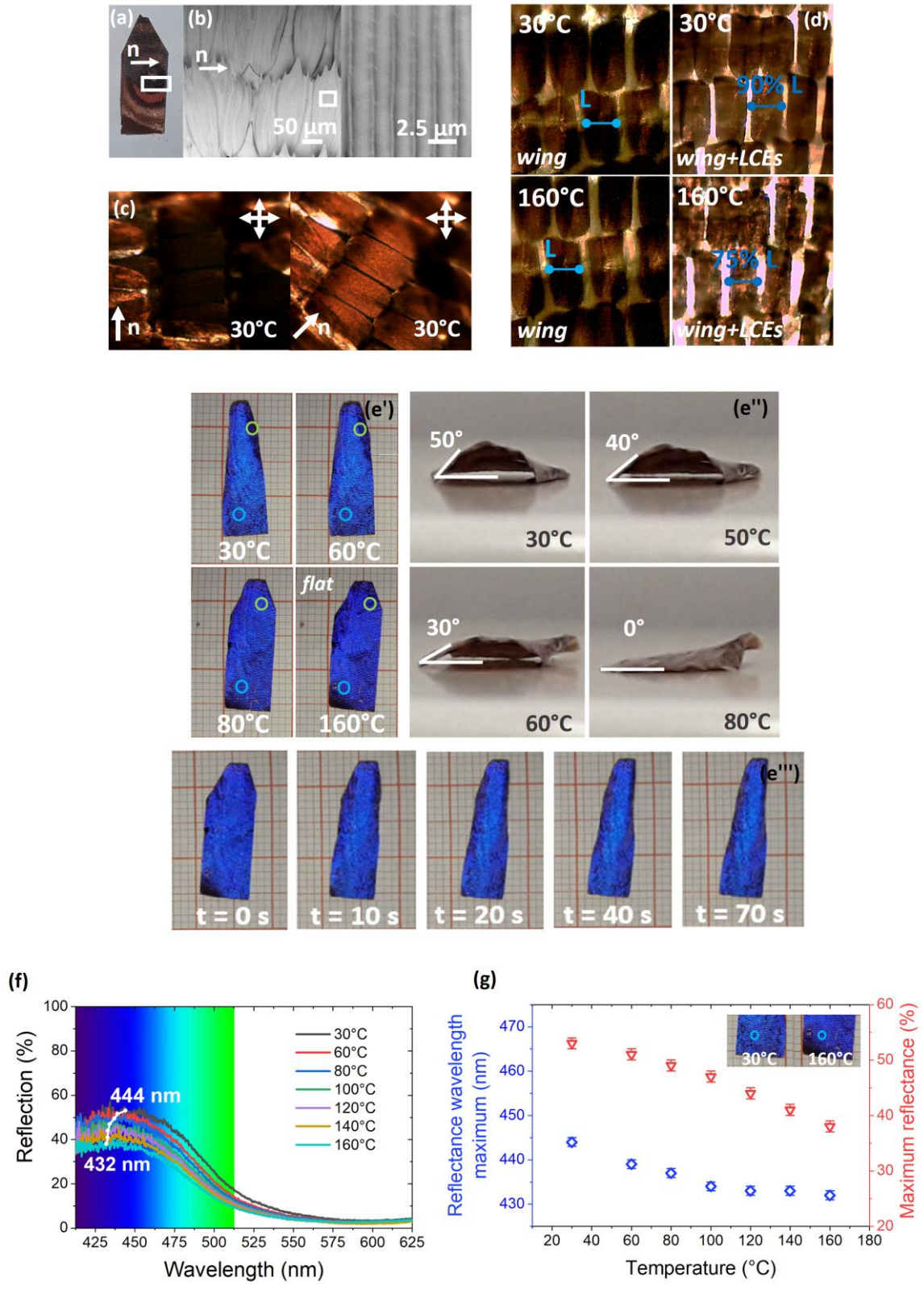

Figure 6.16. a) Optical image of the back side of the wing with infiltrated LCE after UV polymerization. The nematic director is indicated by the vector, **n**. b) Scanning electron microscope images of the LCE layer. c) Polarized optical microscope images of the untreated butterfly wing (two images on the top) and of

the wing with infiltrated LCE on its back side (two images on the bottom). Cross arrows represent directions of polarizer and analyzer. d) Optical images of the untreated butterfly (two images on the left) and the wing with infiltrated LCEs (two images on the right) at 30 °C and at 160 °C. In the first case, no deformation of the ground scales has been observed. In the second case, a 10% deformation has been observed after the polymerization of LC monomeric mixture and a further 15% contraction has been measured when heated to 160 °C. e') The hybrid system has a convex curled shape at room temperature and reaches a flat shape, with the increase of temperature, due to the LCE layer strain and deformation. e'') Curved part of the hybrid stripe that shows a bending of 50°, 40°, 30° and 0°, at 30 °C, 50 °C, 60 °C and 80 °C respectively. e''') Shape recovering of the hybrid system when room temperature is restored. f) Reflectance spectra of the hybrid structure at different temperatures. The reflection is collected from the flat part of the wing stripe. g) Reflectance wavelength maximum and maximum reflectance intensity as a function of temperature collected from flat part of the butterfly wing (shown in the inset at 30 °C and 160 °C).

The slight deformation variations of the different points of the wing can be attributed to some inhomogeneities of the LCE film thickness. Figure 6.17.a shows a SEM image where both membrane and jagged scales of the ventral wing side are covered with a homogenous LCE layer. The polymer layer thickness looks constant all over areas of several millimeters. Few regions with some defects (at the scale level) have been observed using SEM (Figure 6.17.b), which could slightly affect the deformation of the different points of the wing.

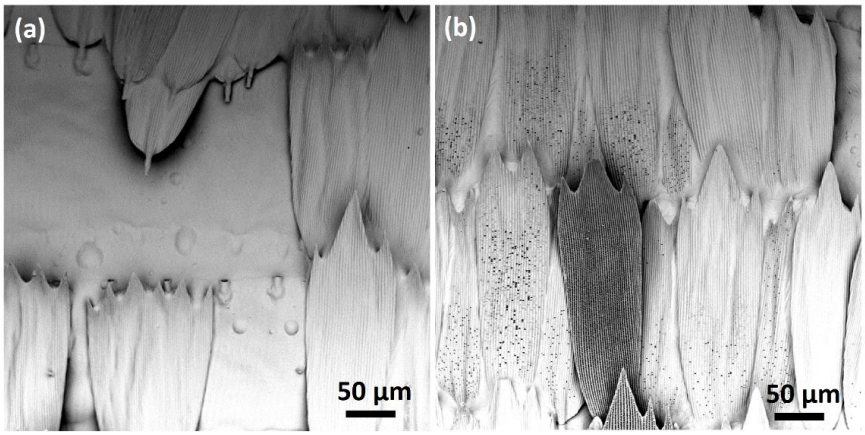

Figure 6.17. a) LCE layer covers the wing membrane (seen from the ventral side) and the jagged scales. b) Scale infiltration defect on the ventral side of the butterfly wing.

During the thermal actuation, the monitored part remains flat meaning that the contribution to the reflectance shift cannot be attributed to the iridescence of the sample. At room temperature, the LCE stress reflects in a blue shift of 39 nm with respect to the untreated butterfly wing reflectance. Increasing the temperature above 100 °C, the lateral contraction of each single scale modifies the nanostructured ridges inducing a wavelength shift of 12 nm. A total shift of 51 nm with respect to the untreated butterfly has been thus obtained. This color tuning can be attributed not only to the ridge distance variation but also to a tilting and/or bending of the ridges due to the LCEs strain. Such phenomena resulted in the decrease of the air separation between the lamellae and thus in a different interference effect of the stack. To explore the different contribution of the geometrical parameter of the periodic ridges, we performed reflectance calculation of the periodic tree structure using a MATLAB code for periodic patterned multilayers based on Rigorous Coupled Wave Analysis (RCWA) [54-56]. The periodic unit cell represents the tree structured ridge with the geometrical dimensions measured in the SEM images of Figure 6.4.

The reflection spectrum has been calculated and reported in Figure 6.18.a considering the case of a 10 lamellae stack using a simplified model based on multilayer interference effect, in which the lamellae are considered perfectly parallel to the membrane substrate and symmetrically distributed with respect to the ridge trunk (see the inset in Figure 6.18.a). The calculation results show a reflection peak at around 480 nm (blue color), greatly reproducing the experimentally measured reflectance, and other two weak picks at about 420 nm and 560 nm. Monitoring the squared electric field distribution within each ridge at 400 nm, 480 nm and 600 nm (Figure 6.18.b), we could better understand the photonic properties of the butterfly. At 400 nm, the lamellar structure determines a not optimized reflection and a relatively weak transmission through the tree-like structure with a weak cavity effect within each ridge. At the reflectance maximum, the periodic structure behaves as an effective Bragg reflector explaining the strong reflection peak in the blue spectral range. Increasing the wavelength up to 600 nm, the nanometric periodicity does not affect anymore the light propagation that is mostly transmitted across the scale leading to a negligible reflectance.

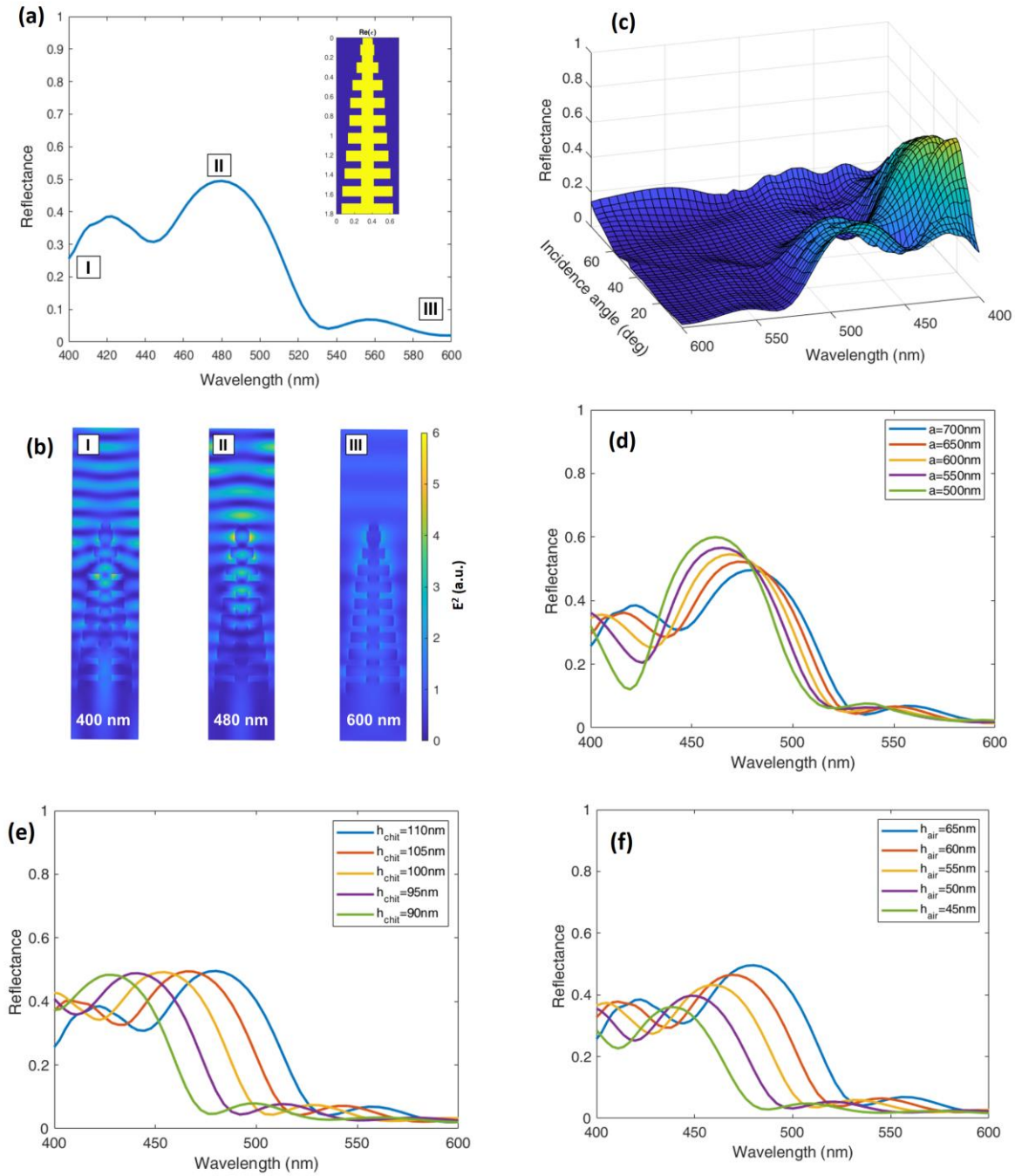

Figure 6.18. a) Calculation of the reflectance spectrum from the tree-like structure of the scale ridges with 10 lamellae layers. In the inset, the periodic unit cell of the RCWA calculation is reported. b) Squared electric field spatial distribution for three different wavelengths: 400 nm, 480 nm and 600 nm. c) Reflectance dependence on the angular direction of the incident wave. The incident angle is calculated with respect to the normal to the scale surface. d) Calculation of the reflectance spectra varying "a": the distance between the ridge from 700 nm to 500 nm with a step of 50 nm. e) Calculation of the reflectance spectra varying the chitin lamellae thickness from 110 nm to 90 nm with a step of

5 nm. f) Calculations of reflectance spectrum varying the thickness of the air layer between the lamellae.

As expected for Bragg reflectors, increasing the angle of incidence of the plane wave with respect to the normal to the surface, a blue shift of the reflectance occurs as reported in the reflectance map as a function of the light incidence angle in Figure 6.18.c. Focusing on the contribute of the scale parameter variation while actuating the infiltrated LCE layer, we calculated the reflectance spectra singularly varying the pitch of the ridges, the thickness of the lamellae and their interspacing. Interestingly, a reduction of the ridge separation (Figure 6.18.d) induces a blue shift of the spectra and a more pronounced reflection intensity, probably due to an effective refractive index increase and interference effect. Contrary to previously reported assumption [15], we exclude that both the experimental initial shift of 39 nm and the minor shift of 12 nm could be attributed to the lamellae contraction, as in this case an effective blue shift will be expected without an intensity reflectance variation, as demonstrated in the calculation of Figure 6.18.e. We rather suppose that the LCEs strain and activation generate both a gradual approach of the vanes together with a slight deformation of each single ridge. Looking at Figure 6.18.f, reporting the reflectance spectra calculated when the air layer thickness changed from 65 nm to 45 nm, a blue shift of about 50 nm with an intensity decrease from 50% to 38% is observed. This result is in full agreement with the experimental measurements shown in Figure 6.16.f, and indicates that the color tuning is mostly determined by the variation of the air space between chitin lamellae.

To estimate the contribution of the ridge separation variation and iridescence, we measured the reflectance spectra of the bent edges of the assembled wing stripe (indicated by the light green circle in Figure 6.16.e'), as a function of temperature. Such information is immediately clear looking at the reflectance spectra in Figure 6.19.a and the maximum peak of every reflective spectrum and the intensity as a function of temperature is reported in Figure 6.19.b.

At room temperature, at the stripe corners, the wing has a curved shape forming an angle of 50° that generates a reflectance peak at 437 ± 1 nm (Figure 6.19.b) with a reflectance of the 24%. Such values are in good agreement with the reflectance of the wing measured in case of a rigid angular tilting of 50° (Figure 6.6.a-b). Increasing the temperature up to 50 °C, in which the bent wing forms an angle of 30° with respect the sample plane, the maximum peak shifts at

455 ± 1 nm, which can be compared with the value of 458 ± 1 nm measured in case of 30° rigid angular rotation of the butterfly wing. At 80 °C the wings becomes completely flat, releasing the induced stress of the photopolymerized layer and well reproducing the reflectance spectrum of the flat part of the wing measured at 80 °C. Above this temperature, the contraction of the LCE polymerized layer induces a further wavelength shift of 5 nm from 438 ± 1 nm at 80 °C to 433 ± 1 nm at 160 °C due to scale shrinkage. It is interesting to notice how within the temperature range from 30 °C - 60 °C, the different coloration is determined by the iridescence of the wing, while above 80 °C when the stripe recovers the flat shape, and the further shift of 5 nm is generated from the structural color tuning.

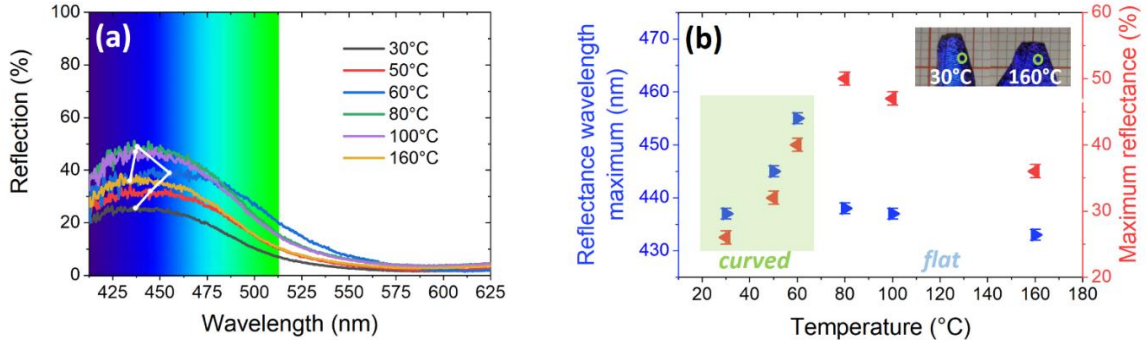

Figure 6.19. a) Reflectance spectra of the hybrid structure for different temperatures. The reflection is collected from the curved part of the wing stripe. b) Wavelength dependence of the reflectance peak and the maximum reflectance intensity as a function of temperature in case of the curved part of the wing (shown in the inset at 30 °C and 160 °C).

6.6 Towards butterfly wing replicated in PDMS and LCE

6.6.1 Negative PDMS mold of butterfly wing

The fabrication of a negative PDMS mold reproducing the multi-layered scales of the *Morpho* butterfly wing is here reported. The positive replica was made infiltrating the PDMS mold by Liquid Crystalline Elastomers.

A piece of the butterfly wing was cut by a blade and glued on a microscope glass. In order to easily separate the wing from the negative PDMS mold, it was necessary to decrease the stickiness of the wing. Therefore, the sample surface was treated overnight in a solution of toluene and several drops of $CF_3(CF_2)_5CH_2CH_2SiCl_3$. After that, the wing was covered with the liquid PDMS

resin (PDMS-Sylgard 184) with the elastomer base to the curing agent ratio of 10:1. Bubbles inside PDMS mixture were removed by a vacuum pump for half hour. The sample was then heated at 70 °C for two hours. After peeling, several scales remained attached to the PDMS mold (Figure 6.20.a), but the butterfly wing was completely removed and replicated on the PDMS mold in areas of several millimetres.

Optical microscope images of the PDMS mold are reported in Figure 6.20.a-d showing scales' detail replicated in the PDMS mold that are characterized by linear grooves, that reproduce the ridges of butterfly wing.

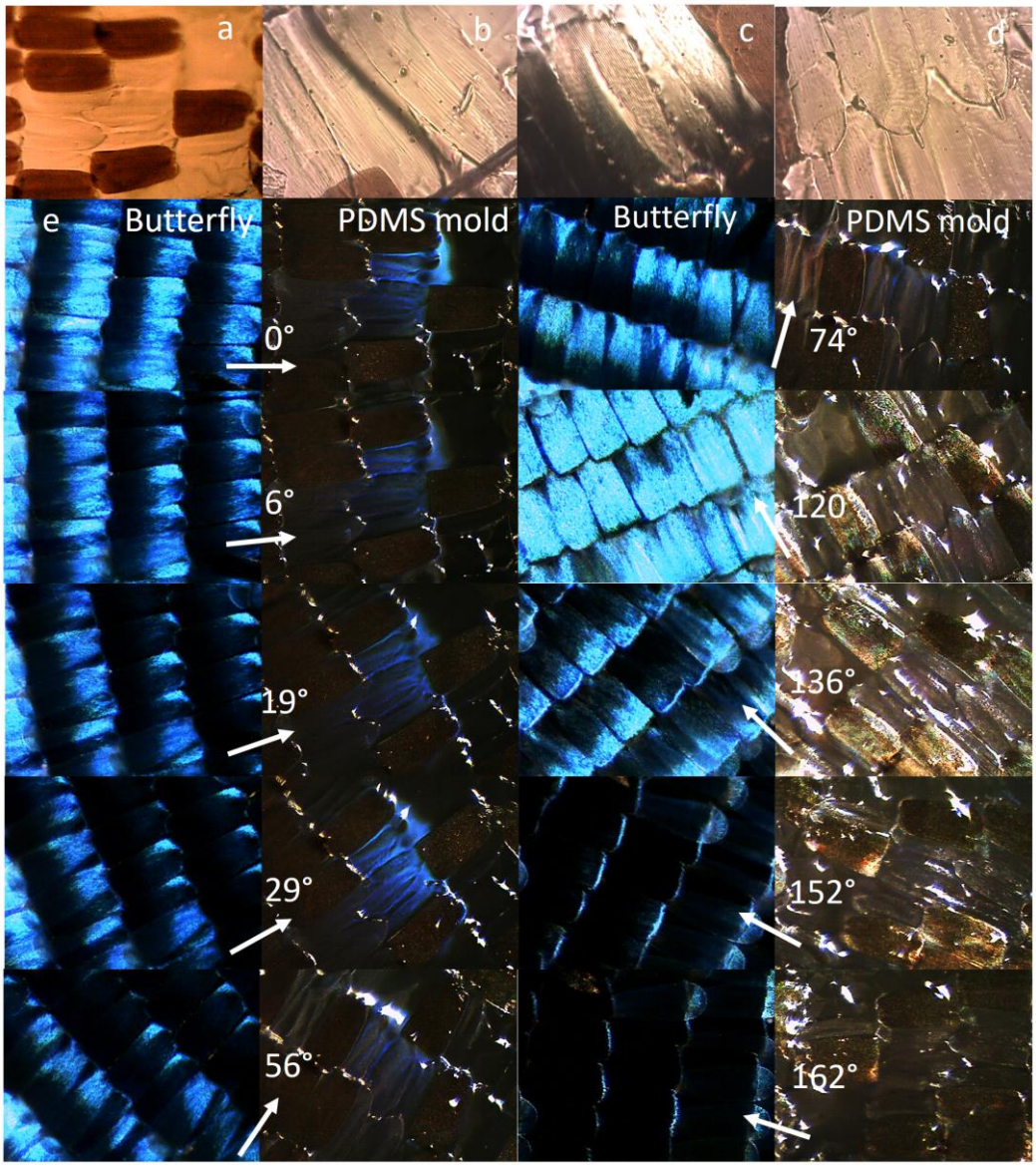

Figure 6.20. a-d) Optical images of the PDMS negative mold. e) Images of *Morpho Menelaus* butterfly wings and PDMS replica for different angles for an in-plane rotation with white light illumination fixed a 45° with respect to the wing normal.

The negative PDMS replica demonstrated iridescence property. In fact, looking from above and illuminating with white light at 45° with respect to PDMS mold normal, an in-plane rotation (in the mold plane) shows that the reflectance depends on the orientation of the scale with respect to the illumination direction. A comparison with the rotation of the real iridescence butterfly wing is also reported in Figure 6.20.e.

6.6.2 Positive LCE replica of butterfly wing

After the realization of the negative PDMS mold, which partially reproduced the micro structures of the wing, the mold was infiltrated by LCE mixture and heated up to the isotropic phase (100 °C). The sample was then placed between two permanent magnets and cooled down until room temperature at a slow rate (-1 °C/minute) in an oxygen-free environment (using a zip-lock bag flushed with a slow stream of argon). The sample was maintained at room temperature for one hour in the nematic phase and after removing it from the magnetic set up, an UV light source (30 mW/cm^2) was used to initiate the photo-polymerization for 60 minutes. The PDMS mold was removed while LCE replica remained attached on glass.

The LCE nematic alignment was verified by a polarized optical microscope. POM images are shown in Figure 6.21 where the transmittance extinction is observed for sample director orientation parallel to the polarizer axis.

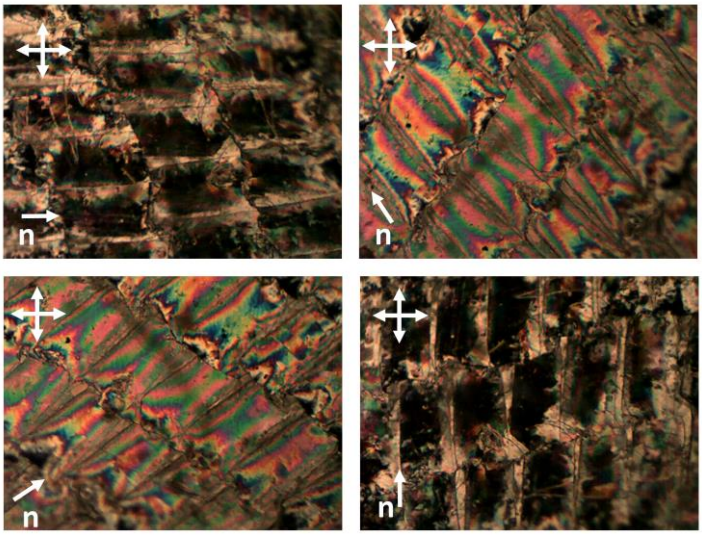

Figure 6.21. Polarized optical microscope images of the LCE replica of the butterfly wing. The director direction is indicated with **n**, while the two arrows represent the polarization axis of the crossed polarizers.

In order to better understand the colors that appear when the LCE sample is observed under POM, while it is rotated at 45° with respect to the two polarizers direction, some theoretical considerations have been reported in Appendix A.

6.6.3 Effects of interference in LCE butterfly wing replica

The LCE butterfly wing replica has been heated from 30 °C to 100 °C with a step of 10 °C. POM images are reported in Figure 6.22.

Figure 6.22. LCE scales are heated from room temperature until 100 °C showing color interference variations at POM. Decreasing the temperature until 30 °C, the sample recovers the same colors and therefore the initial birefringence.

Color changes due to interference effects, described in Appendix A, have been observed for birefringence variation. If we assume an average birefringence value, typical for LCEs, of 0.12 from Michel-Lévy chart (see Appendix A), we can deduce that LCE sample should have a thickness of about 15 µm (green color) at room temperature. After LCE activation at about 60 °C, the sample undergoes a variation of its thickness. We could estimate a value of about 17.5 µm (yellow color) and a birefringence of 0.08 at 100 °C. Such shape changing (of 16%) retrieved from birefringence variations is perfectly compatible with the expected expansion of the dimensions perpendicular to the director. By lowering down temperature, we observed the reversed color changes, with a recovery of the initial birefringence at room temperature.

References

[1] Q. Li, Q. Zeng, L. Shi, X. Zhang and K.-Q. Zhang, J. Mater. Chem. C 2016, 4, 1752-1763.

[2] K. Chung, S. Yu, C.-J. Heo, J. W. Shim, S.-M. Yang, M. G. Han, H.-S. Lee, Y. Jin, S. Y. Lee, N.Park, J. H. Shin, Adv. Mater. 2012, 24, 2375-2379.

[3] Q. Shen, J. He, M. Ni, C. Song, L. Zhou, H. Hu, R. Zhang, Z. Luo, G. Wang, P. Tao, Small 2015, 11, 5705.

[4] S. Kinoshita, S. Yoshioka and K. Kawagoe, Proc. R. Soc. Lond. B 2002, 269, 1417-1421.

[5] S. Kinoshita, S. Yoshioka and J. Miyazaki, Rep. Prog. Phys. 2008, 71, 076401.

[6] M. A. Giraldo, S. Yoshioka, C. Liu and D. G. Stavenga, J. Exp.l Biol. 2016, 219, 3936-3944.

[7] S. Kinoshita and S. Yoshioka, ChemPhysChem 2005, 6, 1442-1459.

[8] P. J. Vernon, Y. Fang, Y. Cai, K. H. Sandhage, Angew. Chem. Int. Ed. 2010, 49, 7765-7768.

[9] S.-H. Kang, T.-Y. Tai, T.-H. Fang, Curr. Appl. Phys. 2010, 10, 625-630.

[10] H. Butt, A. K. Yetisen, D. Mistry, S. A. Khan, M. U. Hassan, S. H. Yun, Adv. Opt. Mater. 2016, 4, 497-504.

[11] R. E. Rodríguez, S. P. Agarwal, S. An, E. Kazyak, D. Das, W. Shang, R. Skye, T. Deng, and N. P. Dasgupta, ACS Appl. Mater. Interfaces 2018, 10, 4614-4621.

[12] S.-H. Kang, T.-Y. Tai, T.-H. Fa, Curr. App. Phys. 2010, 10, 625-630.

[13] S. Zhang, Y. Chen, Sci. Rep. 2015, 5, 16637.

[14] G. Zyla1, A. Kovalev, E. L. Gurevich, C. Esen, Y. Liu, Y. Lu, S. Gorb, A. Ostendorf, Appl. Phys. A, 2020, 126, 740.

[15] R. A. Potyrailo, R. K. Bonam, J. G. Hartley, T. A. Starkey, P. Vukusic, M. Vasudev, T. Bunning, R. R. Naik, Z. Tang, M. A. Palacios, M. Larsen, L. A. Le Tarte, J. C. Grande, S. Zhong & T. Deng , Nat. Comm. 2015, 6, 7959.

[16] R. H. Siddique, A. Faisala, R. Hnigb, C. Bartelsc, I. Wackerc, U. Lemmerb and H. Hölscher, Proc. of SPIE 2014, 9187, 91870E-1.

[17] X. Qing, Y. Liu, J. Wei, R. Zheng, C. Zhu, and Y. Yu, Adv. Optical Mater. 2019, 7, 1801494.

[18] Z. Chen, F. Fu, Y. Yu, H. Wang, Y. Shang, and Y. Zhao, Adv. Mater. 2018, 1805431.

[19] M. E. Calvo, L. González-García, J. Parra-Barranco, A. Barranco, A. Jiméne-Solano, A. R. Gonzále-Elipe, H. Míguez, Adv. Optical Mater. 2015, 3, 2, 171-175.

[20] P.-G. de Gennes, P. G. C. R. Acad. Sci. Paris 1975, 281b, 101.

[21] P.-G. de Gennes, P. G. C. R. Acad. Sci. Paris IIB 1997, 324, 343.

[22] J. Küpfer, H. Finkelmann, Makromol. Chem., Rapid Commun. 1991, 12, 717.

[23] H. Wermter, H. Finkelmann, e-Polym. 2001, 013.

[24] M.-H. Li, P. Keller, Phil. Trans. A. 2006, 364, 2763-2777.

[25] T. Ikeda, J.-I. Mamiya, Y. Yu, Angew. Chem., Int. Ed. 2007, 46, 506-528.

[26] T. J. White; D. J. Broer, Nat. Mater. 2015, 14(11), 1087-1098.

[27] Y. Yu, T. Ikeda, Angew. Chem. Int. Ed. 2006, 45 (33), 5415.

[28] D. Martella, S. Nocentini, C. Parmeggiani, and D.S. Wiersma, Adv. Mater. Technol. 2019, 4, 1800571.

[29] H. Zeng, P. Wasylczyk, D.S. Wiersma, and A. Priimagi, Adv. Mater. 2018, 30, 1703554.

[30] A. H. Gelebart, M. Mc Bride, A. P. H. J. Schenning, C. N. Bowman, and D. J. Broer, Adv. Funct. Mater. 2016, 26, 5322-5327.

[31] S. Nocentini, D. Martella, C. Parmeggiani, D. S. Wiersma, Adv. Opt. Mater. 2019, 1900156.

[32] S. Nocentini, D. Martella, D.S. Wiersma and C. Parmeggiani, Soft Matter 2017, 13, 8590-8596.

[33] I. De Bellis, D. Martella, C. Parmeggiani, E. Pugliese, M. Locatelli, R. Meucci, D. S. Wiersma, S. Nocentini, J. Phys. Chem. C 2019, 123, 43, 26522-26527.

[34] S. Nocentini, D. Martella, C. Parmeggiani, S. Zanotto, D. S. Wiersma, Adv. Opt. Mater. 2018, 6, 15, 1800167.

[35] H. Xing, J. Li, Y. Shi, J. Guo, J. Wei, ACS Appl. Mater. Interfaces 2016, 8, 14, 9440-9445.

[36] M. H. Li, A. Brûlet, P. Davidson, P. Keller and J. P. Cotton, Phys. Rev. Lett., 1993, 70, 2297-2300.

[37] J. P. Cotton and F. Hardouin, Prog. Polym. Sci. 1997, 22, 795-828.

[38] D. J. Broer, J. Boven, G. N. Mol and G. Challa, Die Makromolekulare Chemie 1989, 190, 2255-2268.

[39] S: Yoshioka and S. Kinoshita, Proc. R. Soc. Lond. B 2004, 271, 581–587.

[40] R. H. Siddique, S. Vignolini, C. Bartels, I. Wacker & H. Hölscher, Sci. Rep. 2016, 6, 36204.

[41] S. Berthier, E. Charron, A. Da Silva, Opt. Comm. 2003, 228, 349-356.

[42] S. Berthier, E. Charron, and J. Bouleng, *Insect Sci.* **2006**, 13, 145-157.

[43] W. Wua, G. Liao, T. Shi, R. Malik, C. Zeng, Microelectronic Engineering 2012, 95, 42-48.

[44] S. Zobl, B. D. Wilts, W. Salvenmoser, P. Pölt, I. C. Gebeshuber and T. Schwerte, Biomimetics 2020, 5, 5.

[45] F. Liu, Y. Liu, L. Huang, X. Hu, B. Dong, W. Shi, Y. Xie, X. Ye, Opt. Comm. 2011, 284, 2376-2381.

[46] S. Niu, B. Li, Z. Mu, M. Yang, J. Zhang, Z. Han, L. Ren, J. Bionic Eng. 2015, 12, 170-189.

[47] A. D. Pris, Y. Utturkar, C. Surman, W. G. Morris, A. Vert, S. Zalyubovskiy1, T. Deng, H. T. Ghiradella and R. A. Potyrailo, Nat. Photonics 2012, 6.

[48] B. Ni, M. Zhang, C. Guyon, P. Keller, M. Tatoulian, and M.-H. Li, submitted to Mater. Chem. Front. on 16 April 2020.

[49] T. H. Ware, Z. P. Perry, C. M. Middleton, S. T. Iacon and T. J. White, ACS Macro Lett. 2015, 4, 9, 942-946.

[50] T. Hessberger, L. Braun, R. Zentel, Polymers 2016, 8, 410.

[51] Y. Zheng, X. Gao and L. Jiang, Soft Matter 2007, 3, 178-182.

[52] M.-H. Li, P. Keller, J.-Y. Yang, P.-A. Albouy, Adv. Mater. 2004, 16, 1922-1925.

[53] A. Buguin, M.-H. Li, P. Silberzan, B. Ladoux, P. Keller, J. Am. Chem. Soc. 2006, 128, 1088-1089.

[54] S. Zanotto 2020. PPML - Periodically Patterned Multi-Layer, https://www.mathworks.com/matlabcentral/fileexchange/55401-ppml, MATLAB Central File Exchange (accessed: December 2019).

[55] S. Zanotto, G. Mazzamuto, F. Riboli, G. Biasiol, G. C. La Rocca, A. Tredicucci, A. Pitanti, Nanophotonics 2019, 8(12), 2291-2301.

[56] Zanotto, F. Sgrignuoli, S. Nocentini, D. Martella, C. Parmeggiani, D. S. Wiersma, Appl. Phys. Lett. 2019, 114, 201103.

Appendix A

A Optics of Liquid Crystalline Elastomers

A.1 Optics of uniaxial anisotropic media

The index of refraction of optically anisotropic media, like many crystals and liquid crystals, depends on the propagation direction and on the polarization of incident light. In general, low-symmetry media are characterized by three principal values for the optical index, along the three orthogonal directions of space: n_x, n_y, n_z. These media are defined as biaxial ones. In higher-symmetry uniaxial media, two of the three directions are equivalent, therefore, they are characterized from only two principal indices. The non-degenerate direction is called the optic axis of the material. The index along the direction of the optic axis is denoted with $n_{//}$, while the index in any perpendicular direction with $n_\perp$. The difference between the two indices $\Delta n = n_{//} - n_\perp$ is called birefringence.

At the macroscopic level, a consequence of optical anisotropy is the phenomenon of double refraction. A light ray entering a uniaxial material at an angle ψ with its optic axis, splits itself into two rays polarized at 90° from each other, therefore producing two different images (Figure A.1). One ray is said to be ordinary: it follows the Snell law of refraction and it sees one constant optical index, n_o, regardless of the direction, as if the material was isotropic. The second ray is named extraordinary, as it experiences a variable optical index depending on the direction, $n_e(\psi)$. n_o and $n_e(\psi)$ are connected to $n_{//}$ and $n_\perp$ by the equations:

$$n_o = n_\perp,$$

$$n_e(\psi) = \frac{n_{//} n_\perp}{\sqrt{n_{//}^{\,2} \cos(2\psi) + n_\perp^{\,2} \sin(2\psi)}}.$$

If $\psi = \pi/2$, then $n_e = n_{//}$ and $n_o = n_\perp$ and the two types of indices are often used interchangeably. In contrast when $\psi = 0$, $n_e = n_\perp$. In this case, the uniaxial material appears isotropic due to it is viewed from the direction of its optic axis.

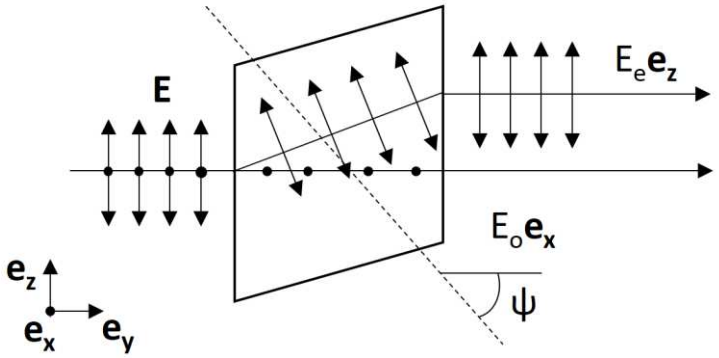

Figure A.1. Double refraction occurring in a slab of uniaxial birefringent material: an unpolarized incoming **E** splits into an ordinary field polarized along $\mathbf{e}_x$ and an extraordinary field polarized along $\mathbf{e}_z$. The dashed line denotes the optic axis.

A.2 Interference of polarized light

One feature of optically anisotropic samples is their ability to display interference colors when observed under crossed polarizers. When an initially linearly polarized light travels through an anisotropic material, extraordinary and ordinary waves propagate at different speeds. Therefore, they acquire an optical phase difference. Since they are coherent, they can interfere. However, being polarized at 90° one with respect to the other one, they are not vibrating in the same plane, and hence cannot interact. Adding an analyzer after the sample, the interference of polarized light is revealed: thanks to the analyzer, the electric fields of the two waves are projected in a common direction, and some component of each wave can interfere with some component of the other (Figure A.2).

It can be demonstrated the intensity of transmitted light after the sample is: [1]

$$I(\phi,\psi)=I_o \sin^2(2\phi) \sin^2[(\pi d/\lambda_o)(n_e(\psi)-n_o)].$$

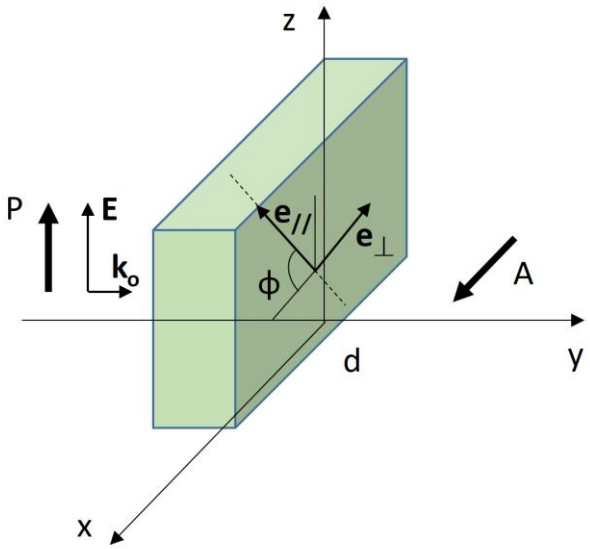

Figure A.2. Uniaxial sample between crossed polarizers. The optic axis of the sample is represented by a dashed line. ψ has been taken as zero: the light propagates perpendicularly to the optic axis. ϕ is the angle between the optic axis and the analyzer.

This equation is the product of two terms: the first one depends on ϕ and it describes the transmittance intensity changes, between crossed polarizers, when the optic axis is rotated. No light goes out the sample if the optic axis is oriented along the polarizer or the analyzer, meanwhile, all of the light goes out the sample if it is placed at 45° in between them. The second term depends on ψ: when viewed from the direction of its optic axis, a uniaxial sample appears black. It also depends on λ_o, therefore colors of interference under white light appear on the sample. In case of light propagating perpendicularly to the optic axis (ψ= 0), the transmitted intensity can be rewritten highlighting the retardation or path difference Γ= dΔn:

$$I(\phi)=I_o \sin^2(2\phi) \sin^2[(\pi\Gamma/\lambda_o)].$$

It is evident that for a given retardation Γ, each wavelength λ_o is transmitted differently. If the sample thickness d and its birefringence Δn are known, the retardation Γ can be calculated with a consequent calculation of the transmission for each wavelength of visible light. All these information can be summarized in the Michel-Lévy chart (Figure A.3) [1] reporting the sample thicknesses as a function of retardations which are matched with a color in the background. Regions of constant birefringence are plotted as lines of slope $1/\Delta n$, since $d = (1/\Delta n)\Gamma$.

Knowing two of the three parameters, the last one can be deduced easily by the chart.

It is possible to observe that one a certain threshold is passed (called the first-order magenta and corresponding to $\lambda_o = 550$ nm), the colors start repeating themselves. A sequence of colors between two magentas define an order.

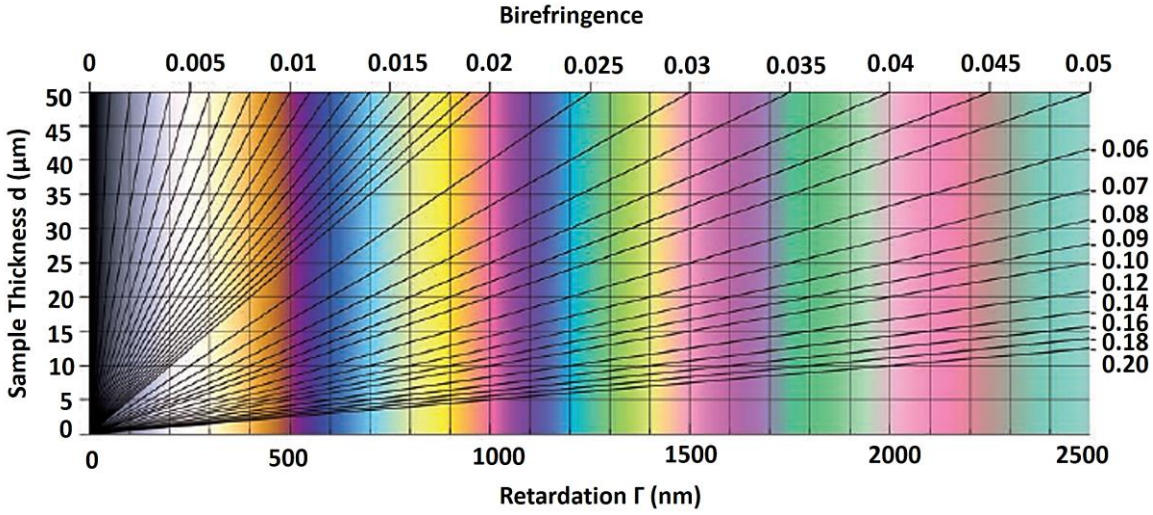

Figure A.3. Michel-Lévy chart. Adapted from reference [1].

Reference

[1] B. E. Sørensen, Eur. J. Miner. 2013, 25, 1, 5-10.

Conclusions

The combination of lithographic techniques, such as UV polymerization and Direct Laser Writing, with soft responsive polymers has been explored in this research work to make photonic structures, for different applications, from tunable telecom filters to tunable structural colors. This study highlights as tailoring the physico chemical properties of custom materials and characterizing their peculiar features enabled to fabricate tunable photonic structure whose good optical properties can be controlled and modulated by multiple tuning activation stimuli (e.g. temperature and light).

A detailed summary of the main results obtained in this research work is reported.

One of the great advantage of custom polymeric materials is the possibility to adjust the chemical formulation and therefore the mesogenic concentration in Liquid Crystalline Networks. In Chapter 3, it has been demonstrated that in such a way the optical properties of photonic materials can be controlled in a deterministic way. This chemical design opens not only to a static determination of the refractive index but also to the modulation of the refractive indices and the optical anisotropy of liquid crystalline mixtures that can be tuned at different temperatures or alternatively by laser light irradiation. The more effective control on the refractive index variation as a function of the applied external stimulus has been obtained by varying the dye concentration as its molecular interaction with the LCN molecules highly affects the overall network arrangement. On the other side, employing a two-photon polymerization process, the increase of the refractive indices has been demonstrated, confirming the need of an in-situ refractive index characterization of micro-structures. For micro-structures, the refractive index variation as a function of the actuating laser power revealed as local light irradiation better activates the reversible molecular disordering and a more pronounced optical anisotropy variation can be attained. Thus for photonic applications, light results as the most effective external trigger source because of the remote and local nature of the stimulus and the induced larger variation of the refractive indices. Measuring the refractive index depending on the molecular formulation and the fabrication technique offered an insight on the polymerization process and molecular interaction that thus affects the matrix optical properties.

On the other side, for custom soft resists, the lithographic parameters should be carefully explored to achieve resolution and structure rigidity comparable to commercial formulation. To this aim, in Chapter 4, we pointed out how refined resolutions, never yet reached for Liquid Crystalline Networks, can be achieved by controlling the polymerization temperature. A home-made system constituted by a Peltier cell (current driven), a heatsink and a thermometer have been engineered and introduced to control the local polymerization temperature down to 5 °C. Using opportune writing parameters at 10 °C, the resulting 3D polymerizable unit results comparable with the typical voxel of commercial resists, enlarging the application field of photo-responsive elastic materials without degradation of the patterned structure rigidity. This research is dictated by the need of spheroidal voxels that represent the best polymerization unit to fabricate three dimensional structures, especially in 3D photonic structures as woodpile photonic crystals or chiral photonic crystals. Exploiting temperature as control parameter to address the lithographic performances opened to a deeper investigation of the molecular anisotropy that rules such behavior. A careful voxel shape analysis highlighted as both temperature, swelling and molecular anisotropy can be exploited to tailor the polymerizable unit dimension. At the same time, it demonstrated a way to study and control anisotropy in Liquid Crystalline Networks in nanostructure polymerization.

In the last part of this manuscript, periodic structures have been studied following different strategies for different applications, from tunable telecom filters to tunable structural colors.

In Chapter 5, DLW lithographic technique enabled for the first time the fabrication of 3D woodpile photonic crystals in LCN matrices. In particular, a tunable filter at telecom wavelength has been designed, fabricated and characterized, using temperature as an external stimulus to tune its optical properties in a reversible way. Moreover, improvement of the optical properties of the elastomeric photonic crystal has been demonstrated by using fabrication at controlled temperature (10 °C) via DLW. In particular, the transmittance attenuation at the stop band for the woodpile written at room temperature is 63%, while at 10 °C it decreases, up to 83%, being now comparable with the transmittance attenuation obtained in case of an Ip-Dip™ woodpile PC (90%). This preliminary but effective result encourage to further explore the use of optimized responsive materials to introduce novel effects and improved

performances. Moreover, the limitation of polymeric materials for photonic applications depends on the reduced refractive index contrast (typical refractive index values for polymers are around 1.5) with respect to air. To achieve a complete photonic band-gap by increasing the refractive index of polymeric microstructures, inorganic moieties or nanoparticles could be incorporated in appropriate design of hybrid materials. This approach can be applied to different polymeric photonic structures, prefabricated also by other techniques, such as standard 3D printers in order to address toward large-scale production through faster and cheaper printing processes and approaching to more challenging structures.

Finally, in Chapter 6 a hybrid system composed by the butterfly wing and a Liquid Crystalline Elastomer artificial muscle has been demonstrated as a smart temperature responsive platform with different functionalities. This first proof of a smart visualizable sensor was developed during a six-month period in collaboration with Prof. Li and Prof. Keller group in Paris, at Chimie ParisTech.

Structural color tuning in *Morpho* butterfly wing was obtained by the integration of a thermo-responsive Liquid Crystalline Elastomer actuator following two different coupling strategies: one using a LCE millimetric film actuator stuck to the back side of the wing, the other one by means of an underlying infiltrated LCE layer. The first strategy leads to a 15 nm blue shift that is thermo-mechanically induced by the iridescence change of the flapping wing. Such color tuning can be also combined with the super hydrophobic properties of the nanostructured wing scales on which a glycerol droplet rolls out by temperature variation, creating a natural/synthetic platform for self-cleaning applications. Following the second strategy, an initial blue shift of the reflectance with respect to the untreated butterfly, induced by a stress of the polymerized layer in the back side of the wing, has been firstly measured at room temperature. During thermal actuation of the LCE muscle up to 80 °C, the wing stripe returns to flat shape (by thermal relaxation of the stress) and then remains flat upon further heating to 160 °C. Together with this thermally driven deformation, the scales dimension shrinks down to 75% of their natural value in their lateral size. Consequently, this effect leads to a blue shift that is not any more ruled by iridescence but only due to a nanostructure modification of the wing ridges. By a comparison of the measured spectra with the Rigorous Coupled Wave Analysis calculation results, we can conclude that the blue shift of the reflection peak can be attributed to the variation of the interspacing in between the lamellae of the scale ridges induced by

the temperature driven LCE strain. The thermo-sensitive properties of this biotic-abiotic platform will open to the first prototype of bio-synthetic responsive devices as visualizable thermal sensors. At the same time, the integration and actuation mechanism can be extended to other thin flexible reflectors and can drive further new structural color designs for responsive tunable platforms. Furthermore, by synthetic material optimization, responsiveness of the composite platforms can be shifted quite easily to different temperature ranges and/or different stimuli, such as light, that can be used to induce actuation towards smart self-tuning devices.

List of publications

- **Two-Photon Laser Writing of Soft Responsive Polymers via Temperature-Controlled Polymerization**
  Isabella De Bellis, Sara Nocentini, Giulia Delli Santi, Daniele Martella, Camilla Parmeggiani, Simone Zanotto, and Diederik S. Wiersma
  Laser Phot. Rev. 2021, submitted.

- **Color Modulation in *Morpho* Butterfly Wings Using Liquid Crystalline Elastomers**
  Isabella De Bellis, Bin Ni, Daniele Martella, Camilla Parmeggiani, Patrick Keller, Diederik S. Wiersma, Min-Hui Li, and Sara Nocentini
  Adv. Intell. Syst. 2020, 2000035

- **Modulation of Optical Properties in Liquid Crystalline Networks across Different Length Scales**
  Isabella De Bellis, Daniele Martella, Camilla Parmeggiani, Eugenio Pugliese, Massimiliano Locatelli, Riccardo Meucci, Diederik S. Wiersma, and Sara Nocentini
  J. Phys. Chem. C 2019, 123, 43, 26522–26527